

This is an Open Access document downloaded from ORCA, Cardiff University's institutional repository:<https://orca.cardiff.ac.uk/id/eprint/141550/>

This is the author's version of a work that was submitted to / accepted for publication.

Citation for final published version:

Bradshaw, Catherine D., Langebroek, Petra M., Lear, Caroline H. , Lunt, Daniel J., Coxall, Helen K., Sisdian, Sindia M. and de Boer, Agatha M. 2021. Hydrological impact of Middle Miocene Antarctic ice-free areas coupled to deep ocean temperatures. *Nature Geoscience* 14 , pp. 429-436. 10.1038/s41561-021-00745-w

Publishers page: <http://doi.org/10.1038/s41561-021-00745-w>

Please note:

Changes made as a result of publishing processes such as copy-editing, formatting and page numbers may not be reflected in this version. For the definitive version of this publication, please refer to the published source. You are advised to consult the publisher's version if you wish to cite this paper.

This version is being made available in accordance with publisher policies. See <http://orca.cf.ac.uk/policies.html> for usage policies. Copyright and moral rights for publications made available in ORCA are retained by the copyright holders.



1 **Hydrological impact of Middle Miocene Antarctic ice-free areas coupled to deep ocean**
2 **temperatures**

3 Catherine D. Bradshaw^{1,2,3,4}, Petra M. Langebroek⁵, Caroline H. Lear⁶, Daniel J. Lunt³, Helen K.
4 Coxall⁴, Sindia M. Sosdian⁶, Agatha M. de Boer⁴

5 ¹Met Office Hadley Centre, Fitzroy Road, Exeter EX1 3PB, UK

6 ²The Global Systems Institute, University of Exeter, North Park Road, Exeter, EX4 4QE

7 ³BRIDGE, School of Geographical Sciences, University of Bristol, Bristol BS8 1SS, UK

8 ⁴Department of Geological Sciences, Stockholm University, SE-106 91, Stockholm, Sweden;

9 ⁵NORCE Norwegian Research Centre, Bjerknes Centre for Climate Research, 5007 Bergen,
10 Norway;

11 ⁶School of Earth and Ocean Sciences, Cardiff University, Main Building, Park Place, Cardiff,
12 CF10 3AT, UK

13 catherine.bradshaw@metoffice.gov.uk

14

15 **Oxygen isotopes from ocean sediments ($\delta^{18}\text{O}$) used to reconstruct past continental ice**
16 **volumes additionally records deep water temperatures (DWT). Traditionally, these are**
17 **assumed to be coupled (ice volume changes cause DWT changes). However, $\delta^{18}\text{O}$ records**
18 **during peak mid-Miocene warmth (~16-15 Ma) document large rapid fluctuations (~1-1.5**
19 **‰) difficult to explain as huge Antarctic ice sheet (AIS) volume changes. Here, using**
20 **climate modelling and data comparisons, we show DWTs are coupled to AIS spatial extent,**
21 **not volume, because Antarctic albedo changes modify the hydrological cycle, affecting**
22 **Antarctic deep-water production regions. We suggest the mid-Miocene AIS had retreated**
23 **significantly from previous Oligocene maxima. The residual ice sheet varied spatially more**

24 rapidly on orbital timescales than previously thought, enabling large DWT swings (up to
25 4°C). When mid-Miocene warmth terminated (~13 Ma) and a continent-scale AIS had
26 stabilized, further ice volume changes were predominantly in height rather than extent,
27 with little impact on DWT. Our findings imply a shift in ocean sensitivity to ice sheet
28 changes occurs when AIS retreat exposes previously ice-covered land; associated feedbacks
29 could reduce the Earth system's ability to maintain a large AIS. This demonstrates ice sheet
30 changes should be characterized not only by ice volume, but also spatial extent.

31 Knowledge of Earth's glacial history and evolution through past warm periods is crucial for
32 understanding cryosphere dynamics and future ice sheet stability. However, the magnitude and
33 timing of ice sheet variations remains uncertain, even for the largest Cenozoic shifts¹. Glacial
34 history is commonly reconstructed from the oxygen isotope composition of fossil calcareous
35 benthic foraminifera shells ($\delta^{18}\text{O}_c$), a proxy for seawater temperature and ice volume². A rapid
36 coeval increase in global $\delta^{18}\text{O}_c$ records is indicative of major ice growth events. Over the last 40
37 million years, rapid expansion of the Antarctic ice sheet (AIS) during the middle Miocene
38 Climatic Transition (MMCT; ~14-13.8 Ma)³ stands out as one of the three periods of major ice
39 growth in the $\delta^{18}\text{O}_c$ record¹.

40 The MMCT is particularly fascinating because of the hypothesized transition from a less stable
41 small wet-based AIS⁴ where meltwater encourages basal sliding and fast moving ice, to a more
42 stable large dry-based AIS where the base is frozen to the bedrock⁵. The major ice growth event
43 is well marked in palaeorecords by a ~1‰ increase in $\delta^{18}\text{O}_c$ (Fig. 1), and thereafter $\delta^{18}\text{O}_c$ values
44 have remained at, or above, these levels to the present day¹ because a climatic threshold was
45 crossed⁶. From $\delta^{18}\text{O}_c$, inferred MMCT ice growth is equivalent to the size of the entire present
46 day AIS, or larger⁷⁻¹¹, but ice sheet isotopic composition changes accounts for some of the

47 amplitude^{12,13}. Sequence stratigraphic estimates of sea level (independent from $\delta^{18}\text{O}_c$) indicate
48 ~20-60 m changes¹⁴⁻¹⁷. Previous studies conclude this magnitude of ice growth implies the pre-
49 MMCT AIS volumes must have been very small^{18,19}. There is little evidence for notable
50 contemporary Northern Hemisphere glaciation²⁰ and although Antarctic topography has changed
51 with time because of tectonics, isostatic adjustments and glacial erosion, topographic changes
52 likely account for ~8 m sea level equivalent (S.L.E.) greater magnitude of ice growth for the
53 same forcing¹³, leaving an additional 12-52 m necessary to explain observations.

54 In stark contrast to the MMCT glaciation, the preceding Miocene Climatic Optimum (MCO;
55 ~16.8-14.8 Ma) contains the lowest $\delta^{18}\text{O}_c$ values of the last 25 million years and fossil evidence
56 for significant tundra and woody Antarctic vegetation^{21,22}; thereby the globally warmest
57 period/least amount of continental ice. Evidence points to a much reduced size of the dynamic
58 wet-based AIS in the MCO, compared with its early Oligocene counterpart¹⁴⁻¹⁷ and large
59 amplitude $\delta^{18}\text{O}_c$ fluctuations combined with sea level estimates imply a highly dynamic
60 cryosphere (Fig. 1, Extended Data Fig. 1).

61 **Differing ice growth-deep water temperature relationships**

62 Some key observations from the mid Miocene Antarctic cryosphere still require explanation.
63 There is a long-held assumption that continental ice volume is inherently coupled to deep water
64 temperatures (DWT) because expanding ice sheets are assumed to cool high latitude regions of
65 deep convection^{1,3,23}. We would therefore expect both the MCO and MMCT to be associated
66 with DWT changes, yet the $\delta^{18}\text{O}_c$ record, combined with independent temperature reconstructions
67 (Fig. 1), reveals some challenging observations. During the MCO, both $\delta^{18}\text{O}_c$ and DWT were
68 highly variable (70% of $\delta^{18}\text{O}_c$ variability attributed to changes in DWT²⁴). During the MMCT,

69 $\delta^{18}\text{O}_c$ was highly variable but DWT variations reduced in amplitude. During the MMCT
70 glaciation, $\delta^{18}\text{O}_c$ was highly variable but DWT variations were small (70% of the $\delta^{18}\text{O}_c$
71 variability attributed to changes in ice volume^{24,25}). After the MMCT, $\delta^{18}\text{O}_c$ and DWT were
72 variable, but less variable than during the MCO.

73 Interpreting $\delta^{18}\text{O}_c$ is complicated because both temperature and the ambient seawater isotopic
74 composition ($\delta^{18}\text{O}_{sw}$) are recorded. $\delta^{18}\text{O}_{sw}$ itself is dependent on global continental ice volume,
75 the isotopic composition of this ice, and localized salinity effects²⁶. Paired independent
76 reconstructions can isolate the temperature signal and analysis of spatially distributed $\delta^{18}\text{O}_c$
77 records can reduce the salinity component. However, for the MMCT glaciation there remains the
78 observation of a large ice increase but little DWT cooling, raising the question: if there is a strong
79 coupling between ice volume and DWT as assumed^{1,3,23}, why did DWT vary so much less during
80 the MMCT when ice sheet growth was most rapid? Here we present new climate model results
81 assessing the impact of ice sheet size on DWT across the MCO and MMCT. Our results confirm
82 the findings of a previous modelling study that DWT is insensitive to ice sheet growth at the
83 MMCT²⁷. While the previous study explains the MMCT ice volume-DWT decoupling in terms of
84 strong feedbacks in the coupled atmosphere-ocean-sea ice system²⁷, our study provides further
85 mechanistic understanding of the differing degrees of middle Miocene ice volume-DWT coupling
86 by proposing a key role for the hydrological cycle. We here advance our understanding of the
87 paradigm by highlighting the important role, not only of ice sheet volume, but also of spatial ice
88 sheet coverage in determining the DWT response to glaciation, during the MMCT and the MCO.

89 We use a fully coupled atmosphere-ocean-vegetation general circulation model, HadCM3LB-
90 M2.1a²⁸ configured with middle Miocene palaeogeography (see Methods and Fig. 2). For our
91 initial assessment using preindustrial CO_2 concentrations, we find that AIS expansion from

92 ICE_{FREE} to ICE_{PART22m} and from ICE_{PART22m} to ICE_{FULL55m} reduces DWT by $\sim 0.5^{\circ}\text{C}$ for each
93 step, thus here ice growth and DWT are coupled (Fig. 3a). However, AIS expansion from
94 ICE_{FULL55m} to ICE_{FULL90m} does not cause further deep ocean cooling (in contrast a slight
95 temperature increase is seen), thus here ice growth and DWT are decoupled (ice volume changes
96 do not affect DWT).

97 We propose that coupling between ice sheet volume and DWT only occurs until the ice sheet
98 reaches the coast because the ice-albedo feedback mechanism and vegetation-climate interactions
99 invoke additional feedback processes identified here for the first time. To demonstrate it is ice
100 sheet spatial extent (rather than height/volume) that is coupled to DWT, we carry out a non-
101 realistic sensitivity study imposing AIS configurations spanning extreme endmembers from ice-
102 free to ice-covered but keep ice volume constant. We assume the ice sheet is of “skin-thickness”
103 (no effective change in elevation as compared to the ice-free state, nominally 1 m S.L.E when
104 fully ice-covered; “ICE_{FULL1m}”), and vary the ice extent longitudinally, latitudinally and
105 topographically. We use preindustrial CO₂ concentrations throughout and conduct an additional
106 high CO₂ sensitivity test (~ 850 ppm; Fig. 4). Combining our results, we find a strong relationship
107 between ice-free extent and DWT, with no evidence of non-linearity (Fig. 3b).

108 **The mechanism linking ice cover to deep water temperatures**

109 Our modelling results suggest summertime “ice-free” Antarctica (ICE_{FREE}, Fig 3, column 1)
110 would be warm and wet, because the land-sea thermal contrast drives monsoon winds, which
111 transport moisture into the Antarctic continental interior from the Southern Ocean (Fig. 5a-c).
112 This moisture falls over the relatively warm continent as rain, not snow, during the summer
113 months (Fig. 5b), and over much of the continent during the winter months for the two highest

114 CO₂ scenarios. Summertime Antarctic temperatures and precipitation are similar to proxy
115 reconstructions for a vegetated Antarctica^{4,21,22,29-31}. A comprehensive model-data comparison
116 (Supplementary Note) indicates peak CO₂ would need to be > 850 ppm for a complete overlap
117 with proxy reconstructions, in agreement with recent MCO reconstructions³². ICE_{FREE} also results
118 in the warmest freshest deep ocean of all the simulations (Fig. 5d-e). Surface runoff from the
119 active hydrologic cycle, being less saline and thus less dense than the seawater it drains into,
120 forms a polar halocline at the surface. This halocline reduces ventilation of the deep ocean (Fig.
121 5d), weakening overturning. In our simulations, deep water is in all cases primarily produced in
122 the Southern Ocean, thus DWTs are determined by southern sinking regions. Antarctic Bottom
123 Water (AABW) production never ceases completely in the model for any scenario
124 (Supplementary Discussion B).

125 In ICE_{FULL1m}, ICE_{FULL55m} and ICE_{FULL90m} (Fig 3, columns 3-5), cold surface temperatures
126 near the ice sheet and the large increase in albedo causes localized radiative cooling of the air
127 column and a reduction in vapour holding capacity. The land-sea thermal contrast reduces (Fig.
128 5a) and the summer monsoon system ceases to operate. Katabatic winds form as the cold dense
129 air flows away from the elevated areas towards the coast (Fig. 5c). The interaction between the
130 winds and sea-ice is complex and dependent upon background CO₂ (Fig. 5b; Supplementary
131 Discussion A). Reduced precipitation (Fig. 5b) and subsequent runoff reduces ocean stratification
132 (Fig. 5d), permitting the cold surface waters to sink more freely from the continental shelf into
133 the abyss (Fig. 5e). Increased AABW production invigorates ocean ventilation.

134 Empirical studies show a clear relationship between ice sheet volume and spatial extent³³,
135 implying ice sheet thickness is limited by spatial extent. Therefore, in order to grow vertically, an
136 ice sheet must also grow spatially (Supplementary Discussion C). After the ice sheet reaches the

137 ocean, additional growth is necessarily predominantly vertical. Although a thickening ice sheet is
138 accompanied by further cooling and drying of the air, this does not significantly affect runoff
139 because precipitation has already been reduced to a low level and is falling as snow, not rain.
140 Consequently, the surface ocean salinity does not change much and hence neither does deep
141 water production, ocean ventilation or, crucially, DWT. This explains the ice volume-DWT
142 decoupling between ICE_{FULL1m} , $ICE_{FULL55m}$ and $ICE_{FULL90m}$. The global mean DWTs begin to
143 rise slowly as ice volume (height) increases (in the absence of CO_2 changes) because the higher
144 topography reduces the amount of summertime low clouds around the Antarctic coastline by 10-
145 15% (not shown), allowing more solar radiation to reach the surface and reducing sea ice, which
146 locally causes greater absorption of solar radiation into the ocean.

147 Our model has a fairly linear response to both a gradually increasing and decreasing ice sheet
148 extent. However, we note in a dynamic ice sheet model, ice-melt in the decreasing ice sheet
149 scenario would result in additional surface runoff that would likely impact AABW production, at
150 least temporarily, as demonstrated in a studies of the modern AIS³⁴.

151 **Sensitivity to atmospheric CO_2 and orbit**

152 Our model does not have an interactive AIS, so the response of the ice sheet to CO_2 forcing is not
153 included and our study is limited to a single model with mid-range CO_2 sensitivity³⁵. However,
154 our results show that atmospheric CO_2 has a much smaller impact on the hydrological regime
155 than ice sheet configuration (Supplementary Discussion A). CO_2 impacts sea-ice extent and sea
156 surface temperatures which in turn affect the deeper layers via vertical mixing, in a process that is
157 complex and non-linear (Supplementary Discussion A).

158 For the MCO, the most recent CO₂ record suggests an average range of concentrations between
159 630 and 470 ppm³². Using the relationship between CO₂ and DWT calculated from our
160 simulations, we infer a consequent ~0.8 °C mean temperature change in the 2-3 km deep layer in
161 the Southern Hemisphere (Fig. 6), which is about 80% of the ~1.0 °C impact from increasing ice-
162 extent (Fig. 3, ICE_{FULL}1m - ICE_{FREE}) in the same layer. This provides a picture of the average
163 DWT changes. The site-specific temperature changes (of 2-4 °C, Fig. 1), will depend also on
164 local dynamics. At Site 761, our simulations estimate a contribution of 0.5 °C from CO₂
165 variations compared to a 0.9-1.9 °C contribution from ice extent changes, and at Site 1171, the
166 contribution from CO₂ is between 0.5-0.6 °C compared to 1.0-1.5 °C from ice extent
167 (Supplementary Discussion D and E). Our results show that CO₂ changes alone cannot explain
168 the observed DWT range at the MCO and moreover, for both the mean layer and the specific
169 sites, our model suggests that ice-extent had a larger impact on DWT than CO₂. For the MMCT
170 glaciation, the most recent CO₂ reconstructions show at most a 170 ppm reduction from ~570 to
171 400 ppm³², for which we infer from our ice-covered model simulations a temperature drop of
172 0.5–0.8 °C at the two sites (Supplementary Discussion E). This is consistent with the
173 reconstructions (Fig. 1) if we assume Antarctica was ice-covered prior to the MMCT glaciation
174 (i.e. little DWT change occurred as a result of increasing ice sheet extent). In the absence of ice
175 sheet changes, we find a minimal effect of orbital configuration on DWT (Supplementary
176 Discussion F).

177 **From thin and vulnerable to thick and established**

178 We introduce the hydrological cycle as a crucial mechanism mediating the link between the
179 DWT and the ice spatial extent (rather than absolute volume), thus explaining the different
180 degrees of coupling between ice sheet changes and DWT during the MMCT and MCO.

181 Our new results lead us to propose that DWT varied by up to 4°C during the MCO because the
182 spatial extent of ice and vegetation rapidly altered. Taken together with existing $\delta^{18}\text{O}_c$,
183 temperature, vegetation and CO_2 reconstructions, this implies the AIS had retreated significantly
184 during the MCO, when average CO_2 concentrations were likely 470-630 ppm, reaching 780-1100
185 ppm at times³². Previous work clearly demonstrates the dynamic behaviour of a small AIS when
186 driven by CO_2 changes combined with orbital forcing⁷. How far exactly the ice sheet retreated
187 during these warmest intervals, however, is unknown. Ice sheet modelling suggests a retreat
188 exposing 60-70% of the Antarctic land surface is consistent with the paleorecord¹³. Other work
189 concludes a retreat even greater than this^{36,37}, perhaps even ice-free¹¹. The evidence for
190 vegetation, including trees, growing on the continent throughout the MCO^{22,29} implies both warm
191 and wet conditions, and it is suggested the moisture supply derived from the Southern Ocean²⁹.
192 To achieve this, our results indicate a greater reduction of ice is needed than the ICE_{PART22m}
193 scenario ice sheet extent, because the Wilkes Land winds are directed landward in ICE_{FREE}, but
194 seaward for ICE_{PART22m} (Figure 3c). We suggest these monsoon moisture-carrying winds
195 induced by spatial ice retreat could provide an explanation for major ice advance onto the
196 continental shelf in the Ross Sea^{38,39} during the MCO occurring at the same time as open water
197 and woody vegetation in the Wilkes Land²² (Supplementary Discussion G).

198 We further infer DWT varied so much less during the MMCT when the AIS volume was growing
199 rapidly because it had already extended to cover most of the continent prior to the major ice
200 growth event, in agreement with previous findings²⁷. Thus, the ice sheet subsequently increased
201 mainly in thickness, not area, and so DWTs were largely unaffected because, without the
202 additional ice-albedo feedback, changes to the hydrological cycle were much smaller. Post-
203 MMCT (label 1 in Fig. 1), both $\delta^{18}\text{O}_c$ and DWT are variable, but less so than during the MCO.

204 The exact degree of coupling, and its mechanism, needs to be explored in a model set-up that
205 includes marine-based ice sheets and ice shelves, not included in this study. However, the
206 physical limits on seawater temperatures (-1.8°C) will set the lower boundary on possible
207 temperature changes as climate cools.

208 Interpretation of our results leads us to support a highly dynamic MCO AIS, and state, alongside
209 CO_2 , it was changes in ice sheet area and proximity to the coast, not volume, that were of key
210 importance for global DWTs. This fundamentally changes the way we should characterize ice
211 sheet changes and how we must view the long-term $\delta^{18}\text{O}_c$ records spanning greenhouse-icehouse
212 transitions. In the absence of independent temperature proxies, it must not be assumed that DWTs
213 scale with ice volume changes.

214 Whilst we do not propose the MCO Antarctica was ever completely ice-free, our results
215 demonstrate any spatial retreat of the AIS can increase precipitation causing associated warming
216 of the deep ocean - changes perhaps having the ability to both accelerate ice melt of ice shelves
217 and glaciers through hydrofracturing from increased precipitation falling into cravasses^{40,41} and to
218 accelerate ice melt of marine-based subglacial basins^{34,41}. Although the temperature changes
219 resulting from changing ice sheet extent are similar to those resulting from CO_2 changes, our
220 study does not include feedbacks to the carbon cycle or to the ice sheet itself and therefore the
221 significance of our results could be greater than indicated here. Our non-realistic sensitivity
222 studies using only a skin-thickness of ice demonstrate the importance of both surface albedo and
223 roughness for a hydrologic control on DWT evolution. It is therefore possible that our
224 mechanism could operate in areas even without complete ice-loss if these two factors change
225 significantly. For example: in regions of debris-covered glaciers, rock glaciers, vegetation-
226 covered rock glaciers and “glacier mice”, which all increase in the context of retreating ice

227 glaciers^{42–45}, in regions of accumulating dark particles (dust and soot)⁴⁶ and in regions of glacier
228 algae, which bloom in supraglacial meltwater⁴⁷.

229 **References**

- 230 1. Zachos, J., Pagani, M., Sloan, L., Thomas, E. & Billups, K. Trends, rhythms, and
231 aberrations in global climate 65 Ma to present. *Science*. **292**, 686–693 (2001).
- 232 2. Chappell, J. & Shackleton, N. Oxygen isotopes and sea level. *Nature* **324**, 137 (1986).
- 233 3. Shackleton, N. J. & Kennett, J. P. Paleotemperature history of the Cenozoic and the
234 initiation of Antarctic glaciation: oxygen and carbon isotope analyses in DSDP Sites
235 277, 279, and 281. *Initial Reports of Deep Sea Drilling Project* **29**, (U.S. Government
236 Printing Office, 1975).
- 237 4. Lewis, A. R. *et al.* Mid-Miocene cooling and the extinction of tundra in continental
238 Antarctica. *Proc. Natl. Acad. Sci.* **105**, 10676–10680 (2008).
- 239 5. Kleman, J. & Glasser, N. F. The subglacial thermal organisation (STO) of ice sheets. *Quat.*
240 *Sci. Rev.* **26**, 585–597 (2007).
- 241 6. Levy, R. H. *et al.* Antarctic ice-sheet sensitivity to obliquity forcing enhanced through
242 ocean connections. *Nat. Geosci.* **12**, 132–137 (2019).
- 243 7. Langebroek, P. M., Paul, A. & Schulz, M. Antarctic ice-sheet response to atmospheric
244 CO₂ and insolation in the Middle Miocene. *Clim. Past* **5**, 633–646 (2009).
- 245 8. Lear, C. H., Mawbey, E. M. & Rosenthal, Y. Cenozoic benthic foraminiferal Mg/Ca and
246 Li/Ca records: Toward unlocking temperatures and saturation states. *Paleoceanography*

- 247 **25**, (2010).
- 248 9. Lear, C. H. *et al.* Neogene ice volume and ocean temperatures: Insights from infaunal
249 foraminiferal Mg/Ca paleothermometry. *Paleoceanography* **30**, 1437–1454 (2015).
- 250 10. de Boer, B., van de Wal, R. S. W., Lourens, L. J. & Bintanja, R. Transient nature of the
251 Earth’s climate and the implications for the interpretation of benthic $\delta^{18}\text{O}$ records.
252 *Palaeogeogr. Palaeoclimatol. Palaeoecol.* **335**, 4–11 (2012).
- 253 11. Miller, K. G. *et al.* Cenozoic sea-level and cryospheric evolution from deep-sea
254 geochemical and continental margin records. *Sci. Adv.* **6**, eaaz1346 (2020).
- 255 12. Langebroek, P. M., Paul, A. & Schulz, M. Simulating the sea level imprint on marine
256 oxygen isotope records during the middle Miocene using an ice sheet–climate model.
257 *Paleoceanography* **25**, (2010).
- 258 13. Gasson, E., DeConto, R. M., Pollard, D. & Levy, R. H. Dynamic Antarctic ice sheet
259 during the early to mid-Miocene. *Proc. Natl. Acad. Sci.* **113**, 3459–3464 (2016).
- 260 14. Kominz, M. A. *et al.* Late Cretaceous to Miocene sea-level estimates from the New Jersey
261 and Delaware coastal plain coreholes: An error analysis. *Basin Res.* **20**, 211–226 (2008).
- 262 15. Miller, K. G. *et al.* The Phanerozoic record of global sea-level change. *Science.* **310**, 1293–
263 1298 (2005).
- 264 16. Kominz, M. A., Miller, K. G., Browning, J. V, Katz, M. E. & Mountain, G. S. Miocene
265 relative sea level on the New Jersey shallow continental shelf and coastal plain derived
266 from one-dimensional backstripping: A case for both eustasy and epeirogeny. *Geosphere*
267 **12**, 1437–1456 (2016).

- 268 17. John, C. M. *et al.* Timing and magnitude of Miocene eustasy derived from the mixed
269 siliciclastic-carbonate stratigraphic record of the northeastern Australian margin. *Earth*
270 *Planet. Sci. Lett.* **304**, 455–467 (2011).
- 271 18. Pekar, S. F. & DeConto, R. M. High-resolution ice-volume estimates for the early
272 Miocene: Evidence for a dynamic ice sheet in Antarctica. *Palaeogeogr. Palaeoclimatol.*
273 *Palaeoecol.* **231**, 101–109 (2006).
- 274 19. Lear, C. H., Elderfield, H. & Wilson, P. A. Cenozoic deep-sea temperatures and global ice
275 volumes from Mg/Ca in benthic foraminiferal calcite. *Science.* **287**, 269–272 (2000).
- 276 20. Bierman, P. R., Shakun, J. D., Corbett, L. B., Zimmerman, S. R. & Rood, D. H. A
277 persistent and dynamic East Greenland Ice Sheet over the past 7.5 million years. *Nature*
278 **540**, 256–260 (2016).
- 279 21. Warny, S. *et al.* Palynomorphs from a sediment core reveal a sudden remarkably warm
280 Antarctica during the middle Miocene. *Geology* **37**, 955–958 (2009).
- 281 22. Sangiorgi, F. *et al.* Southern Ocean warming and Wilkes Land ice sheet retreat during the
282 mid-Miocene. *Nat. Commun.* **9**, 317 (2018).
- 283 23. De Boer, B., de Wal, R. S. W., Bintanja, R., Lourens, L. J. & Tuenter, E. Cenozoic global
284 ice-volume and temperature simulations with 1-D ice-sheet models forced by benthic $\delta^{18}\text{O}$
285 records. *Ann. Glaciol.* **51**, 23–33 (2010).
- 286 24. Kochhann, K. G. D., Holbourn, A., Kuhnt, W. & Xu, J. Eastern equatorial Pacific benthic
287 foraminiferal distribution and deep water temperature changes during the early to middle
288 Miocene. *Mar. Micropaleontol.* **133**, 28–39 (2017).

- 289 25. Shevenell, A. E., Kennett, J. P. & Lea, D. W. Middle Miocene ice sheet dynamics,
290 deep-sea temperatures, and carbon cycling: A Southern Ocean perspective. *Geochemistry,*
291 *Geophys. Geosystems* **9**, (2008).
- 292 26. Waelbroeck, C. *et al.* Sea-level and deep water temperature changes derived from benthic
293 foraminifera isotopic records. *Quat. Sci. Rev.* **21**, 295–305 (2002).
- 294 27. Knorr, G. & Lohmann, G. Climate warming during Antarctic ice sheet expansion at the
295 Middle Miocene transition. *Nat. Geosci.* **7**, 376 (2014).
- 296 28. Valdes, P. J. *et al.* The BRIDGE HadCM3 family of climate models: HadCM3@ Bristol
297 v1. 0. *Geosci. Model Dev.* **10**, 3715–3743 (2017).
- 298 29. Feakins, S. J., Warny, S. & Lee, J.-E. Hydrologic cycling over Antarctica during the
299 middle Miocene warming. *Nat. Geosci.* **5**, 557 (2012).
- 300 30. Rees-Owen, R. L. *et al.* The last forests on Antarctica: Reconstructing flora and
301 temperature from the Neogene Sirius Group, Transantarctic Mountains. *Org. Geochem.*
302 **118**, 4–14 (2018).
- 303 31. Passchier, S. *et al.* Early Eocene to middle Miocene cooling and aridification of East
304 Antarctica. *Geochemistry, Geophys. Geosystems* **14**, 1399–1410 (2013).
- 305 32. Sosdian, S. M. *et al.* Constraining the evolution of Neogene ocean carbonate chemistry
306 using the boron isotope pH proxy. *Earth Planet. Sci. Lett.* **498**, 362–376 (2018).
- 307 33. Paterson, W. S. B. *The physics of glaciers.* (Elsevier, 2016).
- 308 34. Phipps, S. J., Fogwill, C. J. & Turney, C. S. M. Impacts of marine instability across the

- 309 East Antarctic Ice Sheet on Southern Ocean dynamics. *Cryosphere* **10**, 2317–2328 (2016).
- 310 35. Rugenstein, M. *et al.* Equilibrium climate sensitivity estimated by equilibrating climate
311 models. *Geophys. Res. Lett.* **47**, e2019GL083898 (2020).
- 312 36. Frigola, A., Prange, M. & Schulz, M. Boundary conditions for the Middle Miocene
313 Climate Transition (MMCT v1. 0). *Geosci. Model Dev.* **11**, 1607–1626 (2018).
- 314 37. Hamon, N. *et al.* Growth of subtropical forests in Miocene Europe: The roles of carbon
315 dioxide and Antarctic ice volume. *Geology* **40**, 567–570 (2012).
- 316 38. Levy, R. *et al.* Antarctic ice sheet sensitivity to atmospheric CO₂ variations in the early to
317 mid-Miocene. *Proc. Natl. Acad. Sci.* **113**, 3453–3458 (2016).
- 318 39. Colleoni, F. *et al.* Spatio-temporal variability of processes across Antarctic ice-bed–ocean
319 interfaces. *Nat. Commun.* **9**, 2289 (2018).
- 320 40. Van der Veen, C. J. Fracture mechanics approach to penetration of surface crevasses on
321 glaciers. *Cold Reg. Sci. Technol.* **27**, 31–47 (1998).
- 322 41. DeConto, R. M. & Pollard, D. Contribution of Antarctica to past and future sea-level rise.
323 *Nature* **531**, 591 (2016).
- 324 42. Deline, P. Change in surface debris cover on Mont Blanc massif glaciers after the ‘Little
325 Ice Age’ termination. *The Holocene* **15**, 302–309 (2005).
- 326 43. Fickert, T., Friend, D., Grüniger, F., Molnia, B. & Richter, M. Did debris-covered
327 glaciers serve as Pleistocene refugia for plants? A new hypothesis derived from
328 observations of recent plant growth on glacier surfaces. *Arctic, Antarct. Alp. Res.* **39**, 245–

329 257 (2007).

330 44. Zale, R. *et al.* Growth of plants on the Late Weichselian ice-sheet during Greenland
331 interstadial-1? *Quat. Sci. Rev.* **185**, 222–229 (2018).

332 45. Dickson, J. H. & Johnson, R. E. Mosses and the beginning of plant succession on the
333 Walker Glacier, southeastern Alaska. *Lindbergia* **37**, 60–65 (2014).

334 46. Gölles, T., Bøggild, C. E. & Greve, R. Ice sheet mass loss caused by dust and black carbon
335 accumulation. *Cryosph.* **9**, 1845–1856 (2015).

336 47. Williamson, C. J. *et al.* Algal photophysiology drives darkening and melt of the Greenland
337 Ice Sheet. *Proc. Natl. Acad. Sci.* (2020).

338 48. De Vleeschouwer, D., Vahlenkamp, M., Crucifix, M. & Pälike, H. Alternating Southern
339 and Northern Hemisphere climate response to astronomical forcing during the past 35 m.y.
340 *Geology* **45**, 375–378 (2017).

341 49. Pekar, S. F., Christie-Blick, N., Kominz, M. A. & Miller, K. G. Calibration between
342 eustatic estimates from backstripping and oxygen isotopic records for the Oligocene.
343 *Geology* **30**, 903–906 (2002).

344 50. DeConto, R. M. & Pollard, D. Rapid Cenozoic glaciation of Antarctica induced by
345 declining atmospheric CO₂. *Nature* **421**, 245 (2003).

346 **Acknowledgements**

347 C.D.B., D.J.L. were supported by NERC grant NE I006281/1. C.H.L. and S.M.S were supported
348 by NERC grant NE/I006427/1. A.d.B. and C.D.B. gratefully acknowledge support from the

349 Swedish Research Council project [2016-03912]. This work was carried out using the
350 computational facilities of the Advanced Computing Research Centre, University of Bristol -
351 <http://www.bristol.ac.uk/acrc/>. We thank the reviewers for their constructive comments on our
352 manuscript. We thank Dan Suri, Chief Operational Meteorologist, Met Office and Galia
353 Guentchev, Senior Scientist, Met Office, Sarah Feakins and Tim Naish for feedback on earlier
354 drafts of this manuscript. We also thank Edward Gasson for providing a plot of his ice sheet
355 model results¹³.

356 **Author Contributions**

357 C.D. B., C.H.L. and D.J.L. conceived the project and directed the research with the assistance of
358 A.M.d.B. C.D.B. conducted and interpreted the modelling with the assistance of D.J.L., A.M.d.B.,
359 and P.M.L. C.D.B. compiled and interpreted the proxy records with the assistance of C.H.L.,
360 A.M.d.B., H.K.C. and S.M.S. C.D.B. led writing of the paper. All of the authors contributed to
361 writing the manuscript.

362 **Author Information**

363 The authors declare no competing interests. Correspondence should be addressed to C.D.B.
364 Catherine.bradshaw@metoffice.gov.uk

365
366 **Fig. 1. Mid-Miocene benthic (*Cibicidoides* spp.) oxygen isotope, deep water temperatures**
367 **(DWT) and sea level changes. a** $\delta^{18}\text{O}_c$ splice⁴⁸, **b** Site 1171 DWT²⁵, Southern Ocean
368 (Antarctica-proximal), **c** Site 761 DWT⁸, Indian Ocean (Antarctica-distal but in AABW path).
369 Data locations shown on right of panels. DWTs are Mg/Ca reconstructions (uncertainty $\pm 4^\circ\text{C}$;
370 relative values are considered more robust than absolutes). Other available DWT records are too
371 low resolution/short. Data are plotted on their respective age models (full details: Supplementary

372 Table S11). **d** Sea level^{11,14} (Eustatic estimates¹⁴ x1.48 c.f.⁴⁹). Shading: Miocene Climatic
373 Optimum (MCO, yellow), middle Miocene Climatic Transition (MMCT, blue+grey), major ice
374 growth event (MMCT, blue). Vertical lines are indicative of the typical maximum $\delta^{18}\text{O}_c/\text{DWT}$
375 amplitudes during the MCO (4), MMCT prior to the major ice growth event (3), MMCT major
376 ice growth event (2) and post- MMCT (1). Since the data cover different times and resolutions,
377 these lines are not coincident in time between panels a-c.

378
379 **Fig. 2. Orography and ice sheet configurations.** **a** Orography for the different ice volume
380 scenarios simulated (sea level equivalent, S.L.E.). **b** Ice cover fraction for the different scenarios
381 simulated. The latitudinal, longitudinal, topographical and DeConto and Pollard 2003⁵⁰ ice sheet
382 extents all use the 1m S.L.E. orography from **a**. The percentage of ice cover is shown under each
383 thumbnail. Refer also to Methods for more information.

384
385 **Fig. 3. Annual mean Southern Hemisphere deep water temperatures estimates averaged**
386 **between 2 and 3 km, simulated with different sized Antarctic ice sheets.** **a** Changing ice sheet
387 volume: ice-free (ICE_{FREE}), the 22 m sea level equivalent (S.L.E.) regional scale ice sheet
388 configuration ($\text{ICE}_{\text{PART}22\text{m}}$), the 55 m S.L.E. continental ice sheet configuration ($\text{ICE}_{\text{FULL}55\text{m}}$),
389 and the 90 m S.L.E. continental scale ice sheet configuration ($\text{ICE}_{\text{FULL}90\text{m}}$), **b** Changing ice sheet
390 extent: different scenarios between 0% and 100% ice covered (refer to Fig. 2 for details). CO_2 is
391 280 ppm in all cases unless specified and a modern orbit assumed; refer to Methods for more
392 information.

393

394 **Fig. 4. Middle Miocene atmospheric CO₂ reconstructions.** Data provided in Supplementary
395 Table S5 plotted on respective age models. Shading: Miocene Climatic Optimum (MCO,
396 yellow), middle Miocene Climatic Transition (MMCT, blue+grey), major ice growth event
397 (MMCT, blue). Note: the Boron isotope-based CO₂ reconstructions from Sosdian et al., 2018³²
398 plotted are from the L02 scenario and shows two error ranges: the 66% (thicker blue lines) and
399 95% (thinner blue lines) confidence intervals. This dataset supercedes the data from some other
400 publications as documented in Supplementary Table S5 (the reconstructions from the original
401 publications are not plotted).

402
403 **Fig. 5. Simulated atmospheric and oceanographic conditions with different sized Antarctic**
404 **ice sheets. a,** Summer (DJF) air temperature, **b,** Summer precipitation (land only shown) and sea
405 ice fraction, **c,** Summer windspeed and prevailing directions, **d,** Annual mean Southern
406 Hemisphere meridional mean ocean salinity, **e,** Annual mean Southern Hemisphere meridional
407 mean ocean temperature. Scenario ICE_{FREE} has no ice sheet, ICE_{PART22m} is a regional scale 22m
408 S.L.E. ice sheet, and ICE_{FULL1m}, ICE_{FULL55m} and ICE_{FULL90m} are 1m S.L.E., 55m and 90m
409 S.L.E. continental size ice sheets respectively. Refer to Methods and Fig. 2 for more details of the
410 boundary conditions used. CO₂ is 280 ppm in all cases.

411
412 **Fig. 6. Annual mean Southern Hemisphere simulated with different sized Antarctic ice**
413 **sheets and CO₂ concentration.** Deep water temperatures are averaged between 2 and 3 km
414 water depth. Ice sheet configurations as in Fig. 5. Refer to Methods and Fig. 2 for more details of
415 the boundary conditions used.

416

417 **Methods**

418 The model used in these experiments is fully coupled atmosphere-ocean GCM HadCM3LB-
419 M2.1²⁸ with the interactive vegetation model TRIFFID⁵¹. This is the low resolution ocean version
420 of HadCM3⁵² and both the atmosphere and the ocean components have a resolution of 2.5°
421 latitude by 3.75° longitude. The model is run without the need for flux adjustments in the modern
422 configuration by the now-standard practice of removing Iceland from the land-sea mask⁵³. Eddies
423 in the model are parameterized using a spatially constant coefficient of $1000 \text{ m}^2 \text{ s}^{-1}$ according to
424 the Gent-Williams scheme⁵⁴. Vertical diffusion is parameterized using the Richardson number-
425 dependent formulation and a background diffusivity of $1 \times 10^{-5} \text{ m}^2 \text{ s}^{-1}$ at the surface which increases
426 linearly at a rate of $2.8 \times 10^{-8} \text{ m}^2 \text{ s}^{-1} \text{ m}^{-1}$ with depth⁵⁵. A linear mixing profile with depth has been
427 shown to be able to capture that vertical mixing is strongest over topography⁵⁶. Of all the
428 PMIP1.5 and PMIP2 models, only the HadCM3-based models, which had such a linear scheme,
429 managed to correctly simulate the Last Glacial Maximum inverse relationship between the
430 volume and production rate of AABW⁵⁶. As such, we have confidence key processes determining
431 the transfer of surface climate signals to depth are represented well in the ocean component of
432 our model.

433 The background palaeogeography⁵⁷ is representative of middle Miocene conditions. Notable
434 features as compared to modern are that the Panama Gateway and the Indonesian Seaway are
435 open, Australia is located 4° farther south, and the Barents Sea and the Bering Strait are closed.
436 Note that in all experiments, the Eastern Tethys Seaway is also closed. Land topography also
437 differs from modern in that the Tibetan Plateau and the Andes are more than 2000 m lower than
438 at present, and the Rockies Mountains are about 1000 m higher. Greenland is also more than
439 2000m lower than modern, and is ice free.

440 To investigate middle Miocene climate we used a suite of CO₂ and Antarctic ice cover sensitivity
441 studies. Four Antarctic ice cover configurations were each simulated at 5 CO₂ concentrations:
442 180, 280, 400, 560 and ~850 ppm (in accordance with the uncertainty and temporal variability in
443 CO₂ reconstructions for the middle Miocene; Fig. 4), giving a total of 20 simulations. The 4 ice
444 sheet configurations are defined as follows. Firstly, an ice-free Antarctica using an Antarctic
445 bedrock configuration appropriate for the Late Oligocene⁵⁷, referred to as “ICE_{FREE}”. Ice free
446 Antarctica is initialised in the TRIFFID model as covered in in the plant functional type ‘shrubs’.
447 Although unrealistic for the mid Miocene, as the extreme end member scenario, this scenario
448 helps to place our findings into context. Secondly, a skin-thickness ice-covered Antarctica (< 1m
449 sea level equivalent) where the topography is kept the same as in the ice-free case in 1, referred to
450 as “ICE_{FULL1m}”. Thirdly, a modern-like ice-covered Antarctica (~55 m sea level equivalent)
451 using the palaeogeographic configuration for the middle Miocene⁵⁷, referred to as “ICE_{FULL55m}”.
452 Finally, a larger-than-modern ice-covered Antarctica (~90 m sea level equivalent), referred to as
453 “ICE_{FULL90m}”.

454 Configurations 2-4 have the same areal extent and differ in ice sheet height only. In accordance
455 with the proposed 90m drop in sea level over the MMCT⁹, boundary conditions for an ice sheet
456 of this proportion were developed by assuming one-third of the ice is associated with isostatic
457 depression and then applying a uniform increase in elevation across the continent to obtain a 90
458 m sea level equivalent. Additionally simulated at 280 ppm (using the topography of the
459 ICE_{FULL55m} scenario) is the spatial extent of the regional scale ice sheet simulated by a model
460 that includes ice-shelf hydrofracture and ice cliff collapse of 22 m S.L.E.,¹³, referred to as
461 “ICE_{PART22m}”. See Fig. 2 for more details of the Antarctic boundary conditions. Outside of
462 Antarctica, the paleogeography remains constant at the middle Miocene reconstruction. Apart

463 from the prescribed CO₂ changes, all other greenhouse gases, solar and orbital parameters remain
464 at modern settings.

465 To investigate the sensitivity of the hydrological cycle to the extent of Antarctic ice-free area, an
466 additional series of simulations were carried out with a gradually increasing Antarctic ice sheet
467 area, from no ice to the maximum ice sheet extent for scenario 2 above. These intermediate area
468 ice sheets expand latitudinally, longitudinally or topographically as demonstrated in Fig. 2. No
469 change was made to the elevation from the ice-free condition and therefore all of these
470 simulations represent a skin-thickness of ice cover. Two sets of scenarios were run for each of the
471 longitudinal ice growth boundary conditions: Firstly, beginning from an ice-free initial condition
472 (as described above) and secondly, beginning from a 100% ice-covered initial condition and
473 decreasing towards zero. The rest of the scenarios were initiated from the 100% ice-covered state
474 and therefore lose ice only. The longitudinal ice growth scenario also included 4 configurations
475 simulated at ~850 ppm CO₂ (20%, 40%, 60% and 80% ice-covered, refer to Fig. 2).

476 All simulations assume a modern orbit except for 4 sensitivity test cases. A cold orbital
477 configuration favorable for Antarctic glaciation (low obliquity (22.1°), high eccentricity (0.054),
478 perihelion during boreal summer, 374 W/m² summer insolation at 70°S) and a warm orbital
479 configuration favourable for Antarctic deglaciation (high obliquity (24.5°), high eccentricity
480 (0.054), perihelion during austral summer, 483 W/m² summer insolation at 70°S) were identified.
481 Cold and warm orbit sensitivity tests were carried out for the “ICE_{FREE}” and the “ICE_{FULL55m}”
482 configurations.

483 All of the middle Miocene simulations continue from a 2100 year integration under late Miocene
484 boundary conditions⁵⁸ and have been run for a further 2000 years. Supplementary Figures S65-

485 S68 show the evolution of deep water temperatures throughout the simulations and give us
486 confidence that they have stabilised sufficiently for us to draw conclusions.

487 **References**

- 488 51. Cox, P. M. Description on the TRIFFID Dynamic Global Vegetation Model. *Technical*
489 *Report 24* (Hadley Centre, Met Office, 2001).
- 490 52. Gordon, C. *et al.* The simulation of SST, sea ice extents and ocean heat transports in a
491 version of the Hadley Centre coupled model without flux adjustments. *Clim. Dyn.* **16**,
492 147–168 (2000).
- 493 53. Jones, C. A fast ocean GCM without flux adjustments. *J. Atmos. Ocean. Technol.* **20**,
494 1857–1868 (2003).
- 495 54. Gent, P. R. & McWilliams, J. C. Isopycnal mixing in ocean circulation models. *J. Phys.*
496 *Oceanogr.* **20**, 150–155 (1990).
- 497 55. Pacanowski, R. & Philander, S. Parameterization of vertical mixing in numerical models
498 of tropical oceans. *J. Phys. Oceanogr.* **11**, 1443–1451 (1981).
- 499 56. De Boer, A. M. & Hogg, A. M. Control of the glacial carbon budget by topographically
500 induced mixing. *Geophys. Res. Lett.* **41**, 4277–4284 (2014).
- 501 57. Markwick, P. J. The palaeogeographic and palaeoclimatic significance of climate proxies
502 for data-model comparisons. in *Deep-Time Perspectives on Climate Change: Marrying the*
503 *Signal from Computer Models and Biological Proxies* 251–312 (The Geological Society,
504 2007).

505 58. Bradshaw, C. D. *et al.* The relative roles of CO₂ and palaeogeography in determining late
506 Miocene climate: results from a terrestrial model-data comparison. *Clim. Past* **8**, 715–786
507 (2012).

508

509 **Code Availability**

510 The UK Met Office made available the source code of HadCM3 via the Ported Unified Model
511 release (<http://www.metoffice.gov.uk/research/collaboration/um-partnership>). Enquiries
512 regarding the use of HadCM3 should be directed in the first instance to the UM Partnership team,
513 who can be contacted at um_collaboration@metoffice.gov.uk. The main repository for the Met
514 Office Unified Model (UM) version corresponding to the model presented here can be viewed at
515 http://cms.ncas.ac.uk/code_browsers/UM4.5/UMbrowser/index.html. The code detailing the
516 changes required to update HadCM3 to HadCM3LB-M2.1 are available as a Supplement to
517 Valdes *et al.* (2017)²⁸.

518 **Data Availability**

519 The climate model output data is available for analysis and download at
520 https://www.paleo.bristol.ac.uk/ummodel/scripts/papers/Bradshaw_et_al_2021.html. It is
521 possible to reproduce the information in Fig. 2, Fig. 3, Fig. 5 and Fig. 6 via this interface as well
522 as download the data itself and the ancillary information (paleogeography and ice sheet
523 configuration).

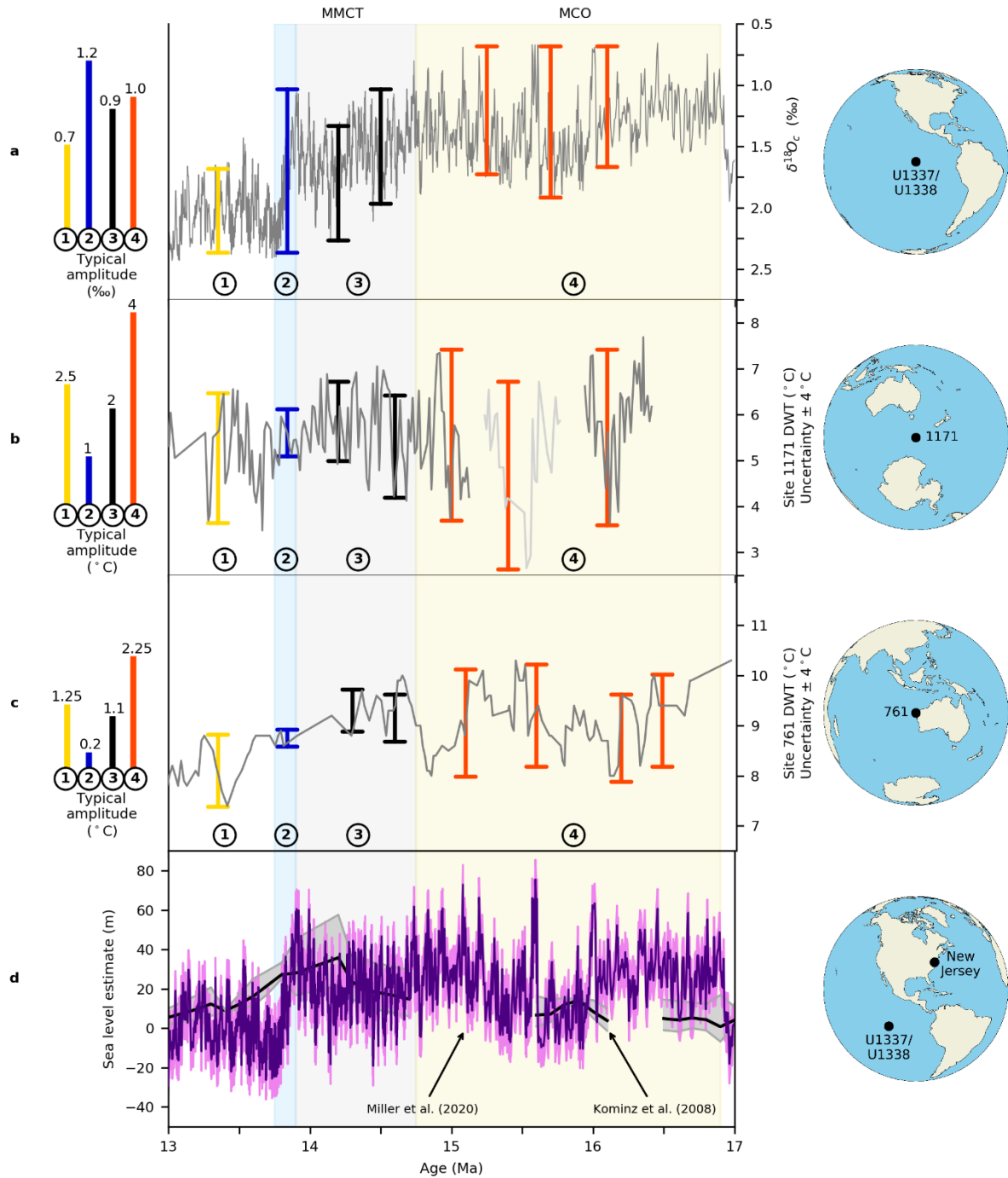


Fig. 1. Mid-Miocene benthic (*Cibicidoides* spp.) oxygen isotope, deep water temperatures (DWT) and sea level changes. a $\delta^{18}\text{O}_c$ splice⁴⁸, b Site 1171 DWT²⁵, Southern Ocean (Antarctica-proximal), c Site 761 DWT⁸, Indian Ocean (Antarctica-distal but in AABW path). Data locations shown on right of panels. DWTs are Mg/Ca reconstructions (uncertainty $\pm 4^\circ\text{C}$; relative values are considered more robust than absolutes). Other available DWT records are too low resolution/short. Data are plotted on their respective age models (full

details: Supplementary Table S11). **d** Sea level^{11,14} (Eustatic estimates¹⁴ x1.48 c.f.⁴⁹).

Shading: Miocene Climatic Optimum (MCO, yellow), middle Miocene Climatic Transition (MMCT, blue+grey), major ice growth event (MMCT, blue). Vertical lines are indicative of the typical maximum $\delta^{18}\text{O}_c/\text{DWT}$ amplitudes during the MCO (4), MMCT prior to the major ice growth event (3), MMCT major ice growth event (2) and post- MMCT (1). Since the data cover different times and resolutions, these lines are not coincident in time between panels a-

c.

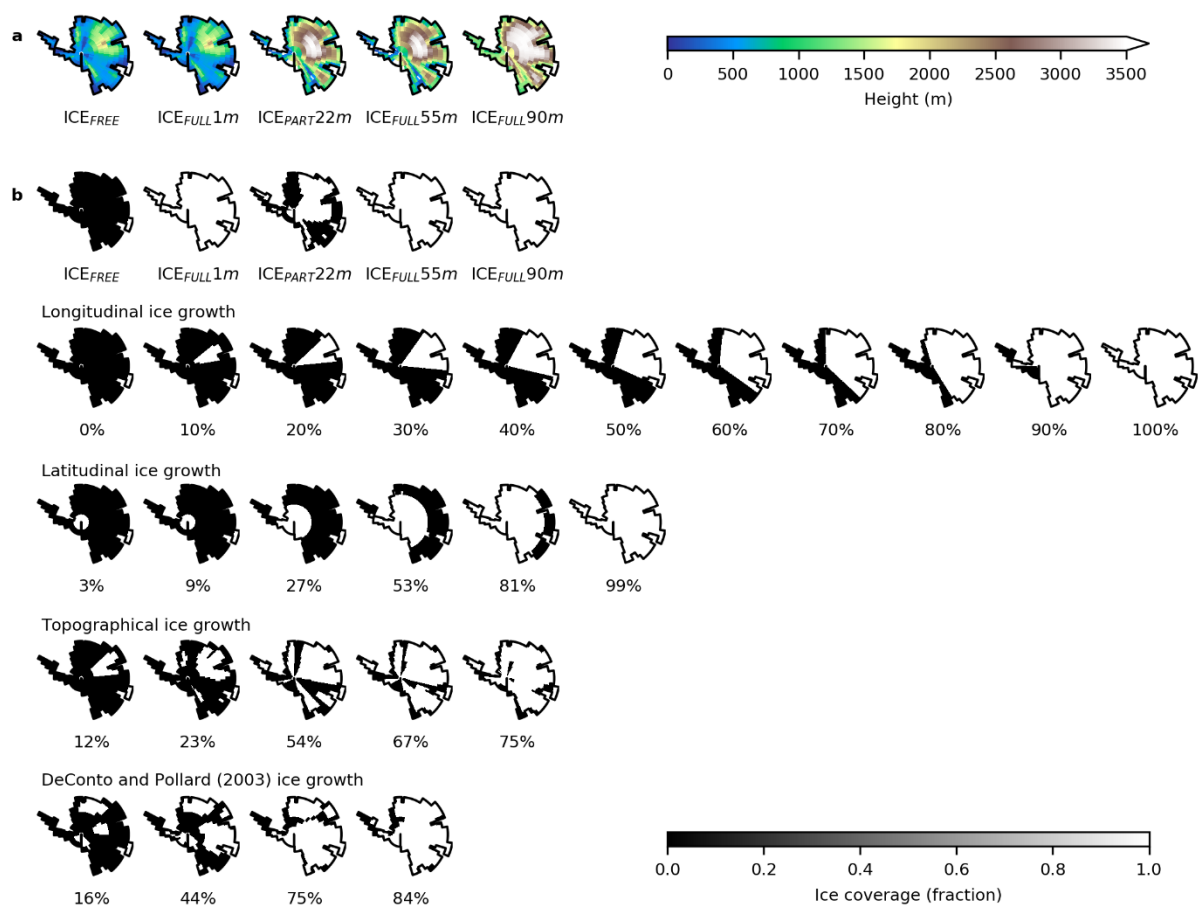


Fig. 2. Orography and ice sheet configurations. **a** Orography for the different ice volume scenarios simulated (sea level equivalent, S.L.E.). **b** Ice cover fraction for the different scenarios simulated. The latitudinal, longitudinal, topographical and DeConto and Pollard 2003⁵⁰ ice sheet extents all use the 1m S.L.E. orography from **a**. The percentage of ice cover is shown under each thumbnail. Refer also to Methods for more information.

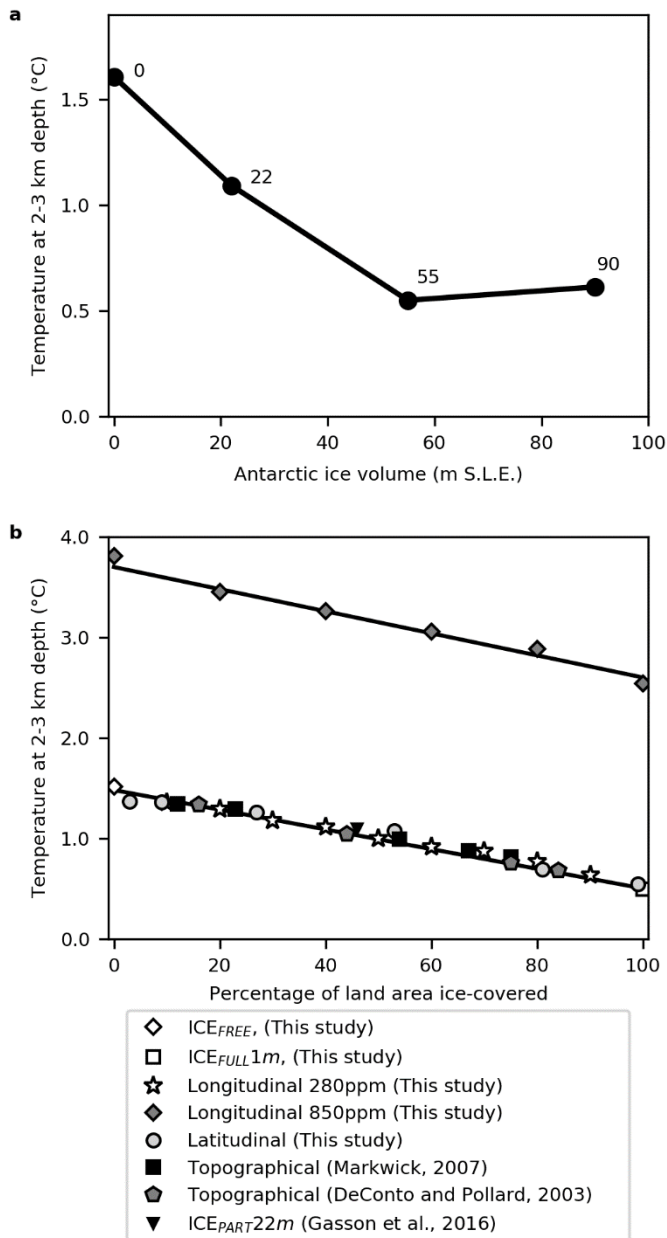


Fig. 3. Annual mean Southern Hemisphere deep water temperatures estimates averaged between 2 and 3 km, simulated with different sized Antarctic ice sheets. a Changing ice sheet volume: ice-free (ICE_{FREE}), the 22 m sea level equivalent (S.L.E.) regional scale ice sheet configuration (ICE_{PART22m}), the 55 m S.L.E. continental ice sheet configuration (ICE_{FULL55m}), and the 90 m S.L.E. continental scale ice sheet configuration (ICE_{FULL90m}), **b** Changing ice sheet extent: different scenarios between 0% and 100% ice covered (refer to Fig. 2 for details). CO₂ is 280 ppm in all cases unless specified and a modern orbit assumed; refer to Methods for more information.

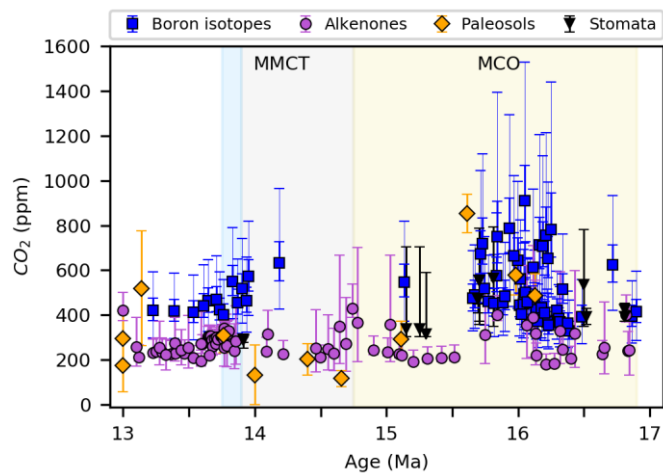


Fig. 4. Middle Miocene atmospheric CO₂ reconstructions. Data provided in Supplementary Table S5 plotted on respective age models. Shading: Miocene Climatic Optimum (MCO, yellow), middle Miocene Climatic Transition (MMCT, blue+grey), major ice growth event (MMCT, blue). Note: the Boron isotope-based CO₂ reconstructions from Soudian et al., 2018³² plotted are from the L02 scenario and shows two error ranges: the 66% (thicker blue lines) and 95% (thinner blue lines) confidence intervals. This dataset supercedes the data from some other publications as documented in Supplementary Table S5 (the reconstructions from the original publications are not plotted).

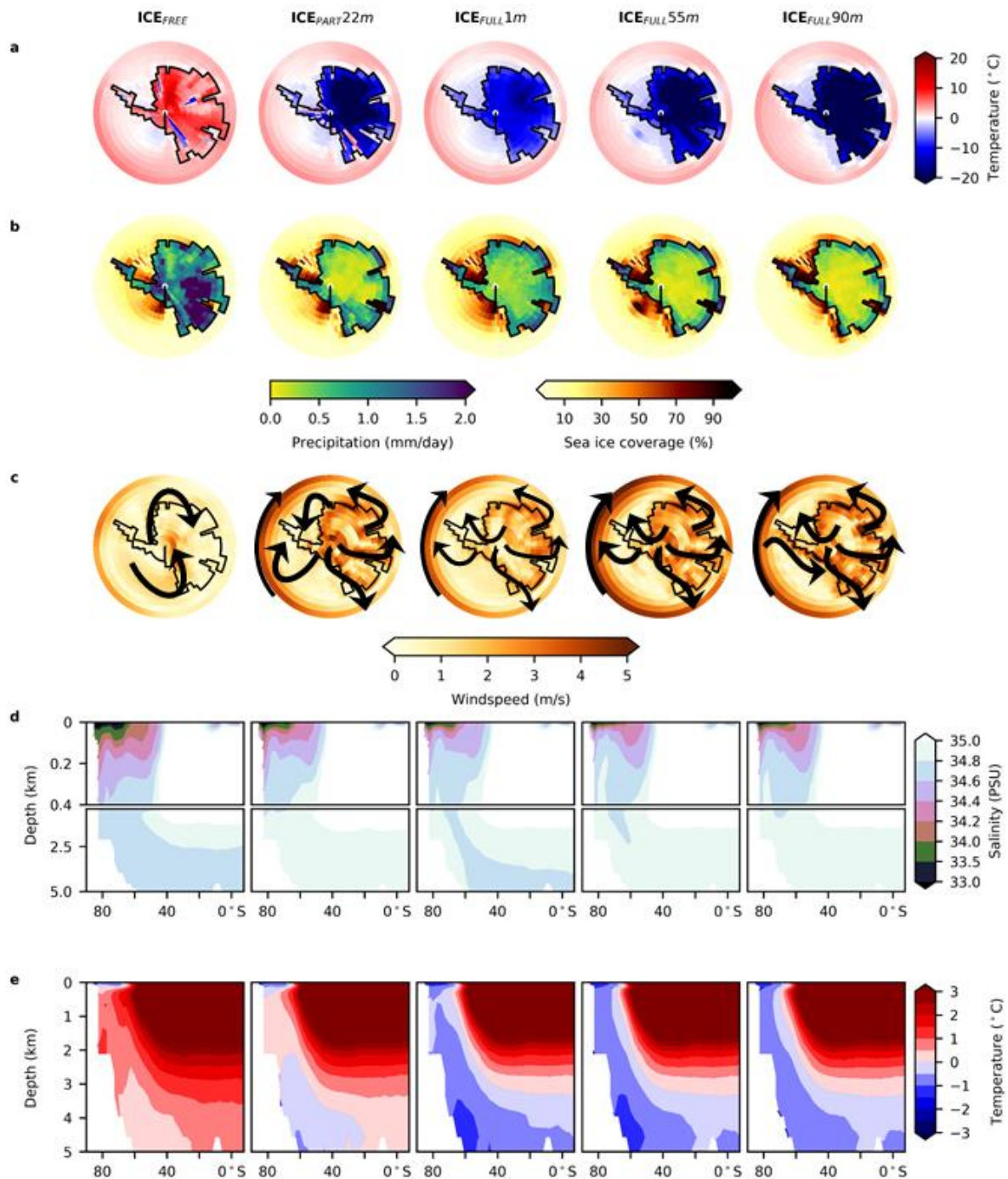


Fig. 5. Simulated atmospheric and oceanographic conditions with different sized Antarctic ice sheets. **a**, Summer (DJF) air temperature, **b**, Summer precipitation (land only shown) and sea ice fraction, **c**, Summer windspeed and prevailing directions, **d**, Annual mean Southern Hemisphere meridional mean ocean salinity, **e**, Annual mean Southern Hemisphere meridional mean ocean temperature. Scenario ICE_{FREE} has no ice sheet, $ICE_{PART22m}$ is a regional scale 22m S.L.E. ice sheet, and ICE_{FULL1m} , $ICE_{FULL55m}$ and $ICE_{FULL90m}$ are 1m

S.L.E., 55m and 90m S.L.E. continental size ice sheets respectively. Refer to Methods and Fig. 2 for more details of the boundary conditions used. CO₂ is 280 ppm in all cases.

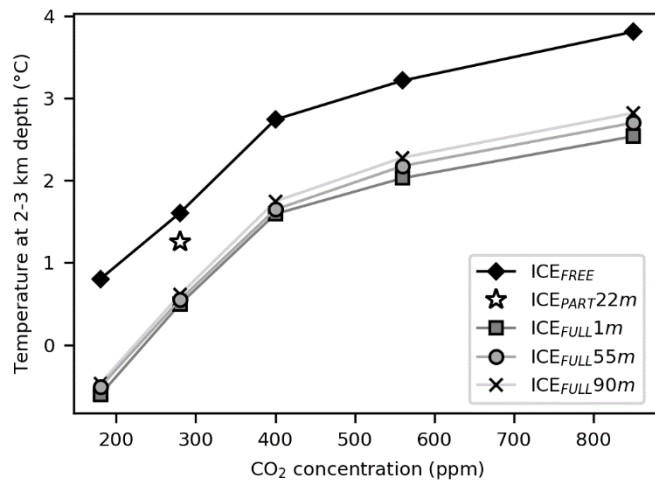


Fig. 6. Annual mean Southern Hemisphere simulated with different sized Antarctic ice sheets and CO₂ concentration. Deep water temperatures are averaged between 2 and 3 km water depth. Ice sheet configurations as in Fig. 5. Refer to Methods and Fig. 2 for more details of the boundary conditions used.

Hydrological impact of Middle Miocene Antarctic ice-free areas coupled to deep ocean temperatures: Supplementary Information

Catherine D. Bradshaw, Petra M. Langebroek, Caroline H. Lear, Daniel J. Lunt, Helen K. Coxall,
Sindia M. Sosdian, Agatha M. de Boer.

Contents:

S1. Supplementary Note: Model-data comparison

Method (Supplementary Figures S1) page 8

Mean annual air temperature (Supplementary Figures S2 to S7) page 9 to 14

Mean annual precipitation (Supplementary Figures S8 to S10) page 15 to 17

Summer mean air temperature (Supplementary Figures S11 to S12) page 18 to 19

Summer total precipitation (Supplementary Figures S13 to S14) page 20 to 21

Mean annual sea surface temperature (Supplementary Figures S15 to S29) page 22 to 36

Maximum monthly sea surface temperature (Supplementary Figures S30 to S38) page 37 to 45

Annual mean deep water temperature (Supplementary Figures S39 to S47) page 46 to 54

S2. Supplementary Discussion:

A. Ocean response to glaciation (Supplementary Figures S48 to S61) page 55 to 70

B. Middle Miocene Deep water production page 71

C. Relationship between ice sheet volume and ice sheet area (Supplementary Figure S62)
page 72

D. Deep water temperature changes that can be accounted for from CO₂ forcing alone
(Supplementary Tables S1 to S2) page 73

- E. Deep water temperature changes that can be accounted for from surface albedo and roughness forcing alone (Supplementary Tables S3 to S4) page 74
 - F. Sensitivity to orbital configuration (Supplementary Figure S63) page 75 to 76
 - G. A potential mechanism for asynchronous advance of different ice sheet catchments (Supplementary Figure S64) page 77 to 78
 - H. Model spinup (Supplementary Figures S65 to S68) page 79 to 80
- S3. Supplementary Information References page 81

S1. Supplementary Note

Model-Data Comparison

Methodology

There are many difficulties associated with developing a model-data comparison methodology, and in the interpretation of results. The model-data comparison methodology adopted follows previous work for the late Miocene^{1,2}. Terrestrial data reconstructions are given in Supplementary Tables S6-9, sea surface temperature (SST) estimates are given in Supplementary Table S10 and deep water temperature (DWT) estimates are given in Supplementary Table S11. Due to the higher temporal resolution of the marine data as compared to the terrestrial data, two slightly different approaches are used. Core-based terrestrial data, being of higher resolution and better age constraint, are additionally treated the same as SST data.

For the terrestrial data:

- Mean annual temperature and precipitation reconstructions are split into two timeslices of 13-14.5 Ma (icehouse) and 14.5 -16.75 Ma (greenhouse) in order to attempt to identify any differences between the MMCT and the MCO. Where age uncertainty is large data will appear in both timeslices and these data are treated separately.
- Within each timeslice, the minimum and maximum temperature and precipitation estimates for each site are retained, and the calibration uncertainty added (where the calibration uncertainty has not been stated by the original author, an uncertainty of 1°C has been assumed).
- Each individual proxy location has been translated back to an estimated paleolocation as dictated by the age control. With the exception of the data taken from Goldner et al., 2014³ (which is used as is because the original latitude and longitude values were not provided), the same paleorotation has been used as the construction of the Middle Miocene paleogeography⁴ to ensure consistency with the model results. Given the uncertainties in the dating of most terrestrial data, the middle of the age ranges has been used.

- All grid cells adjacent to the grid cell containing the paleodata are used to derive the model values. Taking this approach allows for data location uncertainties such as transportation and paleorotation, and allows for model uncertainties in the placement of largescale climate features (it is unreasonable to expect a GCM to reconstruct the exact climate at a single grid cell; greater reliance should be placed on broad-scale patterns).
- Where terrestrial reconstructions have been derived from marine core data, the datapoint location has been manually moved to the nearest land grid cell.
- We remove one of the data from the Goldner et al., 2014³ synthesis for the Falkland Islands since this is not resolved as land in our model.

For the marine data:

- Uncertainty estimates are added to the seawater temperature estimate at each datapoint at each site. Although there are many different calibration equations, assumptions about the past seawater conditions and dissolution depth-corrections, we have used the temperature estimates from the original sources. An element of the remaining inconsistencies between the model output and the data could therefore be related to these uncertainties unaccounted for here. For example, the uncertainty in DWT in the Mg/Ca proxy reconstructions at Site 1171 arising just from using a different calibration equation are of the order $\sim 2^{\circ}\text{C}^5$.
- Typically, calibration uncertainties derived from modern Mg/Ca-temperature calibrations are on the order of $\pm 1^{\circ}\text{C}$. However, there are other controls on foraminiferal Mg/Ca that have been dealt with in different ways in the literature. For example, variations in seawater Mg/Ca will impact both benthic and planktonic foraminiferal Mg/Ca. Epifaunal species of benthic foraminifera may be sensitive to changes in bottom water carbonate saturation state⁶. Planktonic foraminiferal Mg/Ca may be sensitive to change in sea surface pH and salinity⁷. It is impossible to correct all previously published records for such effects, as they have not been published with the required additional data (e.g., benthic foraminiferal B/Ca, planktonic foraminiferal $\delta^{11}\text{B}$). Instead, we therefore increase the uncertainty on absolute temperature estimates from $\pm 1^{\circ}\text{C}$ to $\pm 4^{\circ}\text{C}$ to include any potential bias from these sources. This large uncertainty window applies to absolute

temperatures – reconstructed relative changes in downcore temperatures such as those shown in Fig. 1 have smaller uncertainties.

- Each individual proxy location has been translated back to an estimated paleolocation as dictated by the age control.
- All grid cells adjacent to the grid cell containing the paleodata are used to derive the model values (horizontally and vertically).
- The SST reconstructions are compared to the simulated mean annual temperatures of the surface ocean. In addition, to allow for any seasonal bias in production, the high latitude sites are also compared to the simulated maximum temperatures of the surface ocean.
- The DWT reconstructions are compared to the simulated mean annual temperature at the estimated paleodepths of the core sites.
- As the authors do not specify which of the reconstructed DWT relationships to use, both reconstructions suggested by Lear et al., 2010⁸ (adjusted and unadjusted for assumed changes in saturation state) and both reconstructions suggested by Lear et al., 2015⁹ (linear-fitted and exponential-fitted curves) have been plotted.

To reflect the uncertainties in the data reconstructions and the model results, both are treated as a range of possible values and the term overlap is defined as consistency between model and data if their uncertainty ranges overlap (Supplementary Figure S1a). Where the data and model overlap, it is not possible to determine that they are different; it does not necessarily follow that the data and the model are in agreement if the uncertainty ranges are large (Supplementary Figure S1b). Reference made to any differences between the data reconstructions and the model output in this study therefore refer to the minimum possible difference only. No attempt has been made to try to correct for any GCM bias with respect to modern observations. Such a correction is very difficult because of the large gap in age, it is not considered robust to assume that biases in the model for present day conditions would be the same as any biases in the model for conditions ~15 million years ago because of differences in the land-sea mask affecting ocean circulation, and the removal of continental ice from both Greenland and Antarctica in this study.

Results

Mean annual air temperature

The model-data comparisons show that the 853ppm CO₂ concentration simulations all overlap with the icehouse subset data reconstructions (Supplementary Figure S2). There is more data available in the terrestrial greenhouse subset and the subset of data with poor age control, and both of these show the closest overall match to the data occurs with the 560 ppm CO₂ concentration scenario with no Antarctic ice sheet (Supplementary Figures S3 and S4). For the individual sites, the higher CO₂ concentrations scenarios also show the best model-data fit (Supplementary Figures S5 to S7). Notwithstanding the sparse closely-clustered terrestrial data available for the icehouse period, there is, therefore, no evidence from the terrestrial model-data comparison to support a lowering of CO₂ for the MMCT as compared to the MCO. The data reconstructions are mixed though, between being warmer than the model simulations in the high latitudes and colder than the model simulations in the mid-latitudes of Asia, and it is therefore unlikely that there would be a single CO₂ concentration that could improve the terrestrial model-data comparison.

Mean annual precipitation

The limited mean annual precipitation data suggests that all CO₂/ice sheet scenarios overlap with the data reconstructions from the icehouse subset (Supplementary Figure S8) and the subset with poor age control (Supplementary Figure S10). The same is true for the Antarctic data precipitation data reconstructions in the greenhouse subset, but data reconstructions from the New Zealand locations in that timeslice are wetter than the models can reproduce (Supplementary Figure S9).

Summer mean air temperature

All of the CO₂/ice sheet configuration scenarios overlap with the summer mean temperature data reconstructions on Antarctica when the data is considered as a timeslice mean (Supplementary Figures S11). The warmest of the individual datapoints, however, only overlap with the ICE_{FREE} scenario for the 400, 560 and 853 ppm CO₂ concentrations (Supplementary Figure S12).

Summer total precipitation

None of the CO₂/ice sheet configuration scenarios overlap with the summer precipitation data reconstructions on Antarctica when the data is considered as a timeslice mean (Supplementary Figures S13) but the highest CO₂ concentration scenario shows the closest fit (Supplementary Figure S14).

Mean annual sea surface temperature

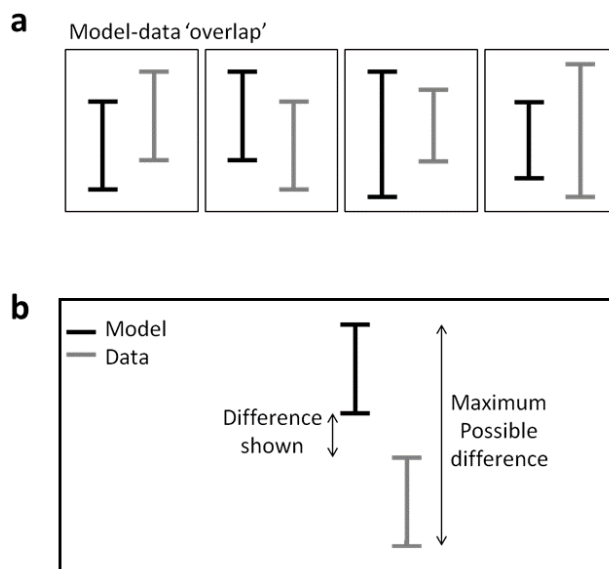
The marine SST model-data comparison shows that the warmest data reconstructions are typically warmer than the model simulations at high latitudes even at the highest CO₂ concentrations tested, but the data reconstructions typically overlap with the model simulations at the lower latitudes, although here it is often restricted to the lower CO₂ concentrations (Supplementary Figures S15 to S29). The model simulations therefore show the same difficulties in reproducing the equator-to-pole temperature gradients reconstructed by the data as other models^{3,10,11}.

Maximum monthly sea surface temperature

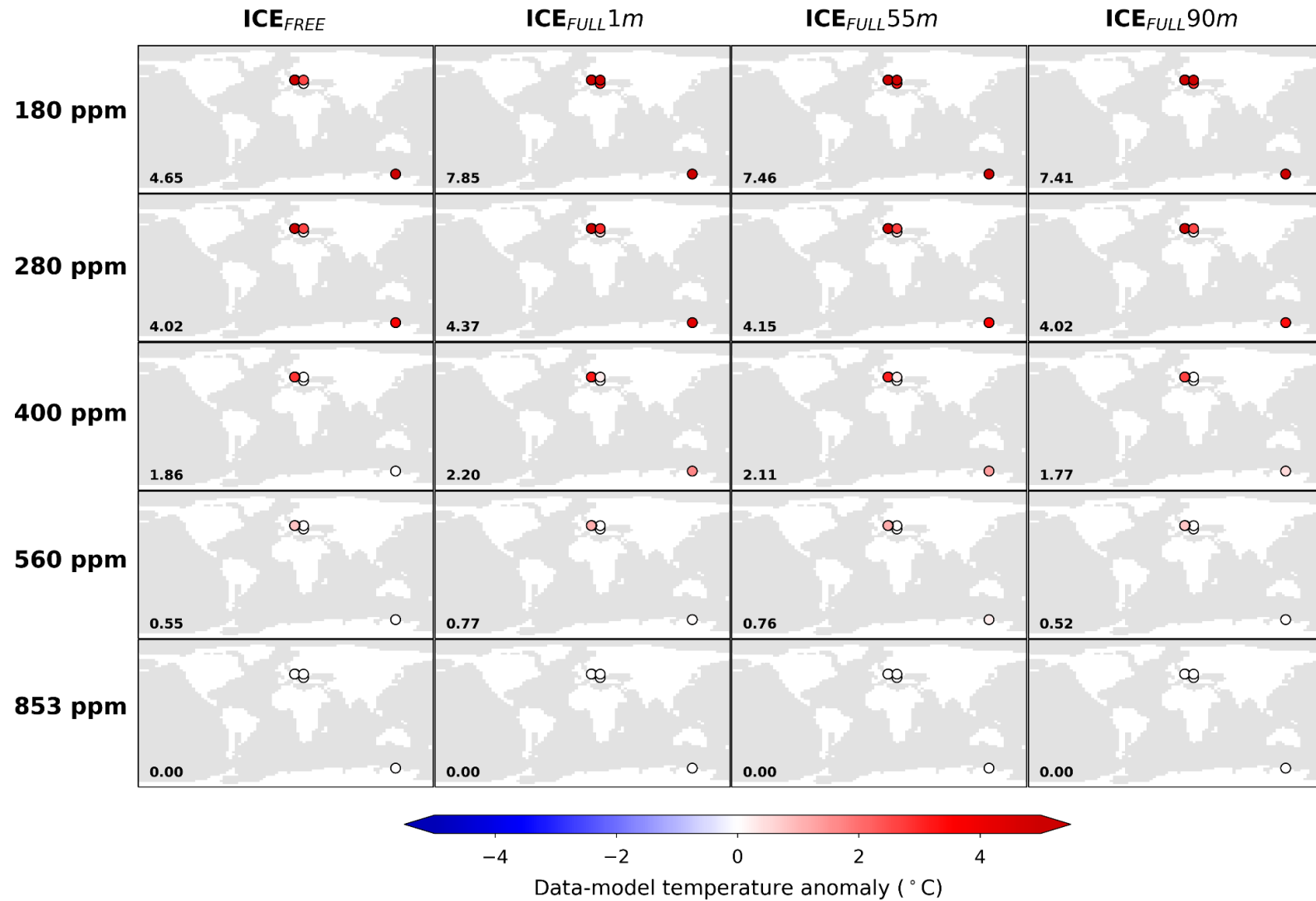
If the high latitude data are assumed to contain a warm-season bias, the cooler icehouse records typically overlap with the model simulations at 280 ppm CO₂ or higher, but the warmer greenhouse records still prove difficult to simulate (Supplementary Figures S30 to S38).

Annual mean deep water temperatures

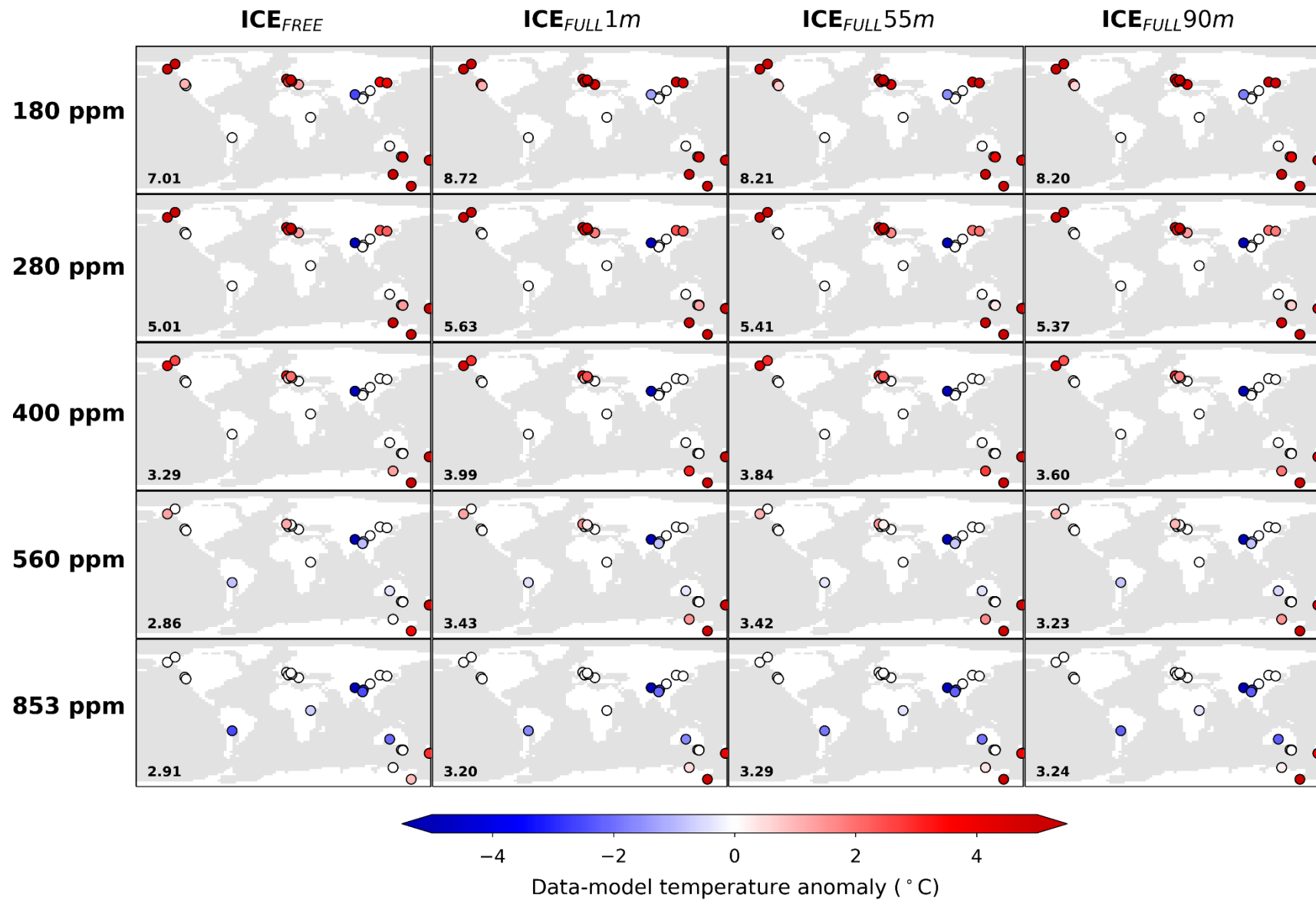
The model simulated deep water temperatures typically overlap with the data reconstructions for all but the warmest of temperatures for the higher CO₂ concentration assumptions (Supplementary Figures S39 to S46).



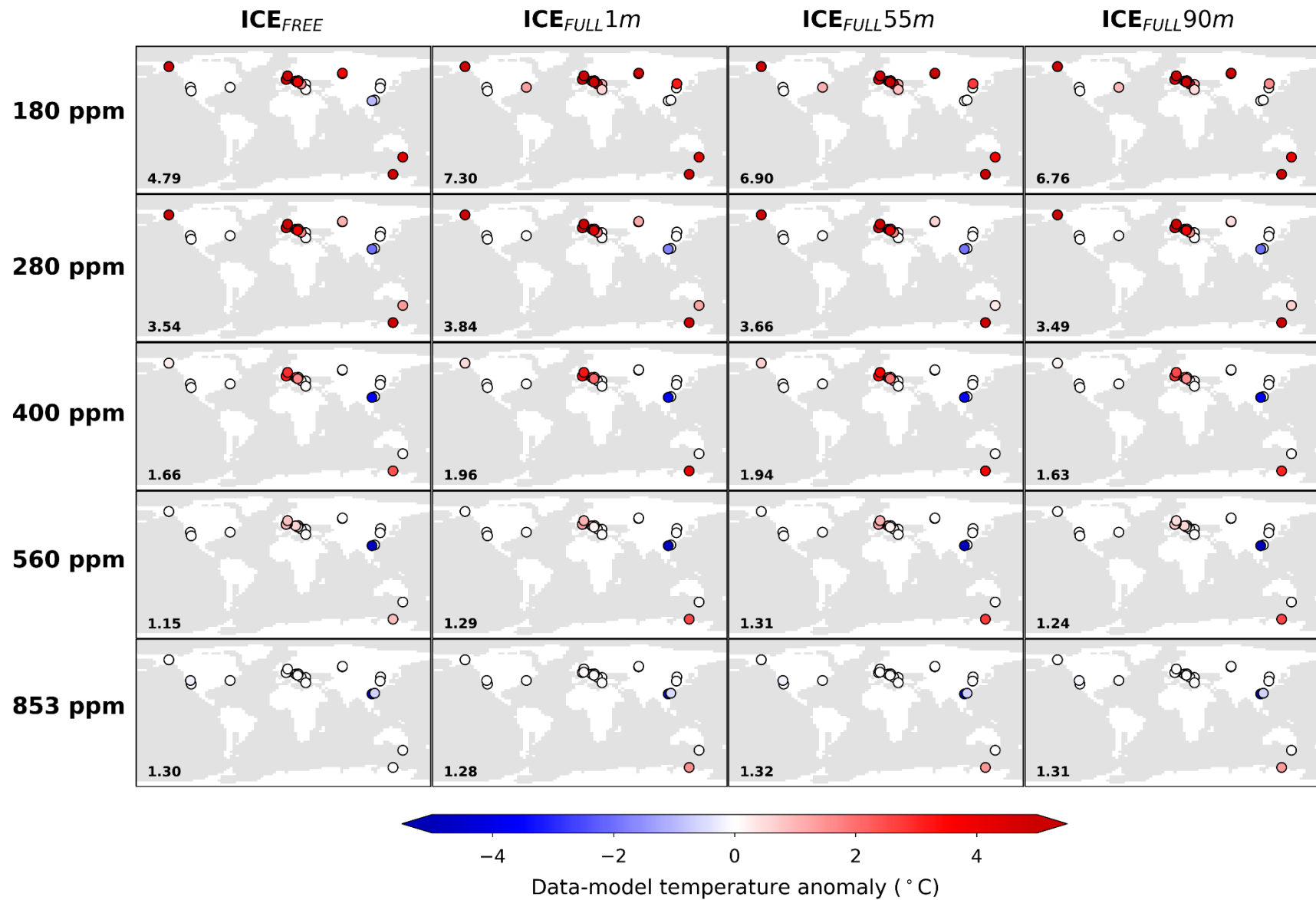
Supplementary Figure S1. Model-data comparison definitions. (a) The definition for “overlap” used in the comparison (all four instances shown are considered as an overlap), (b): Although data-model mismatch is defined as the minimum possible distance to overlap, the maximum possible differences could be much greater if the true values for both the model and the data were to lie at the extremes of the uncertainty ranges.



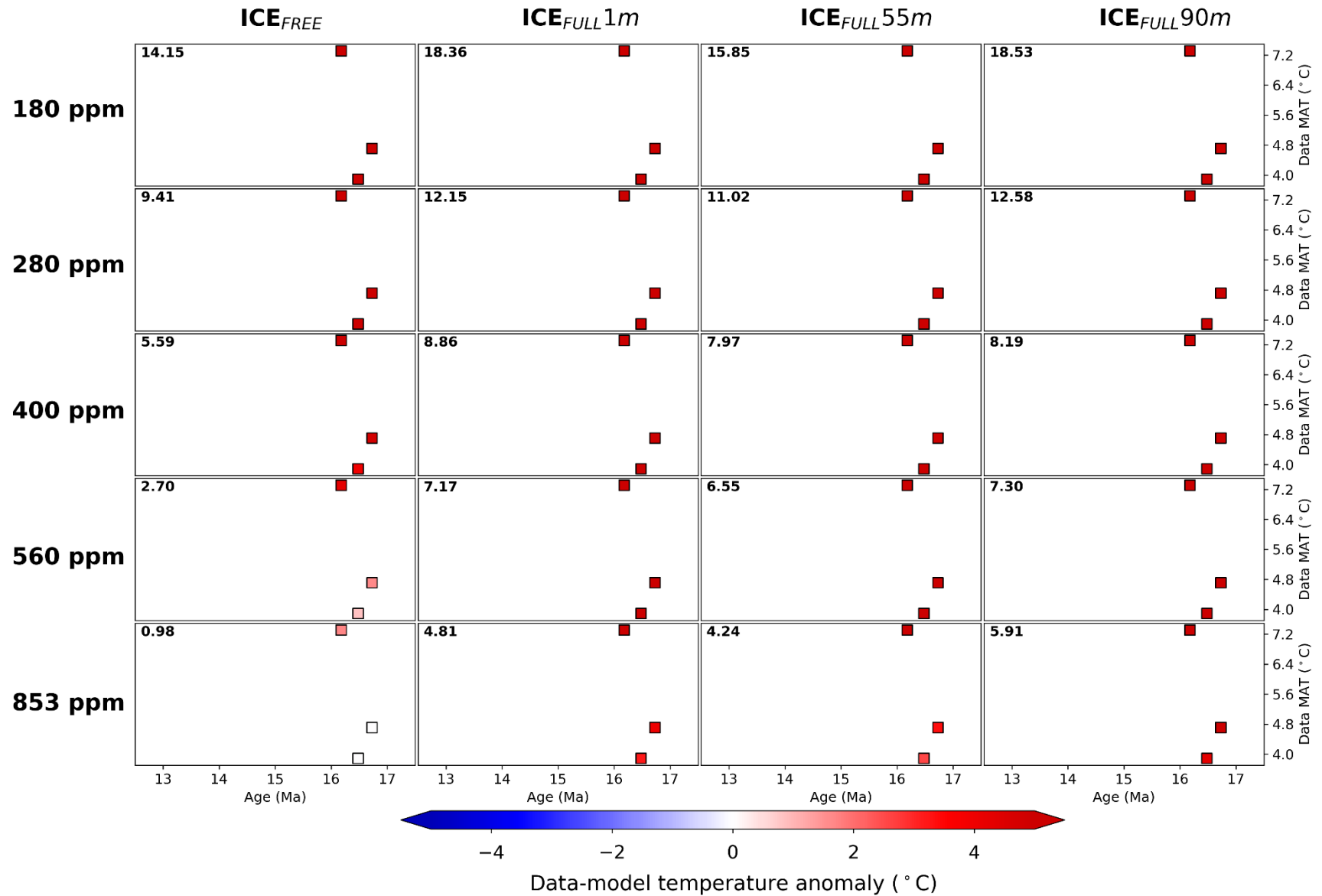
Supplementary Figure S2. Annual mean air temperature model-data comparison for icehouse (13-14.5 Ma) data reconstructions given in Supplementary Table S6. The columns show results for an ice-free Antarctica, a 1m, a 55m and a 90m sea level equivalent Antarctic ice sheet from left to right respectively. The rows show results for atmospheric CO₂ set to 180ppm, 280ppm, 400ppm, 560ppm and 853ppm from top to bottom respectively. The markers are positioned at the mean data reconstruction ages and coloured according to the data-model anomaly (red indicates the data reconstruction is warmer than the model simulates, blue indicates it is cooler and white indicates overlap between the data reconstruction and the model simulation). The RMSE value for the whole synthesis is in the bottom left-hand corner for each scenario.



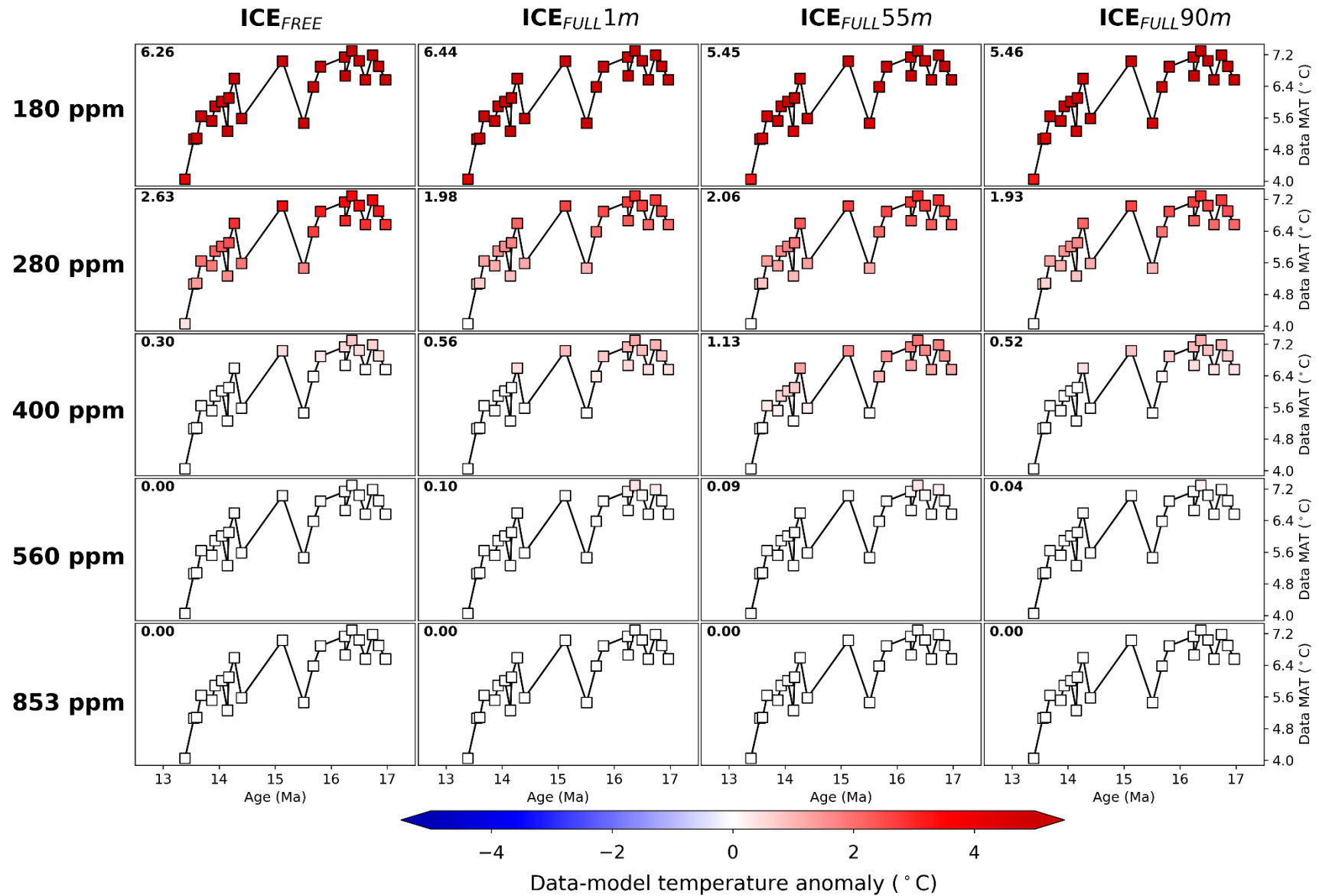
Supplementary Figure S3. Annual mean air temperature model-data comparison for greenhouse (14.5-16.75 Ma) data reconstructions given in Supplementary Table S6. Legend information as in Supplementary Figure S2.



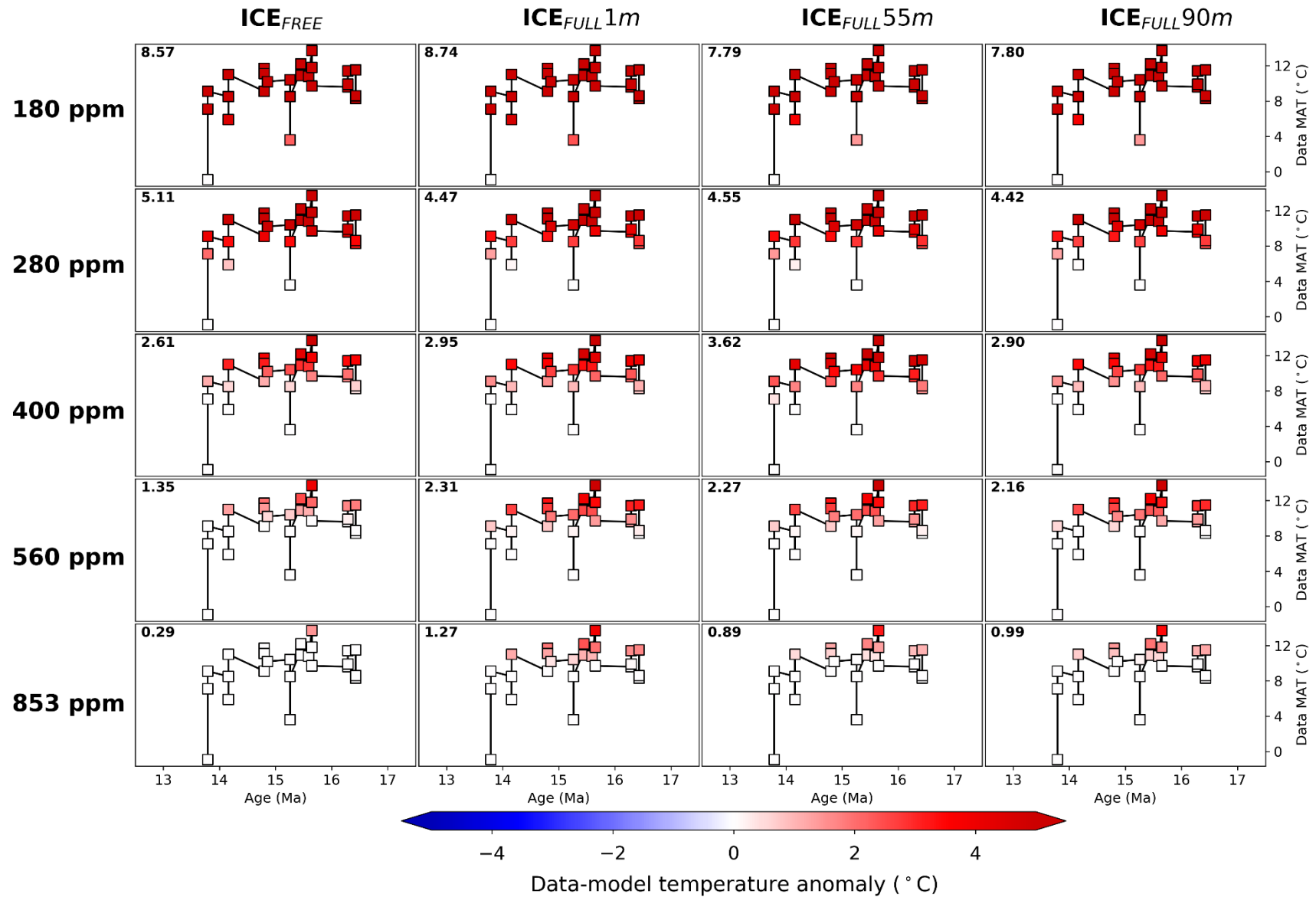
Supplementary Figure S4. Annual mean air temperature model-data comparison for middle Miocene data reconstructions given in Supplementary Table S6 with poor age control. Legend information as in Supplementary Figure S2.



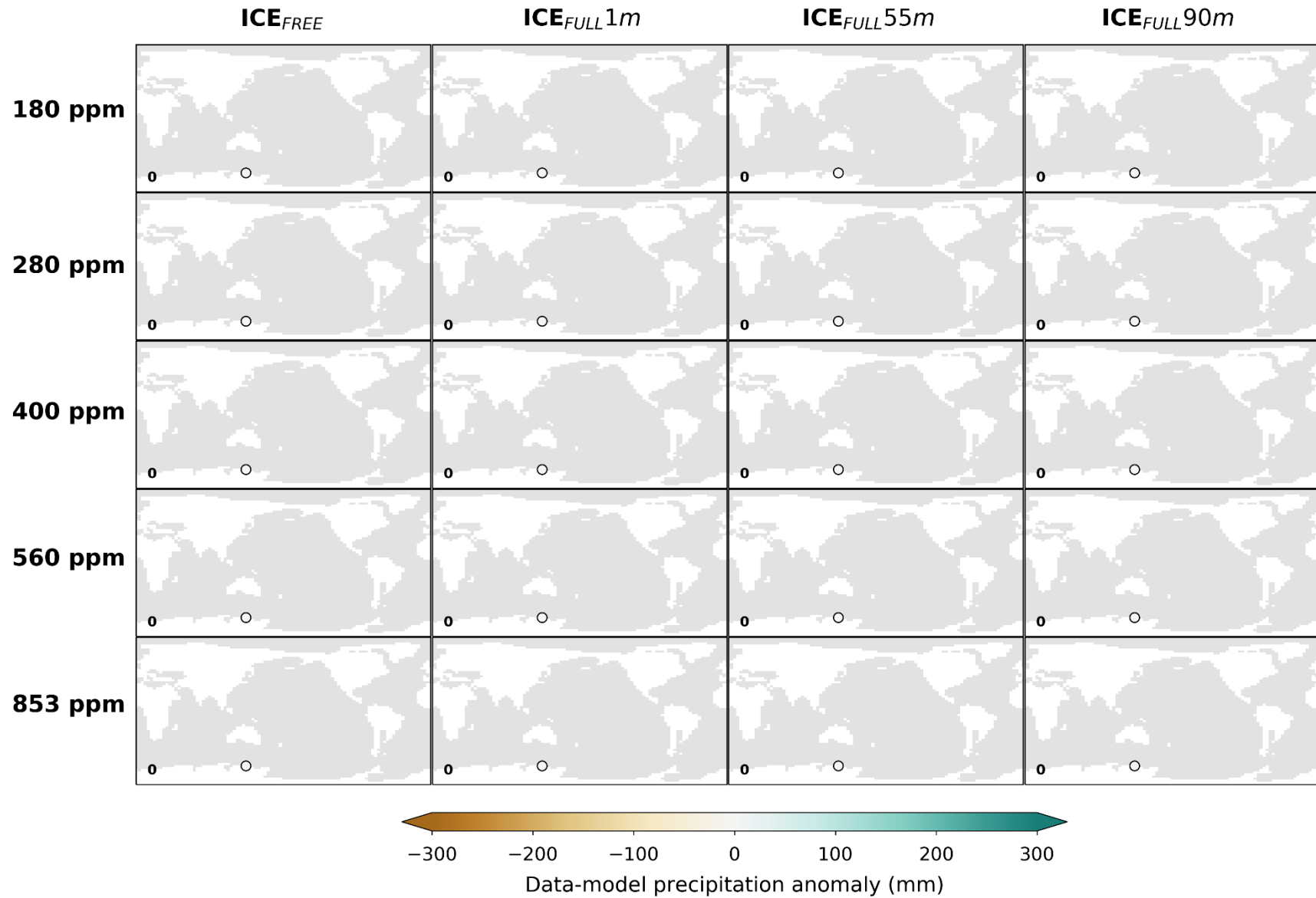
Supplementary Figure S5. Annual mean air temperature model-data comparison for middle Miocene data reconstructions for Site CRP-1 in the Ross Sea. Data from Paschier et al., 2013¹² as given in Supplementary Table S6. Legend information as in Supplementary Figure S2.



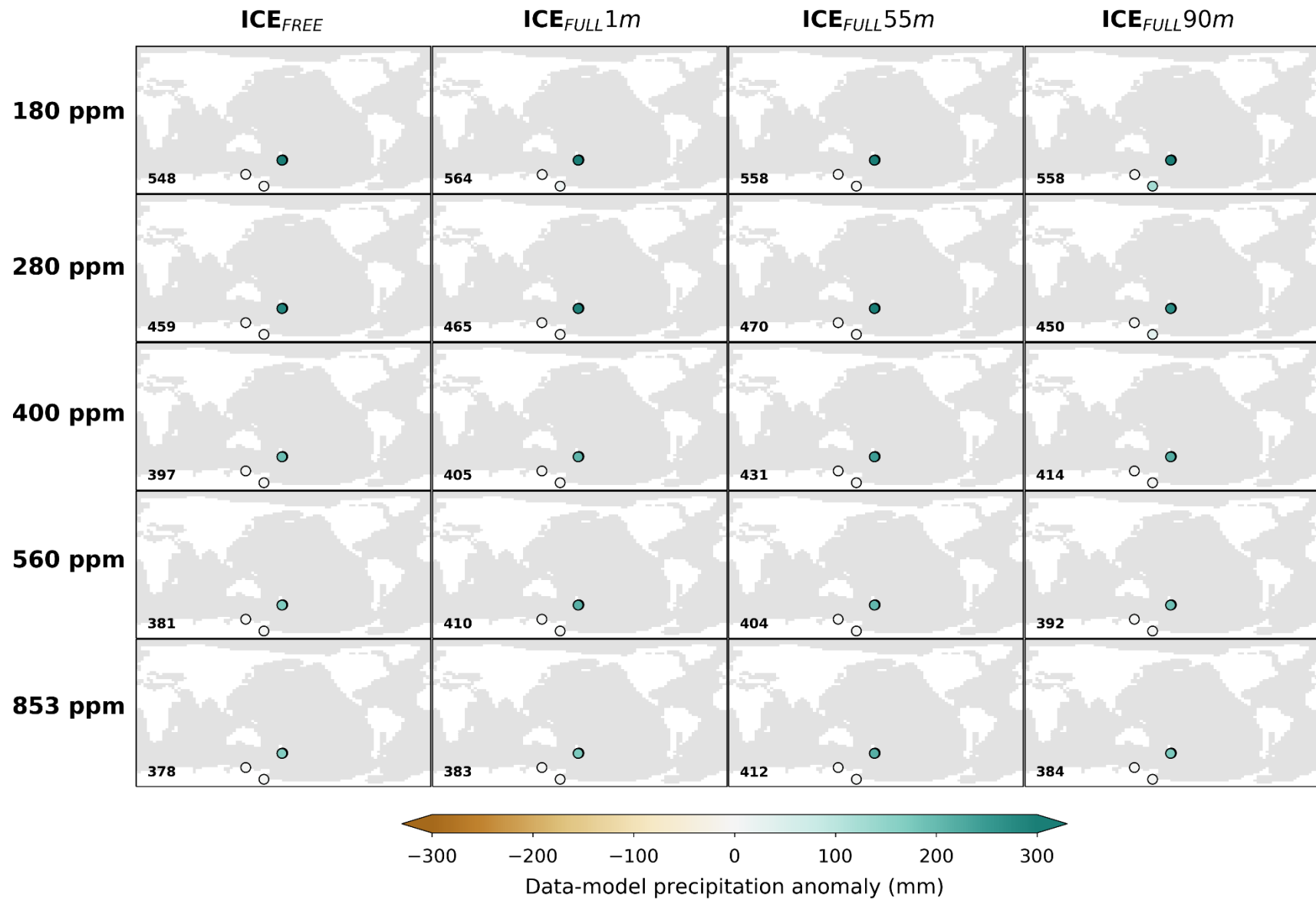
Supplementary Figure S6. Annual mean air temperature model-data comparison for middle Miocene data reconstructions for Site U1356A in the Wilkes Land Continental Margin. Data from Paschier et al., 2013¹² as given in Supplementary Table S6. Legend information as in Supplementary Figure S2.



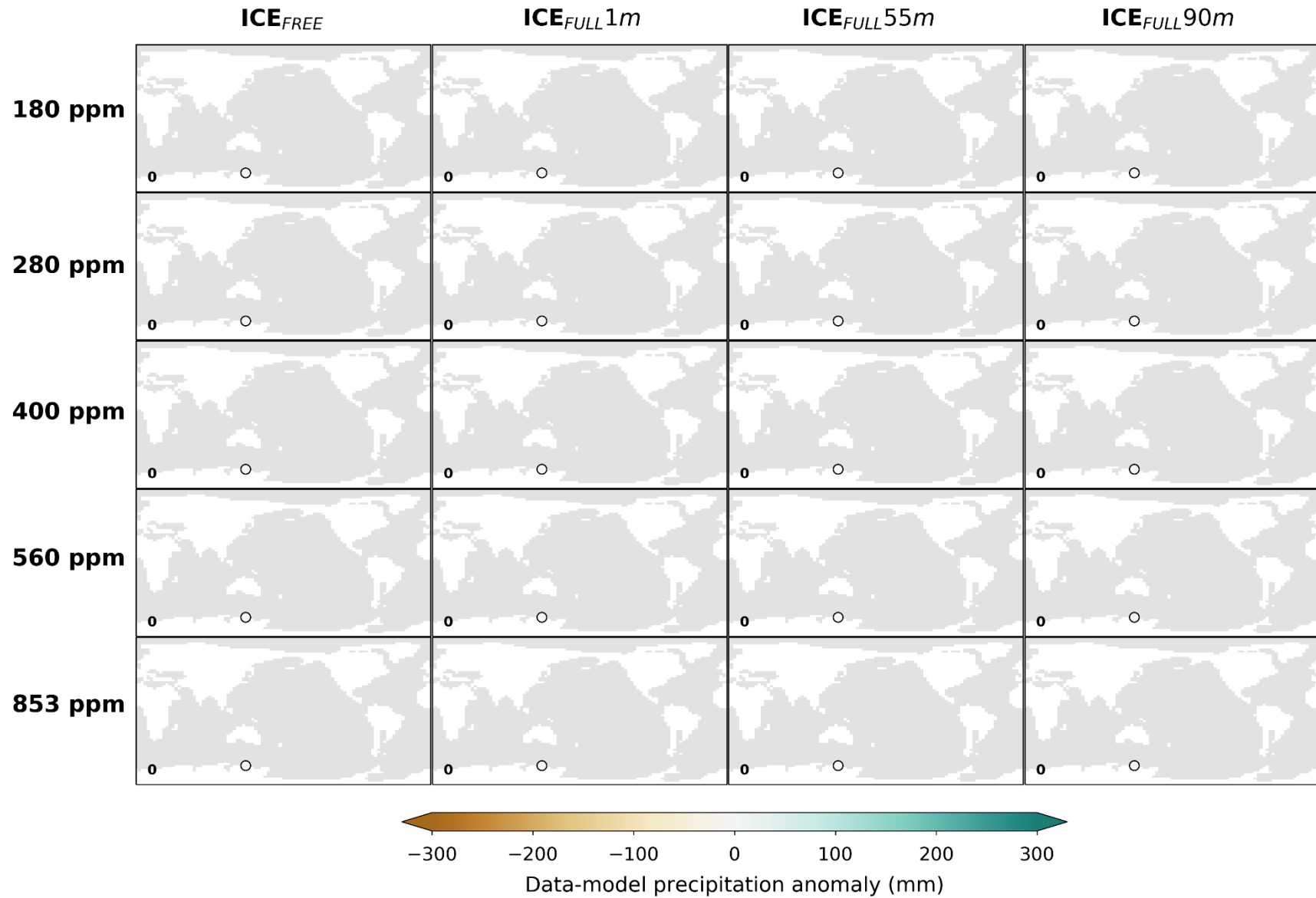
Supplementary Figure S7. Annual mean air temperature model-data comparison for middle Miocene data reconstructions for Site U1356 in the Wilkes Land Continental Margin. Data from Sangiorgi et al., 2018¹³ as given in Supplementary Table S6. Legend information as in Supplementary Figure S2.



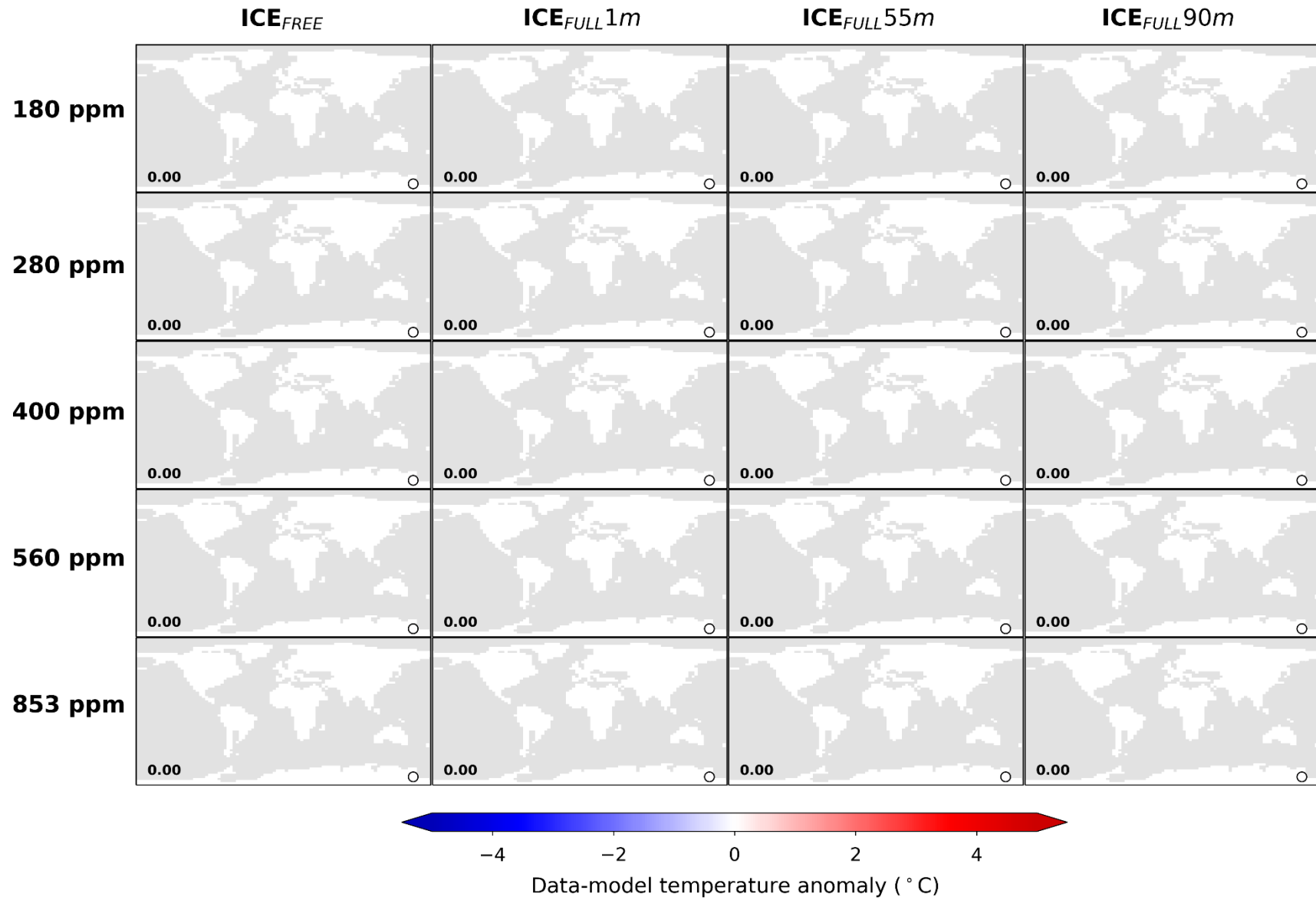
Supplementary Figure S8. Annual mean precipitation model-data comparison for icehouse (13-14.5 Ma) data reconstructions given in Supplementary Table S7. Legend information as in Supplementary Figure S2.



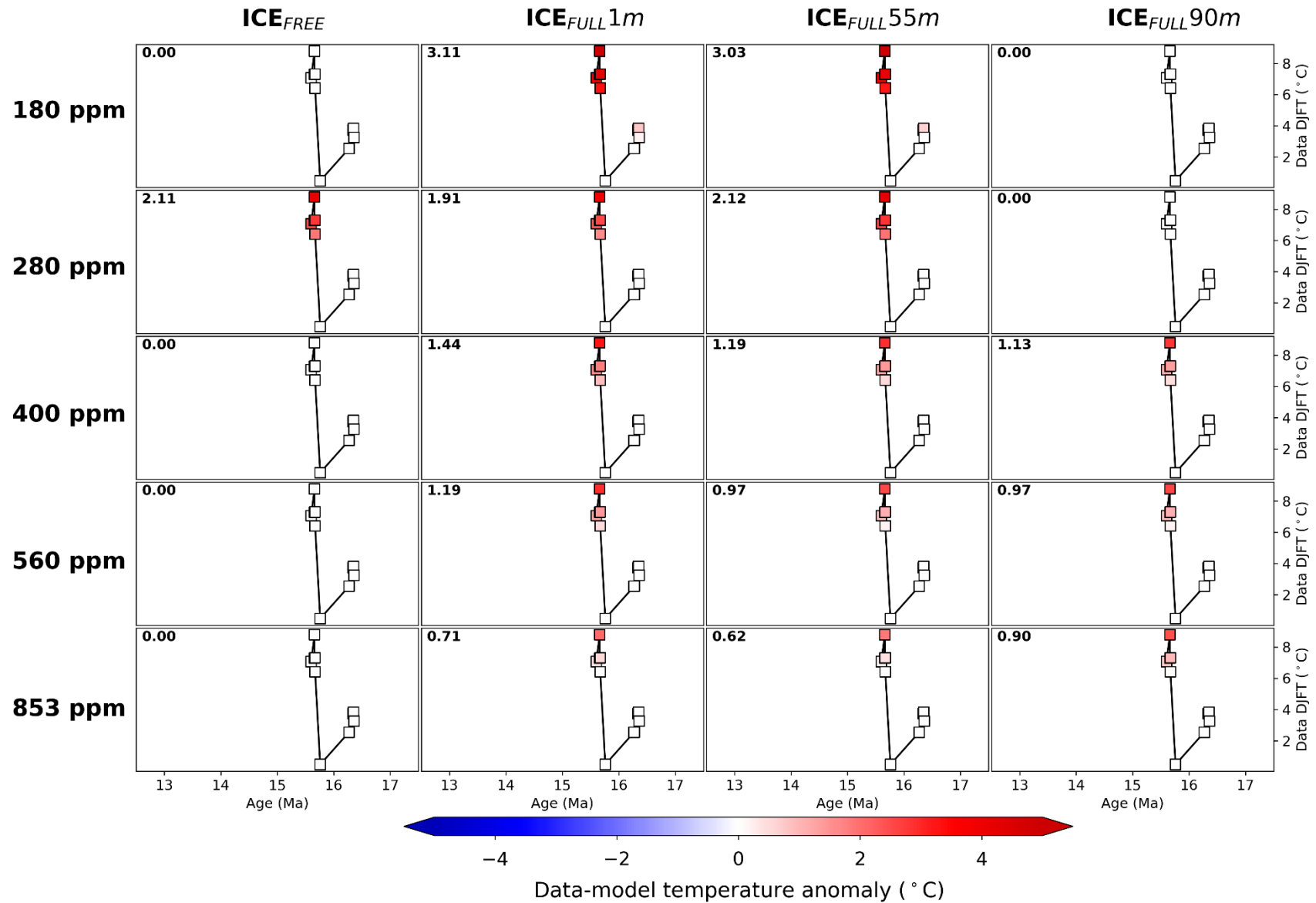
Supplementary Figure S9. Annual mean precipitation model-data comparison for greenhouse (14.5-16.75 Ma) data reconstructions given in Supplementary Table S7. Legend information as in Supplementary Figure S2.



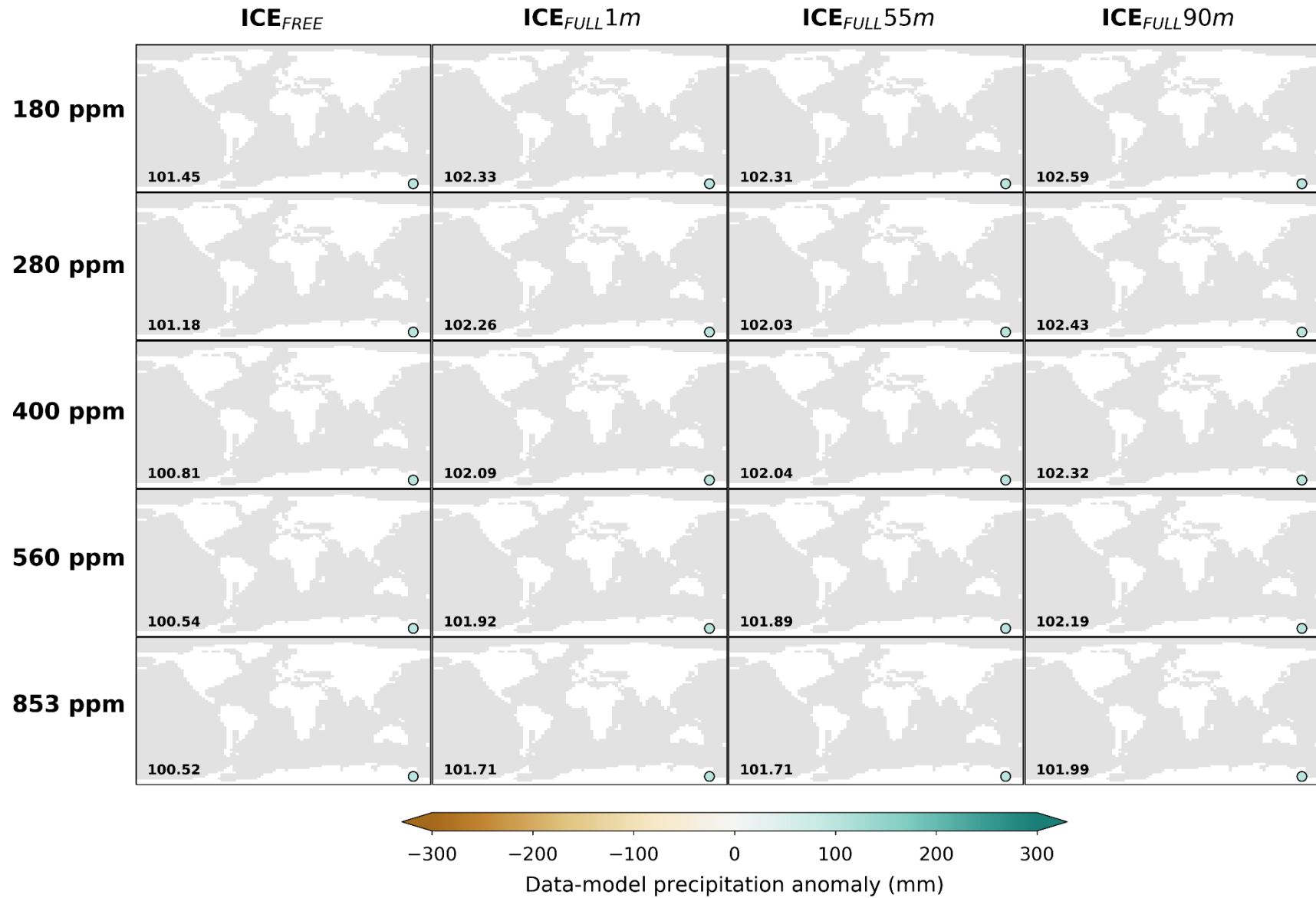
Supplementary Figure S10. Annual mean precipitation model-data comparison for middle Miocene data reconstructions given in Supplementary Table S7 with poor age control. Legend information as in Supplementary Figure S2.



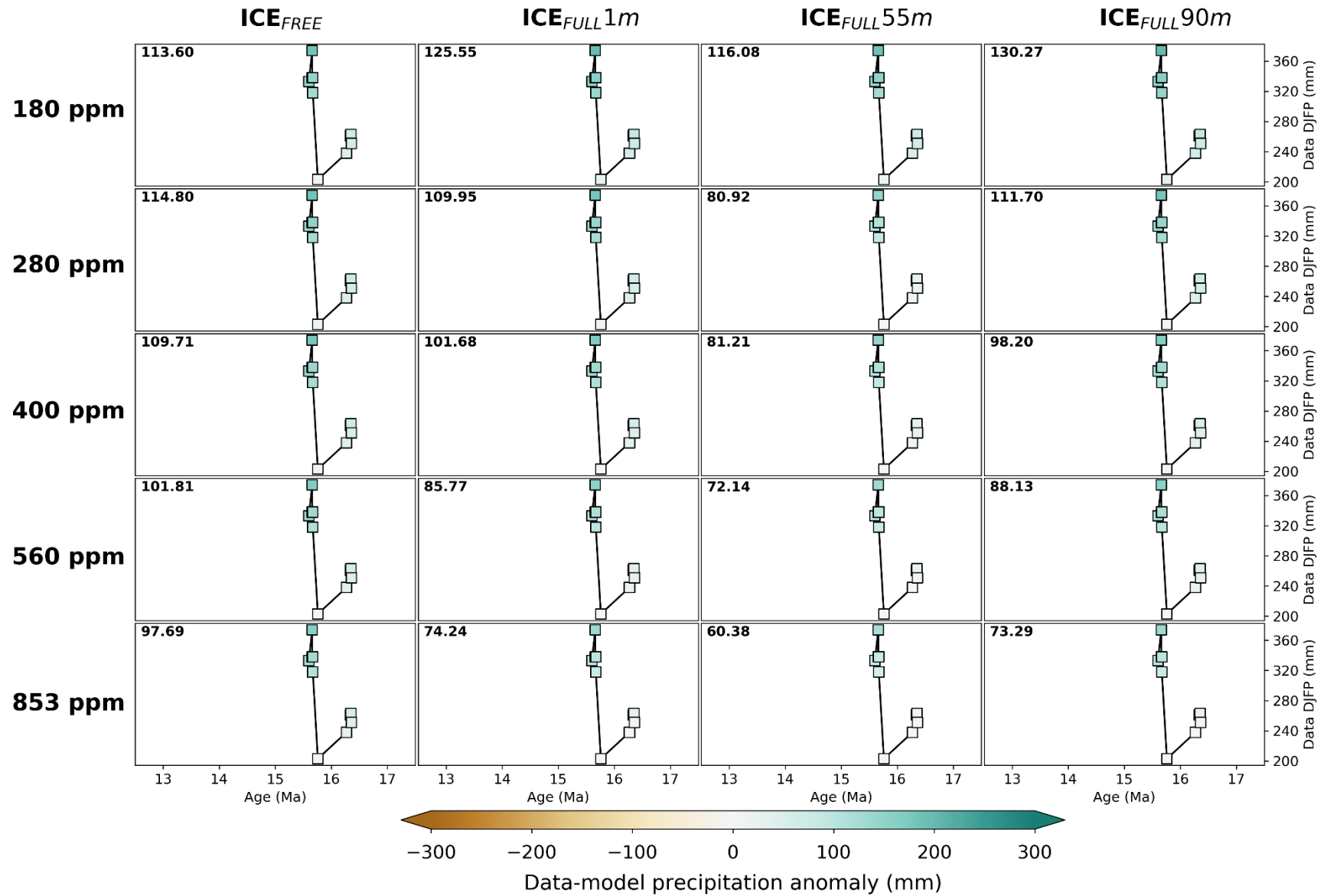
Supplementary Figure S11. Summer (DJF) mean air temperature model-data comparison for greenhouse (14.5-16.75 Ma) data reconstructions given in Supplementary Table S8. Legend information as in Supplementary Figure S2.



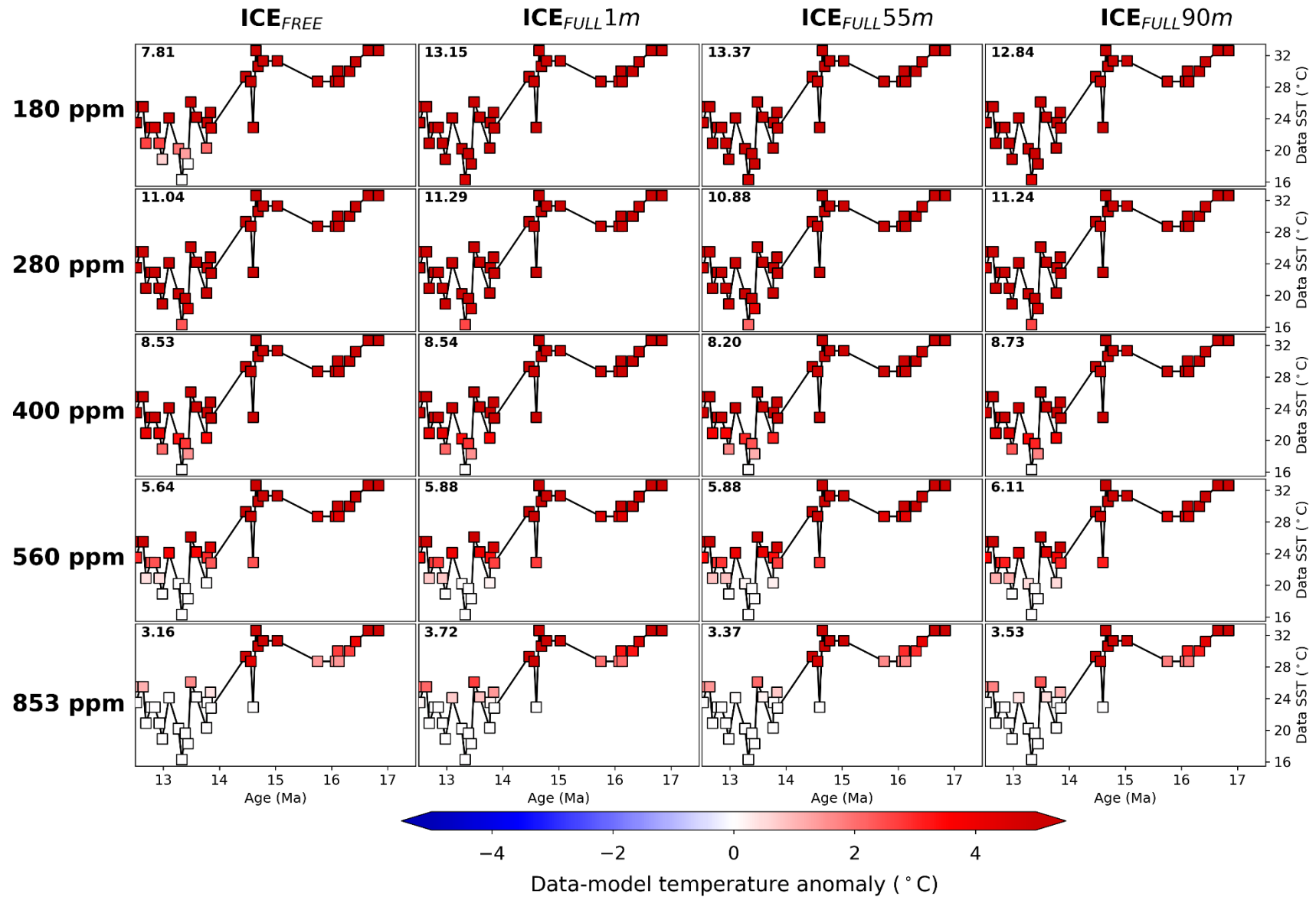
Supplementary Figure S12. Summer (DJF) mean air temperature model-data comparison for middle Miocene data reconstructions for Site AND-2A in the Ross Sea. Data from Feakins et al., 2012¹⁴ as given in Supplementary Table S8. Legend information as in Supplementary Figure S2.



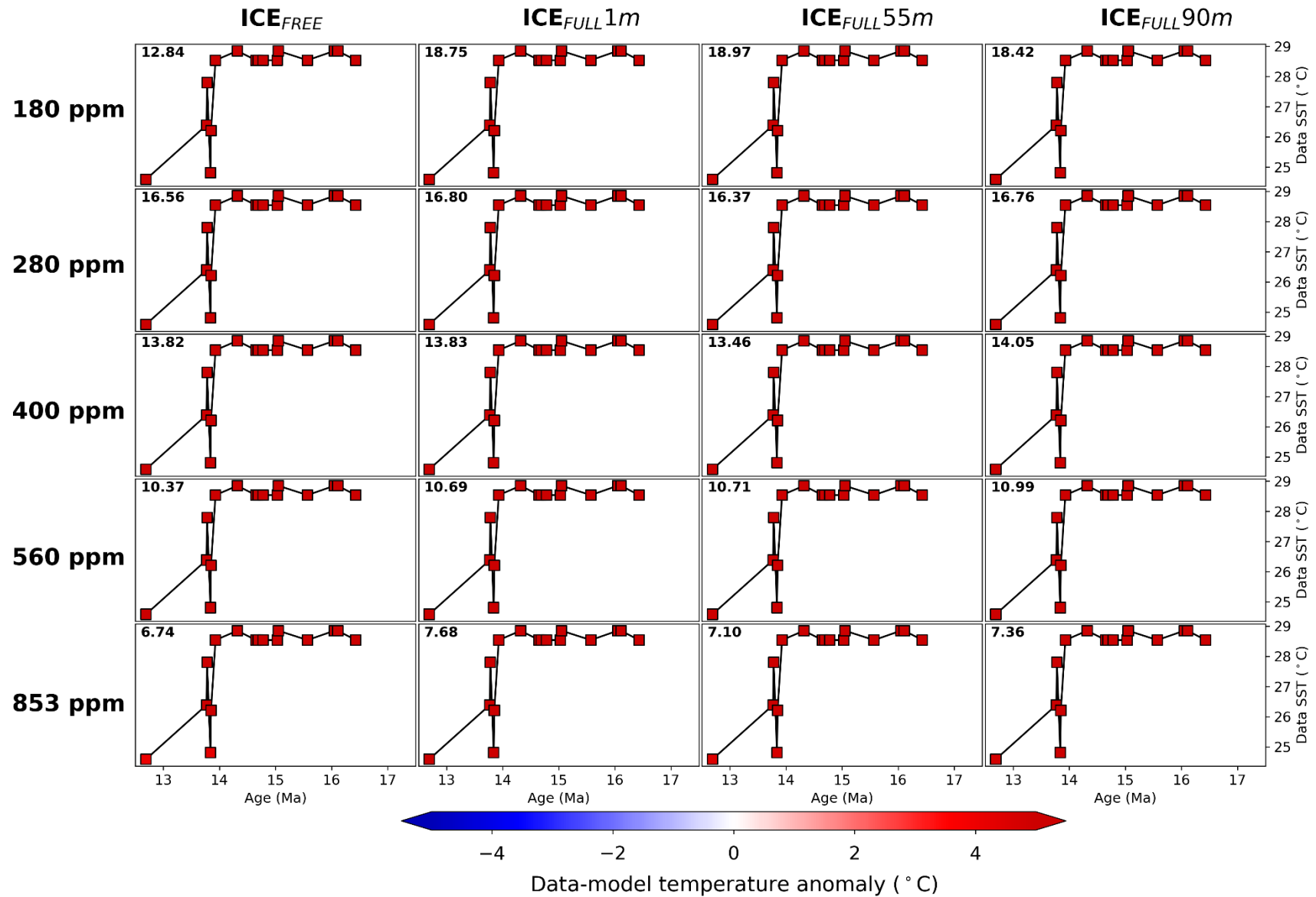
Supplementary Figure S13. Summer (DJF) total precipitation model-data comparison for greenhouse (14.5-16.75 Ma) data reconstructions given in Supplementary Table S9. Legend information as in Supplementary Figure S2.



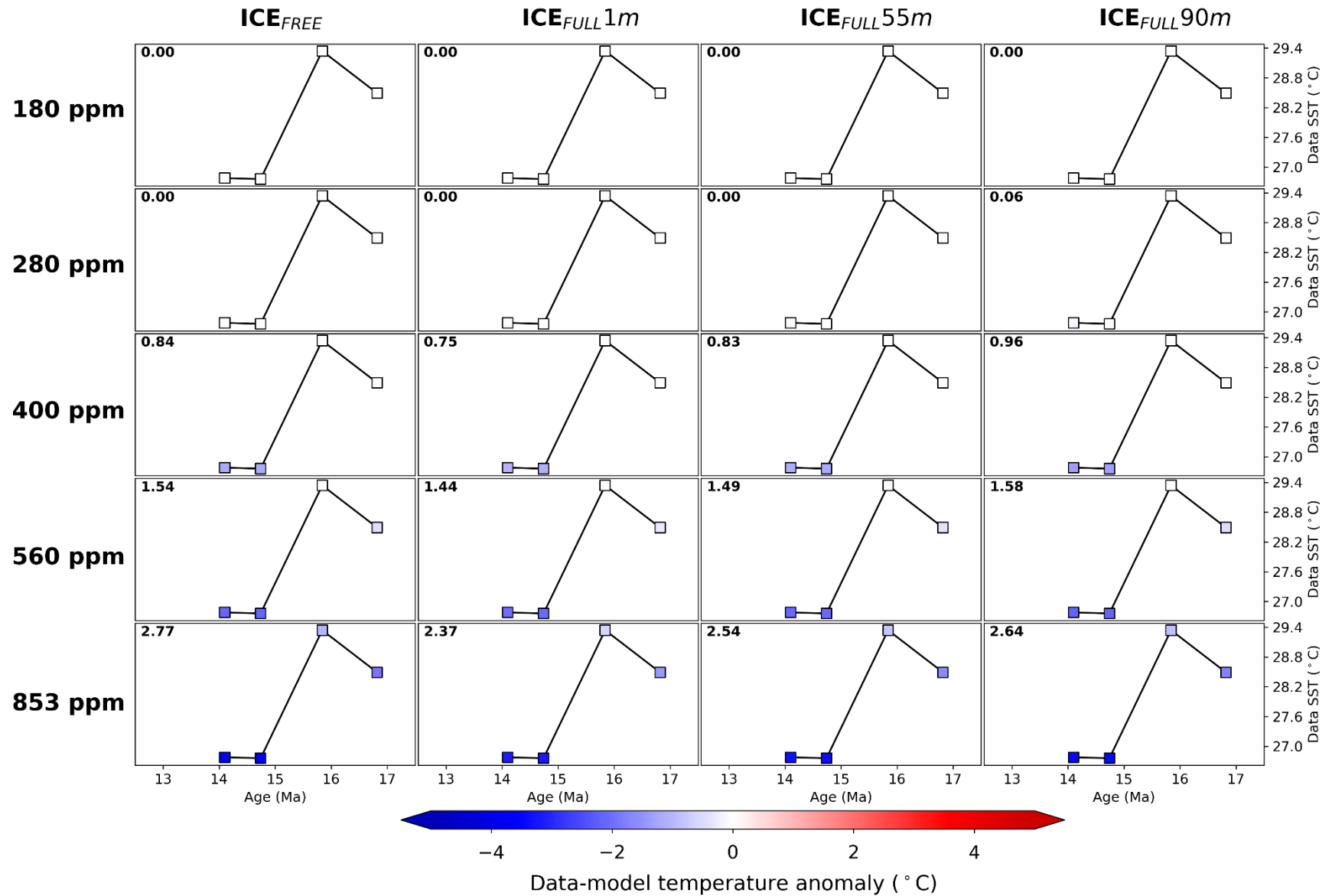
Supplementary Figure S14. Summer (DJF) mean precipitation model-data comparison for middle Miocene data reconstructions for Site AND-2A in the Ross Sea. Data from Feakins et al., 2012¹⁴ as given in Supplementary Table S9. Legend information as in Supplementary Figure S2.



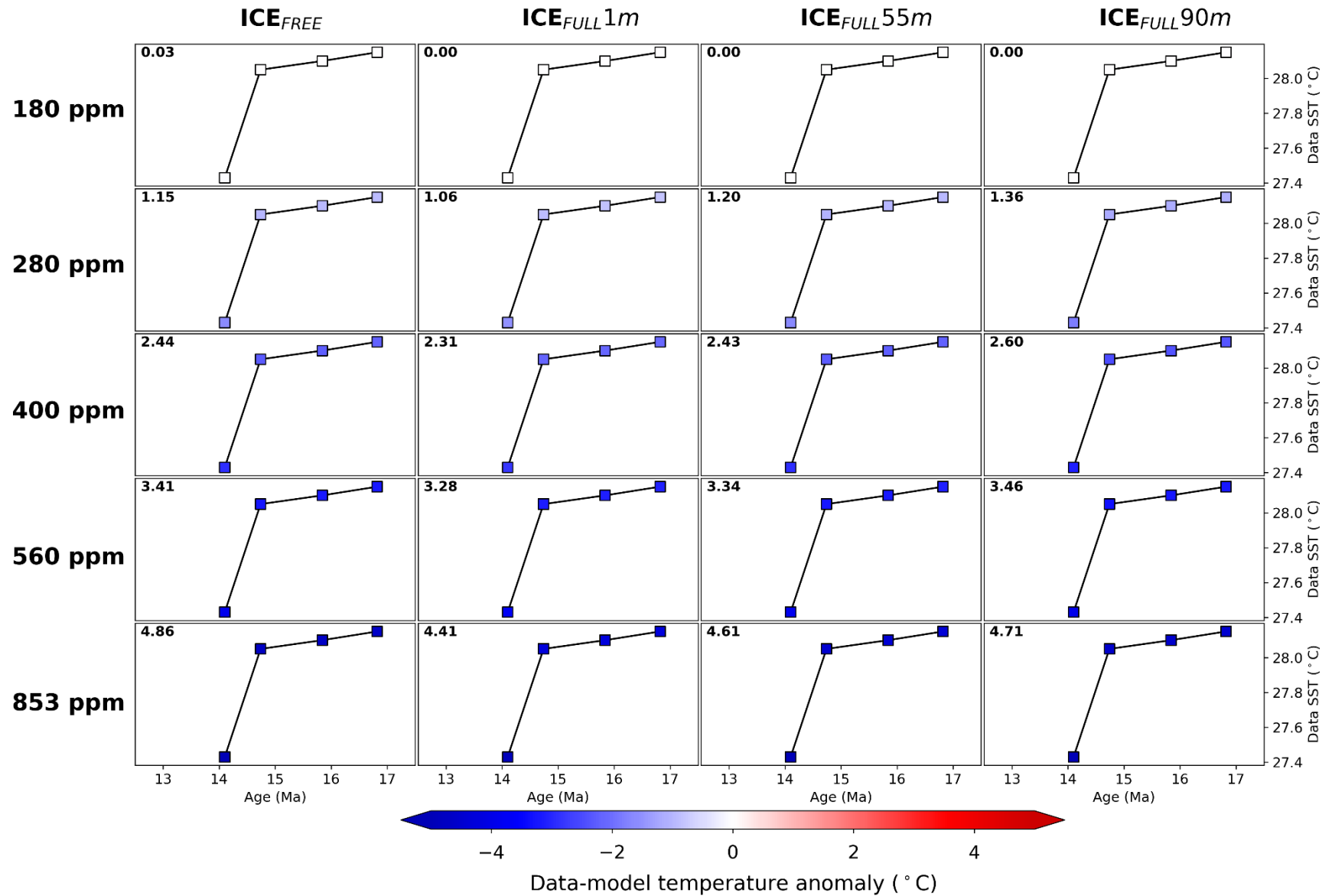
Supplementary Figure S15. Annual mean sea surface temperature model-data comparison for Site 608 in the North Atlantic (TEX₈₆). Data from Super et al., 2018¹⁵ as given in Supplementary Table S10. Legend information as in Supplementary Figure S2.



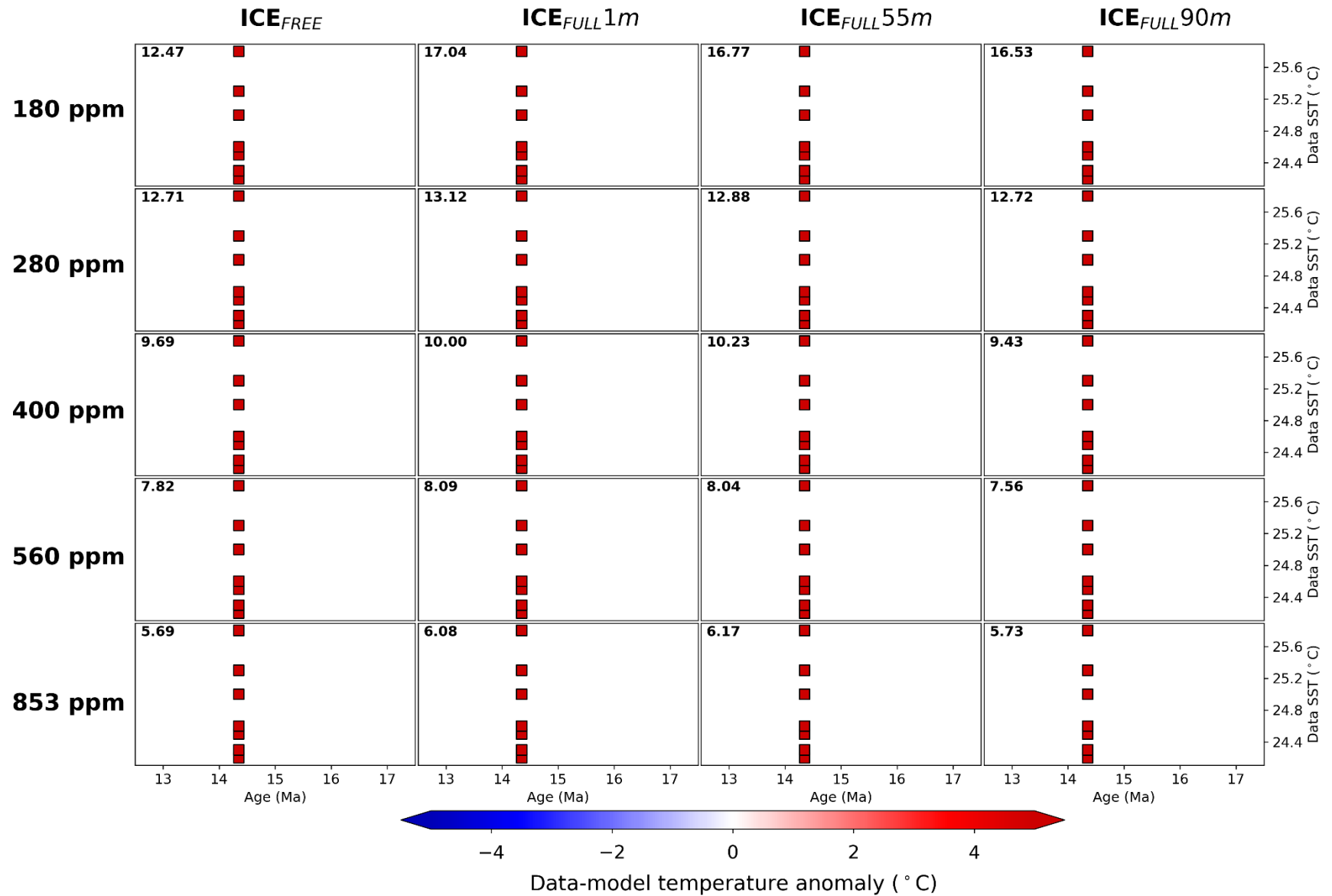
Supplementary Figure S16. Annual mean sea surface temperature model-data comparison for Site 608 in the North Atlantic (UK₃₇). Data from Super et al., 2018¹⁵ as given in Supplementary Table S10. Legend information as in Supplementary Figure S2



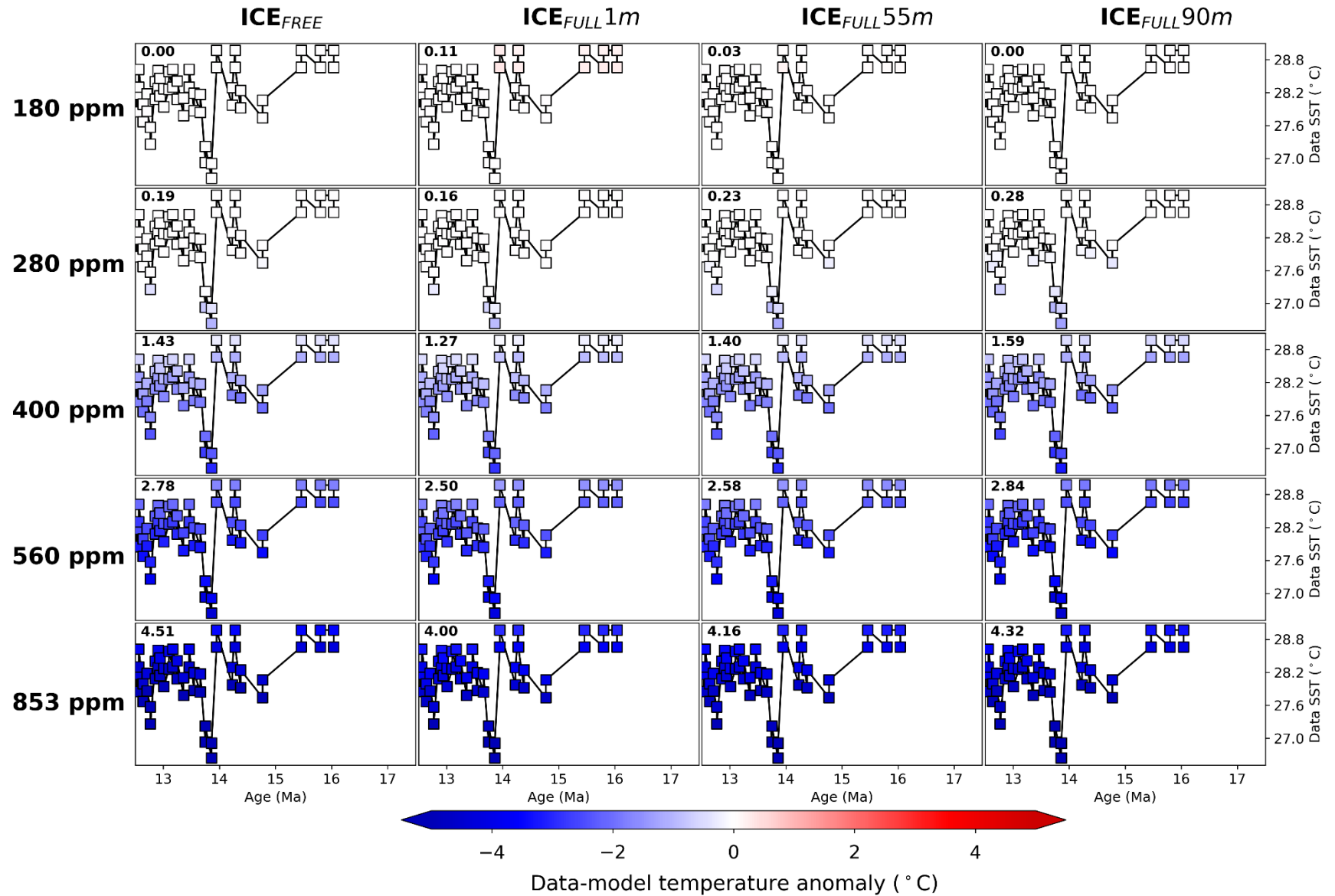
Supplementary Figure S17. Annual mean sea surface temperature model-data comparison for Site 925 in the Tropical Atlantic (TEX₈₆). Data from Zhang et al. 2013¹⁶ as given in Supplementary Table S10. Legend information as in Supplementary Figure S2.



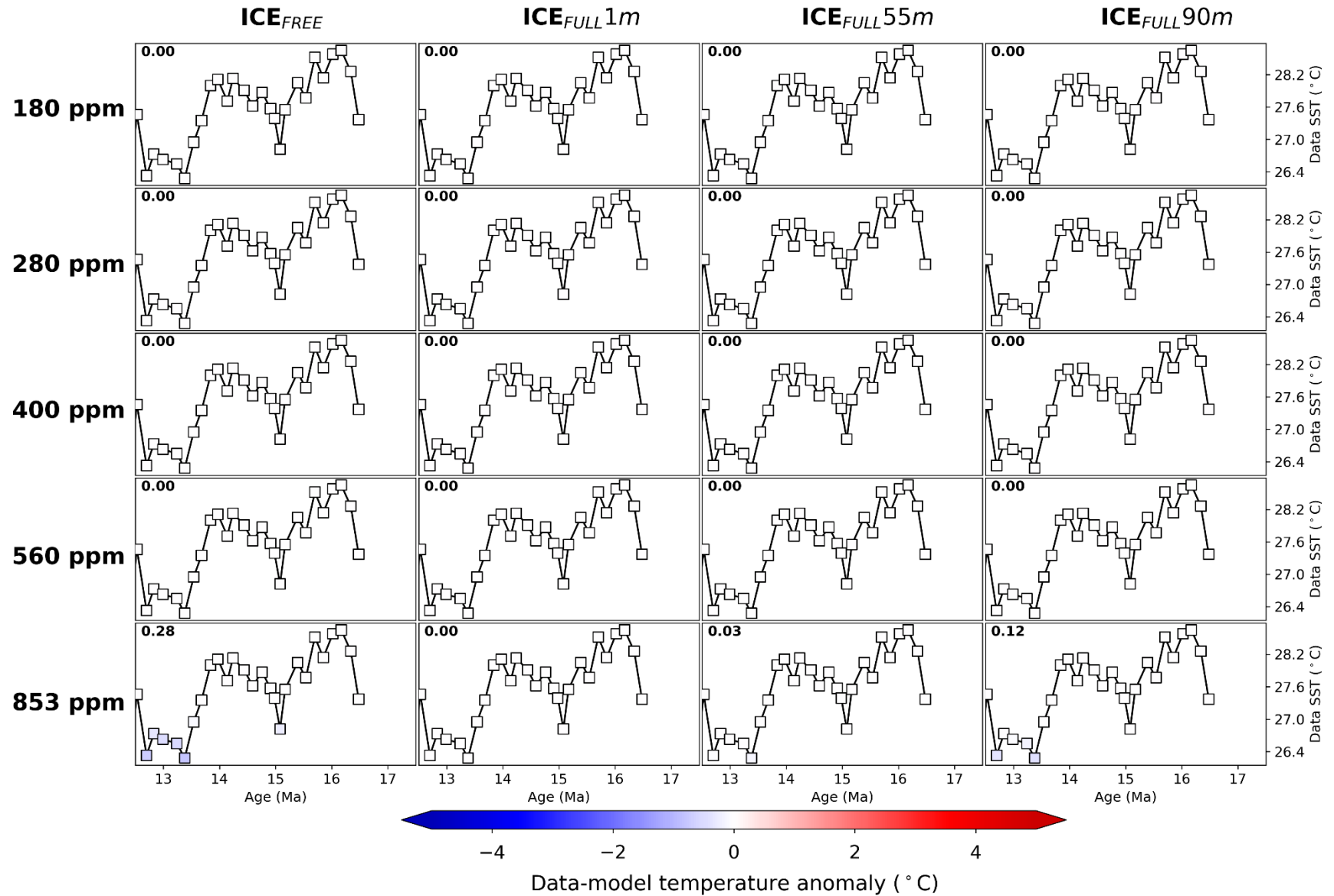
Supplementary Figure S18. Annual mean sea surface temperature model-data comparison for Site 925 in the Tropical Atlantic (UK'37). Data from Zhang et al. 2013¹⁶ as given in Supplementary Table S10. Legend information as in Supplementary Figure S2



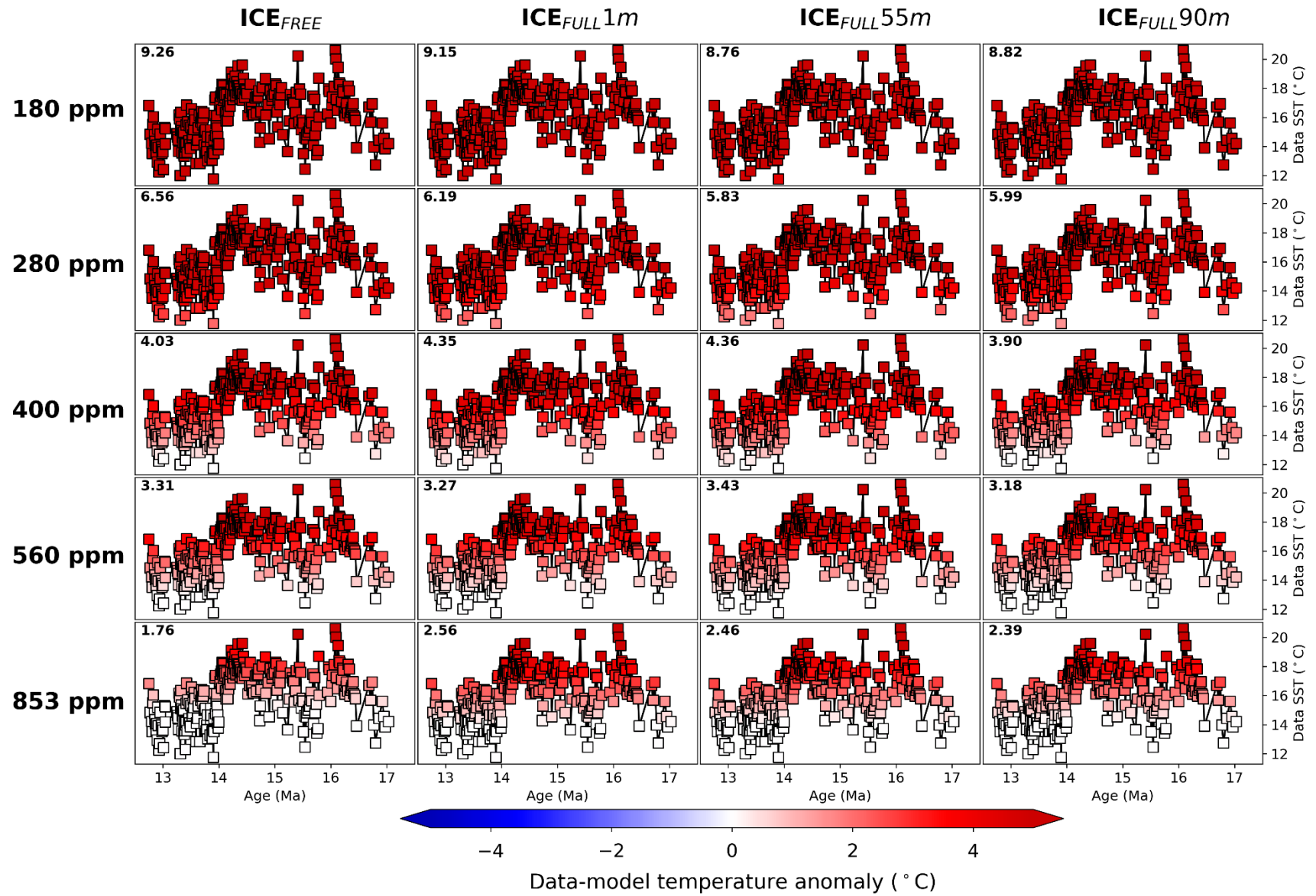
Supplementary Figure S19. Annual mean sea surface temperature model-data comparison for Site LOM-1 in the Mediterranean (Mg/Ca). Data from Scheiner et al. 2018¹⁷ as given in Supplementary Table S10. Legend information as in Supplementary Figure S2.



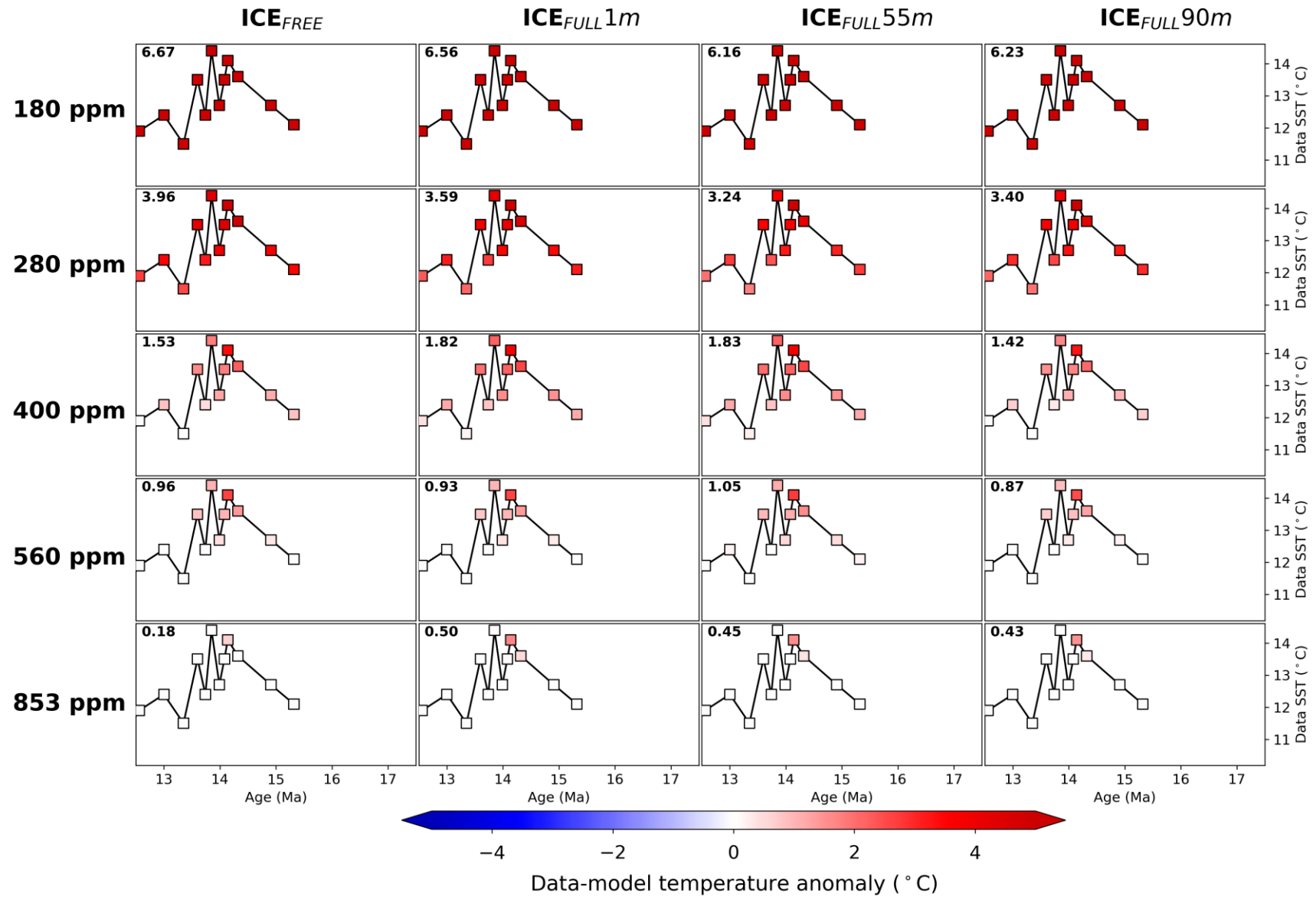
Supplementary Figure S20. Annual mean sea surface temperature model-data comparison for Site U1338 in the Tropical Pacific (UK²₃₇). Data from Rousselle et al., 2013¹⁸ as given in Supplementary Table S10. Legend information as in Supplementary Figure S2.



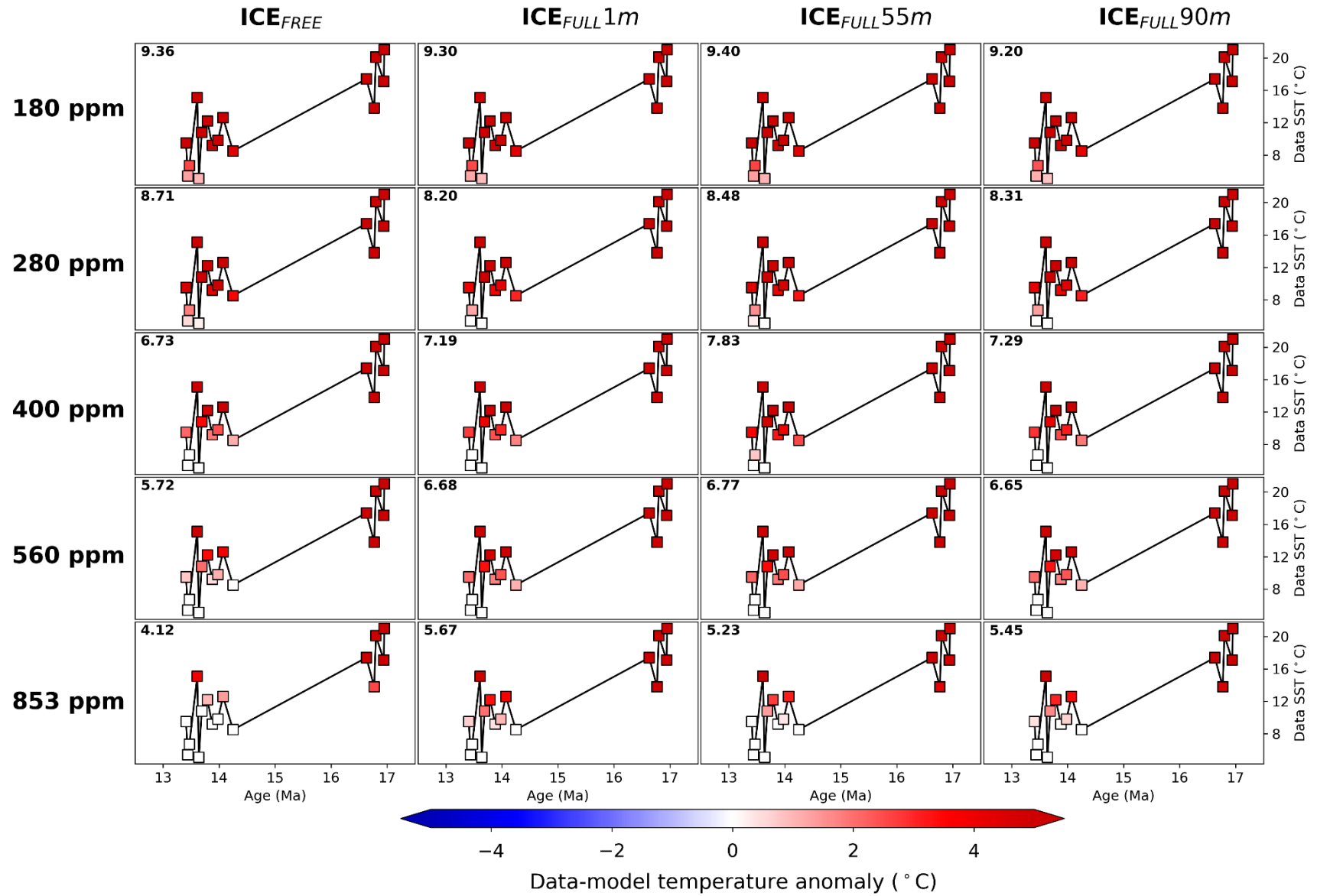
Supplementary Figure S21. Annual mean sea surface temperature model-data comparison for Site 806 in the Tropical Pacific (Mg/Ca). Data from Sosdian and Lear, submitted as given in Supplementary Table S10. Legend information as in Supplementary Figure S2.



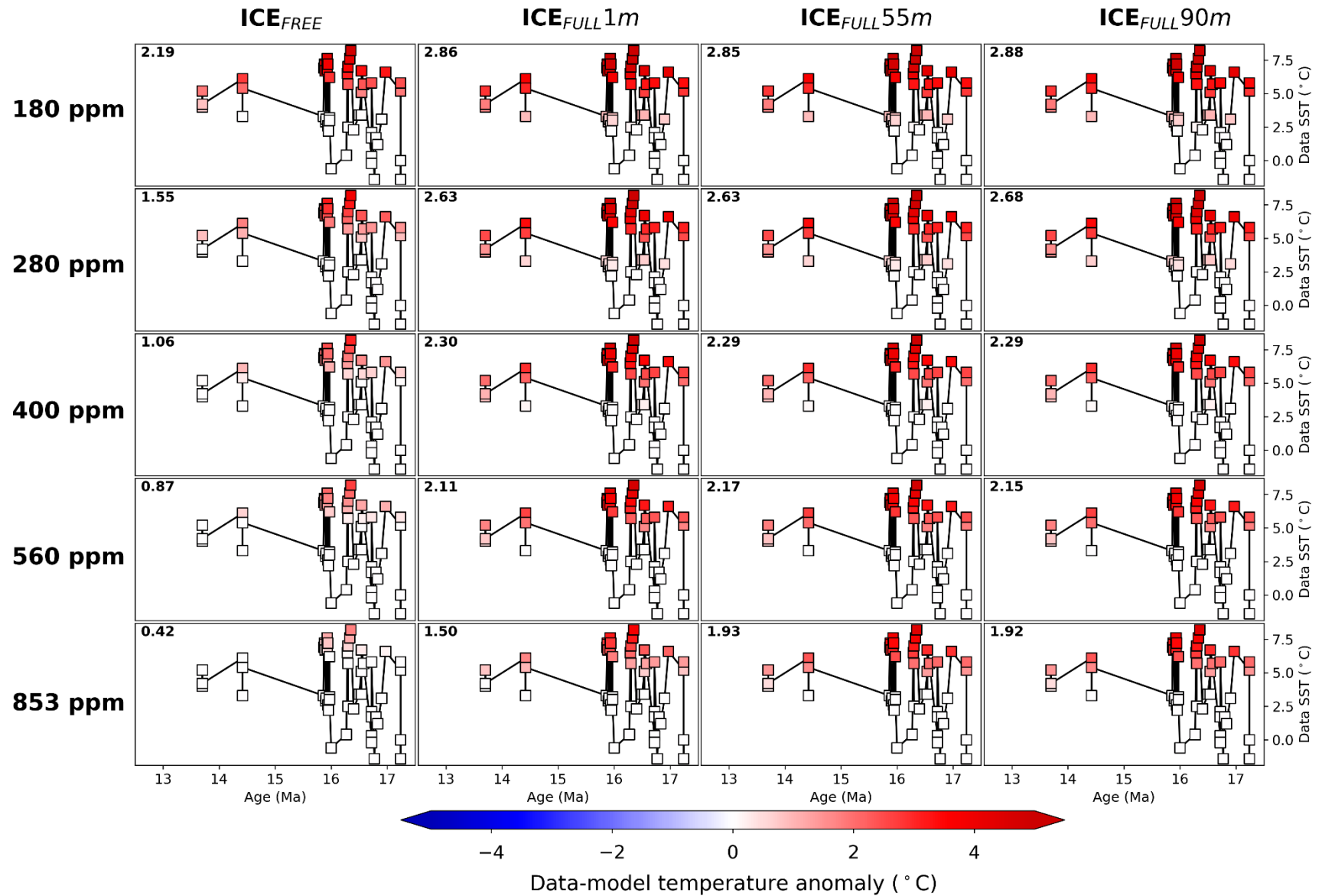
Supplementary Figure S22. Annual mean sea surface temperature model-data comparison for Site 1171 in the Southern Ocean (Mg/Ca). Data from Shevenell et al., 2004¹⁹ as given in Supplementary Table S10. Legend information as in Supplementary Figure S2.



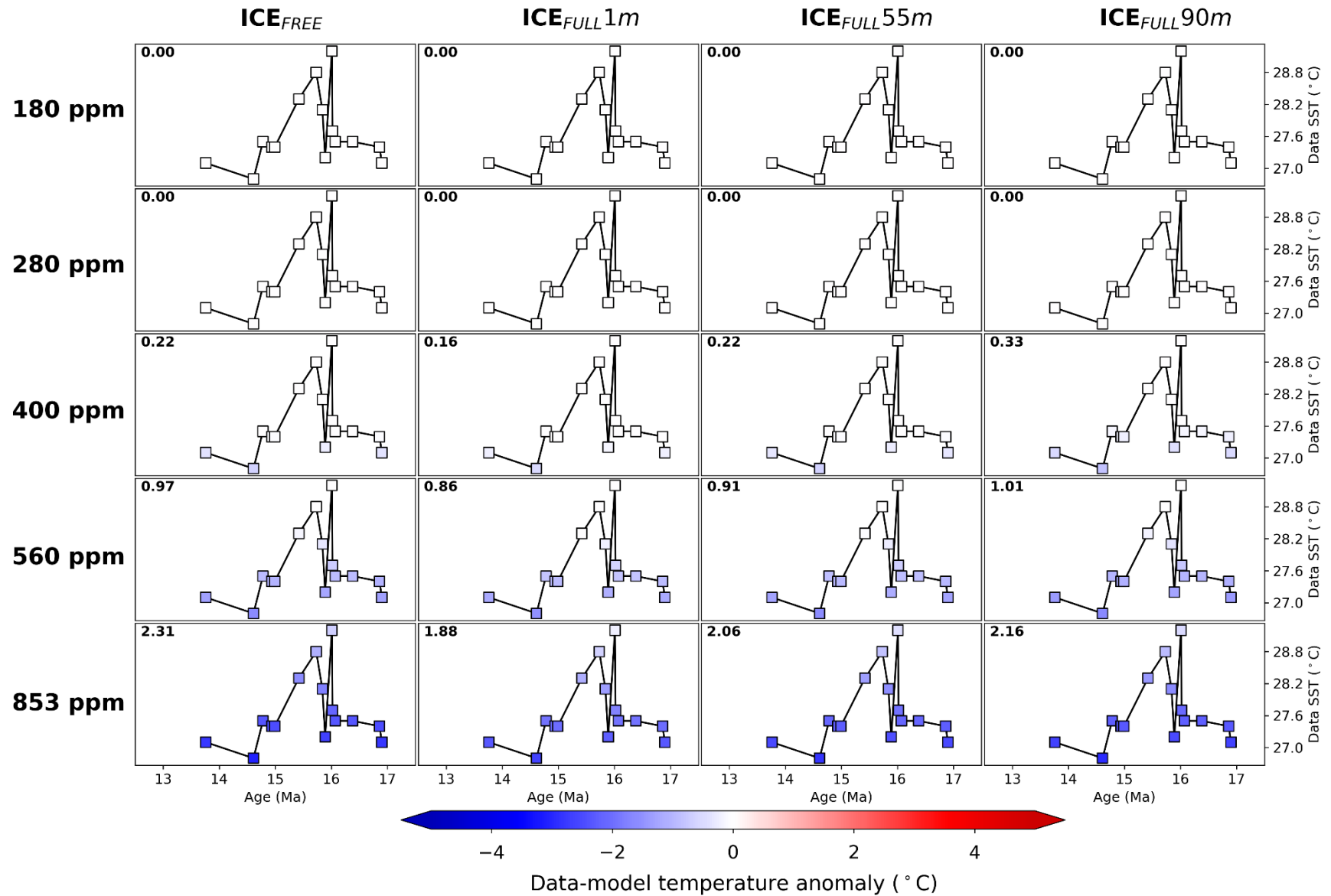
Supplementary Figure S23. Annual mean sea surface temperature model-data comparison for Site 1171 in the Southern Ocean ($\Delta 47$). Data from Leutert et al., 2020²⁰ as given in Supplementary Table S10. Legend information as in Supplementary Figure S2.



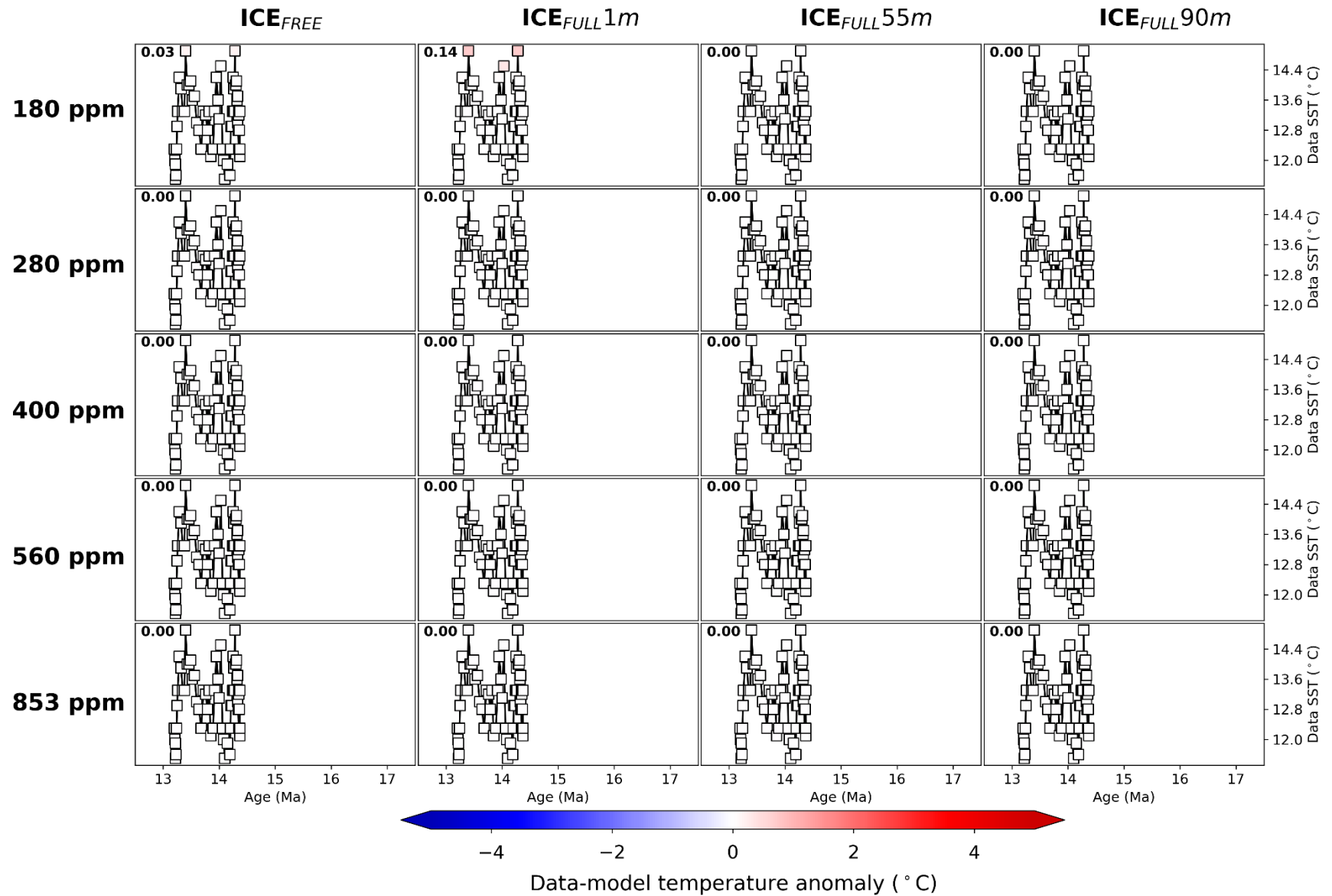
Supplementary Figure S24. Annual mean sea surface temperature model-data comparison for Site U1356 in the Southern Ocean (TEX^L₈₆). Data from Sangiorgi et al., 2018¹³ as given in Supplementary Table S10. Legend information as in Supplementary Figure S2.



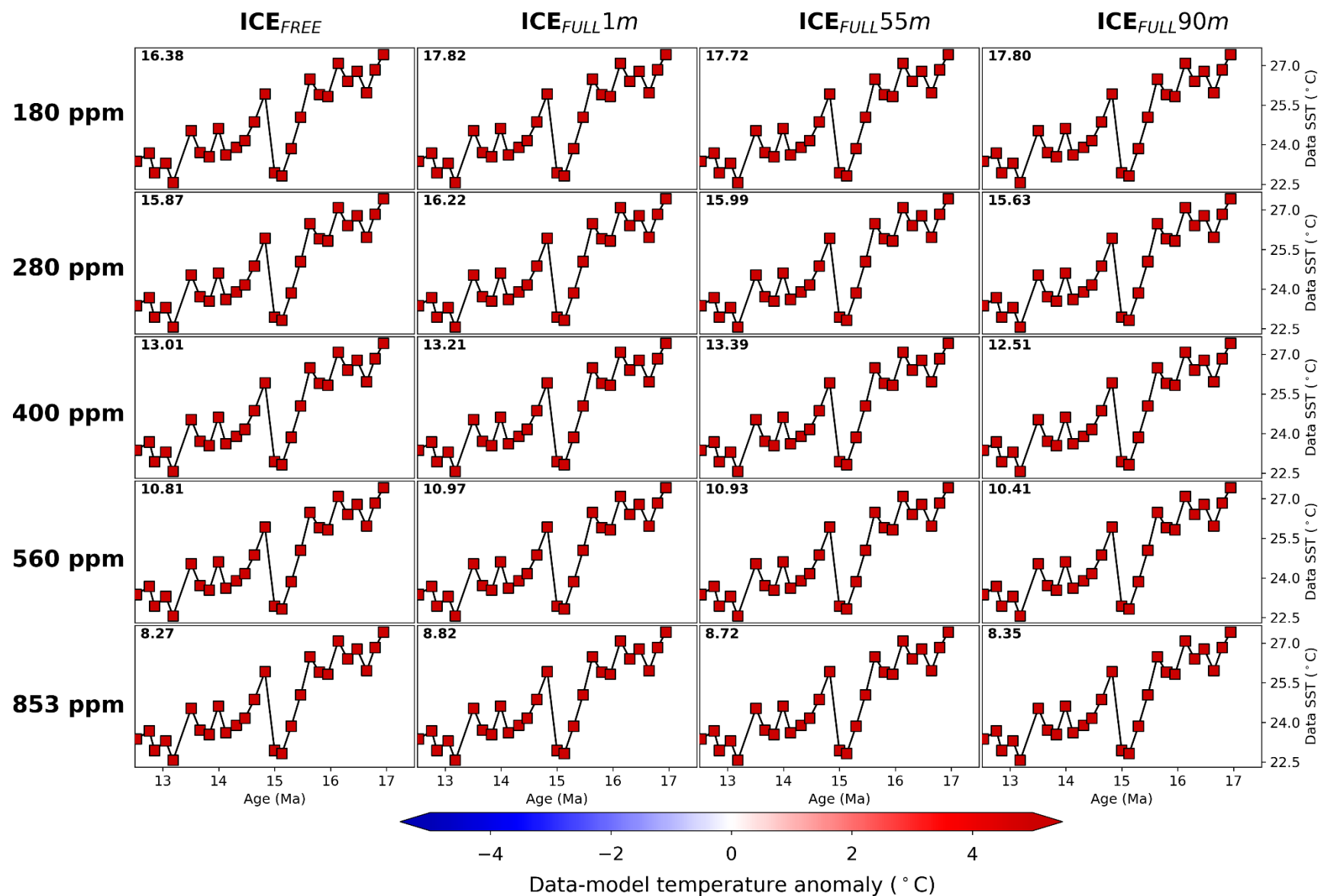
Supplementary Figure S25. Annual mean sea surface temperature model-data comparison for Site AND-2A in the Ross Sea (TEX^L₈₆). Data from Levy et al., 2016²¹ as given in Supplementary Table S10. Legend information as in Supplementary Figure S2.



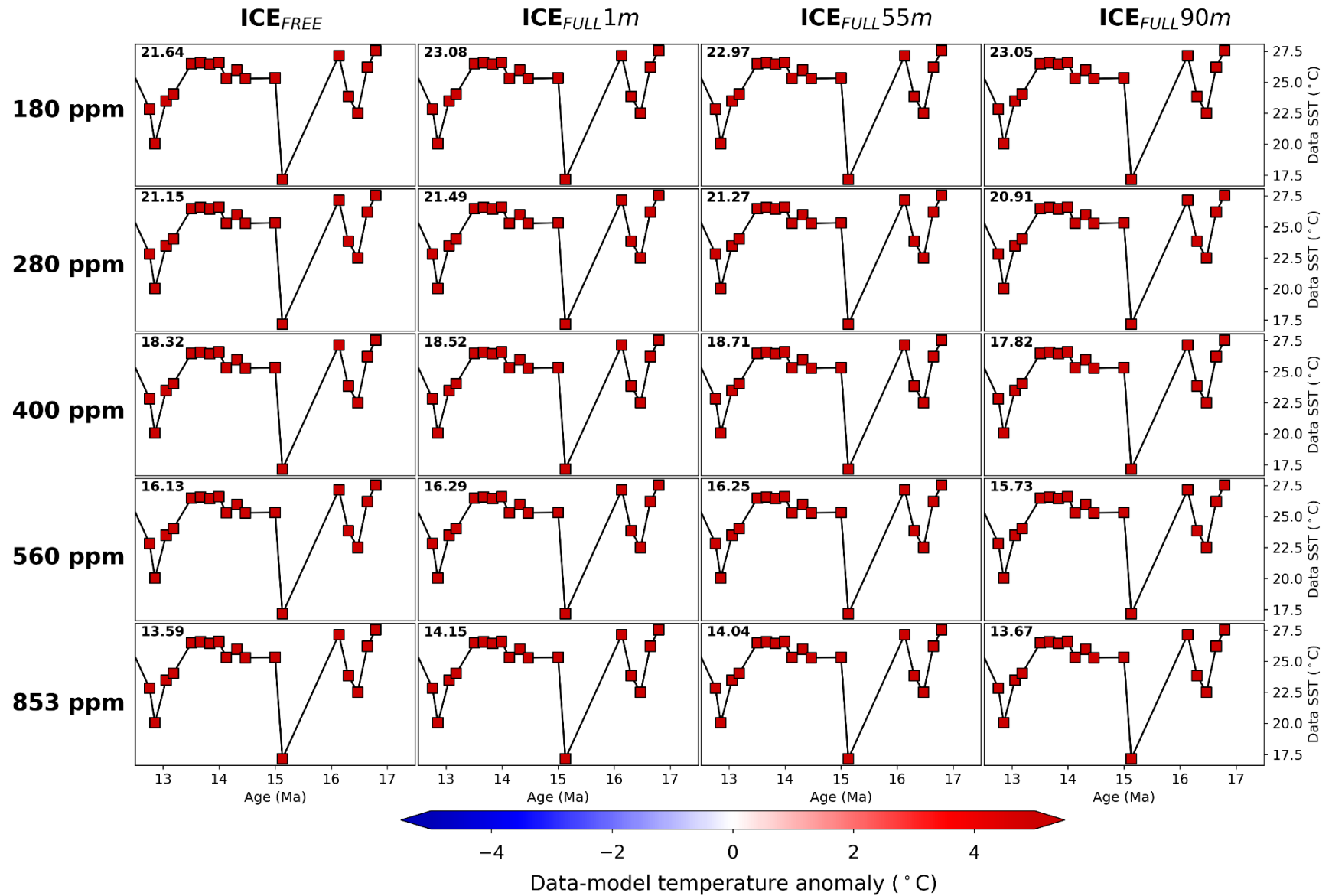
Supplementary Figure S26. Annual mean sea surface temperature model-data comparison for Site 926 in the Tropical Atlantic (Mg/Ca). Data from Sossian et al., 2018²² and Foster et al., 2012²³ as given in Supplementary Table S10. Legend information as in Supplementary Figure S2.



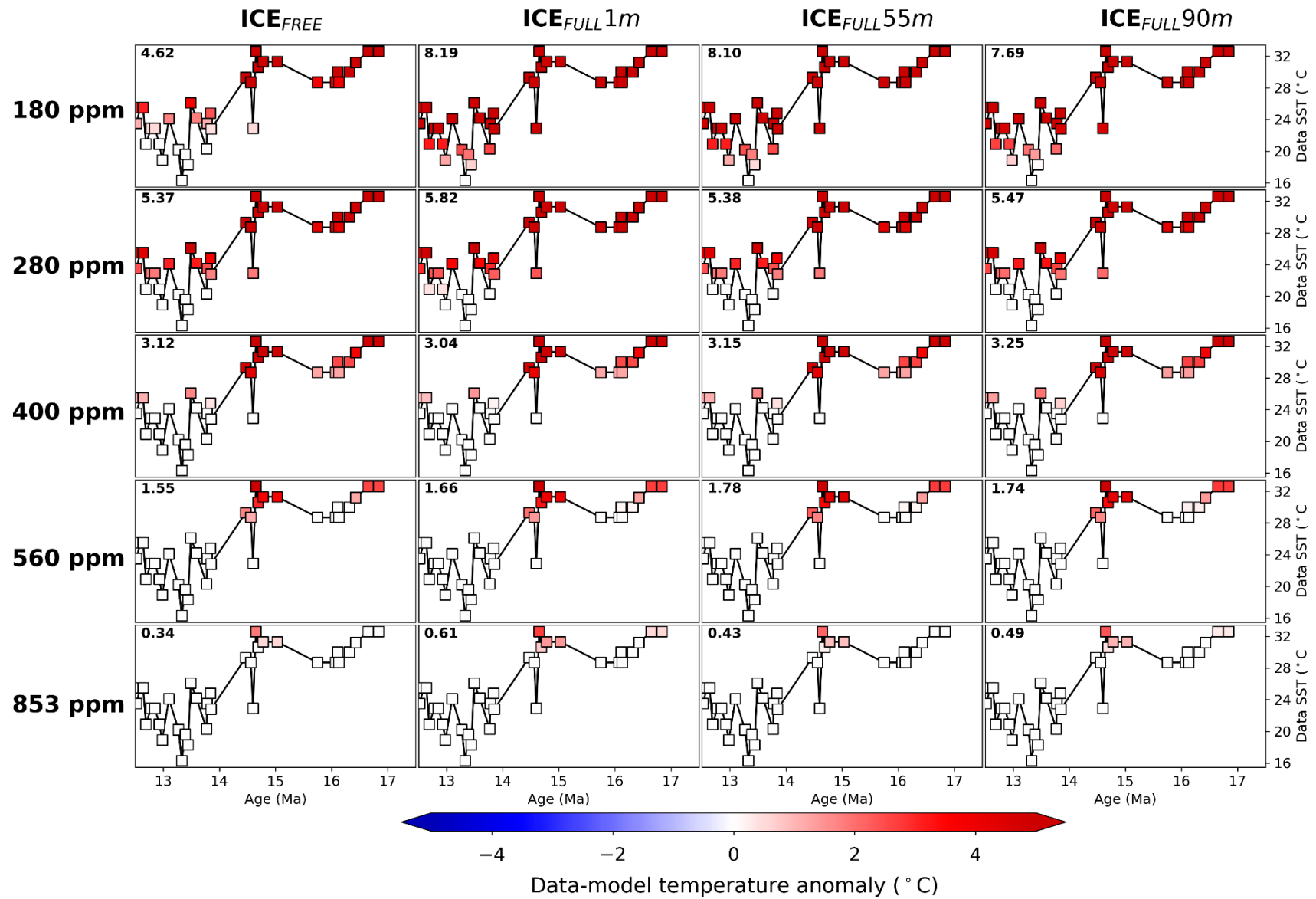
Supplementary Figure S27. Annual mean sea surface temperature model-data comparison for Site 1092 in the Southern Ocean (Mg/Ca). Data from Kuhnert et al., 2009²⁴ as given in Supplementary Table S10. Legend information as in Supplementary Figure S2.



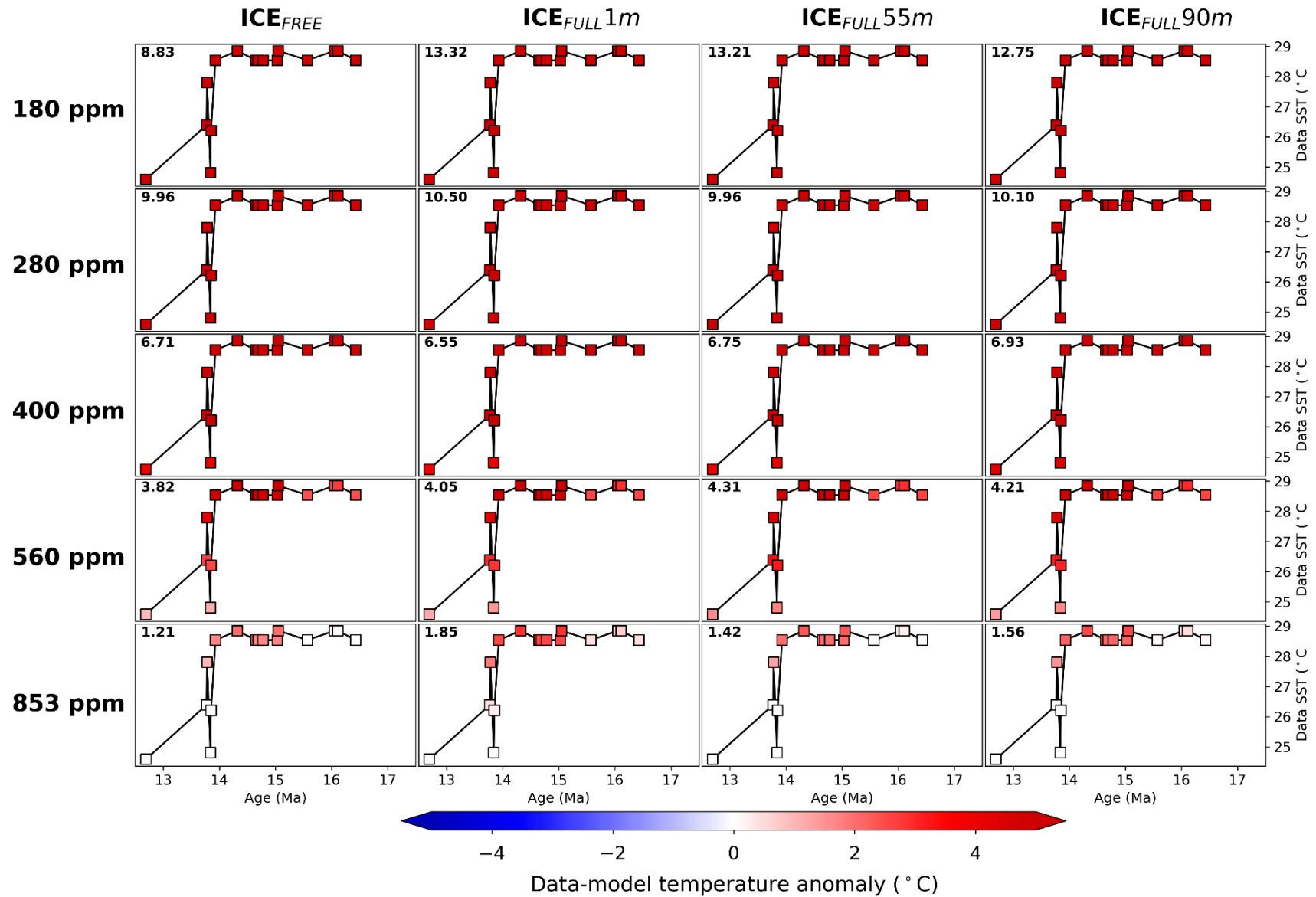
Supplementary Figure S28. Annual mean sea surface temperature model-data comparison for Site 982 in the North Atlantic (TEX₈₆). Data from Super et al., 2020²⁵ as given in Supplementary Table S10. Legend information as in Supplementary Figure S2.



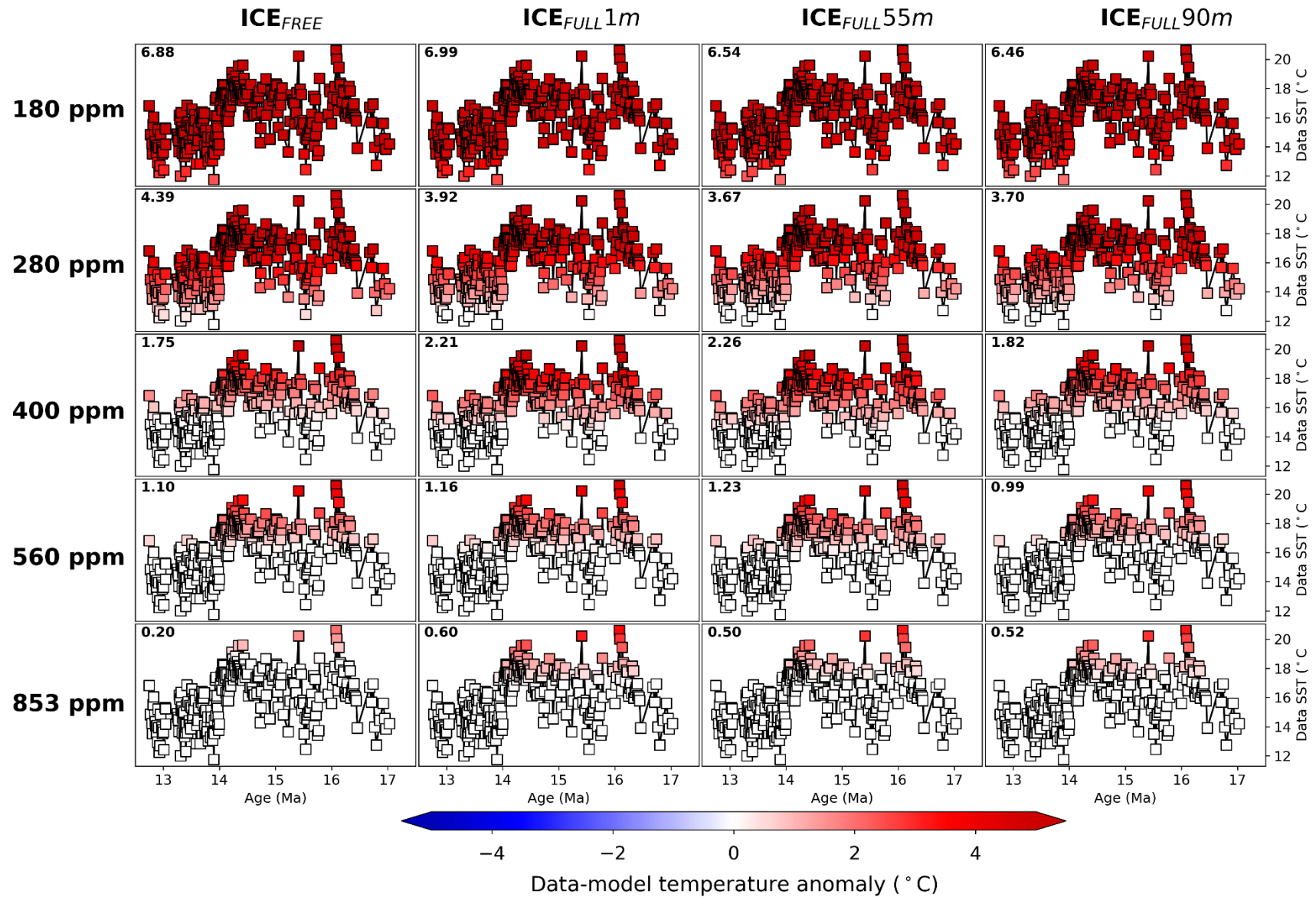
Supplementary Figure S29. Annual mean sea surface temperature model-data comparison for Site 982 in the North Atlantic (UK'37). Data from Super et al., 2020²⁵ as given in Supplementary Table S10. Legend information as in Supplementary Figure S2.



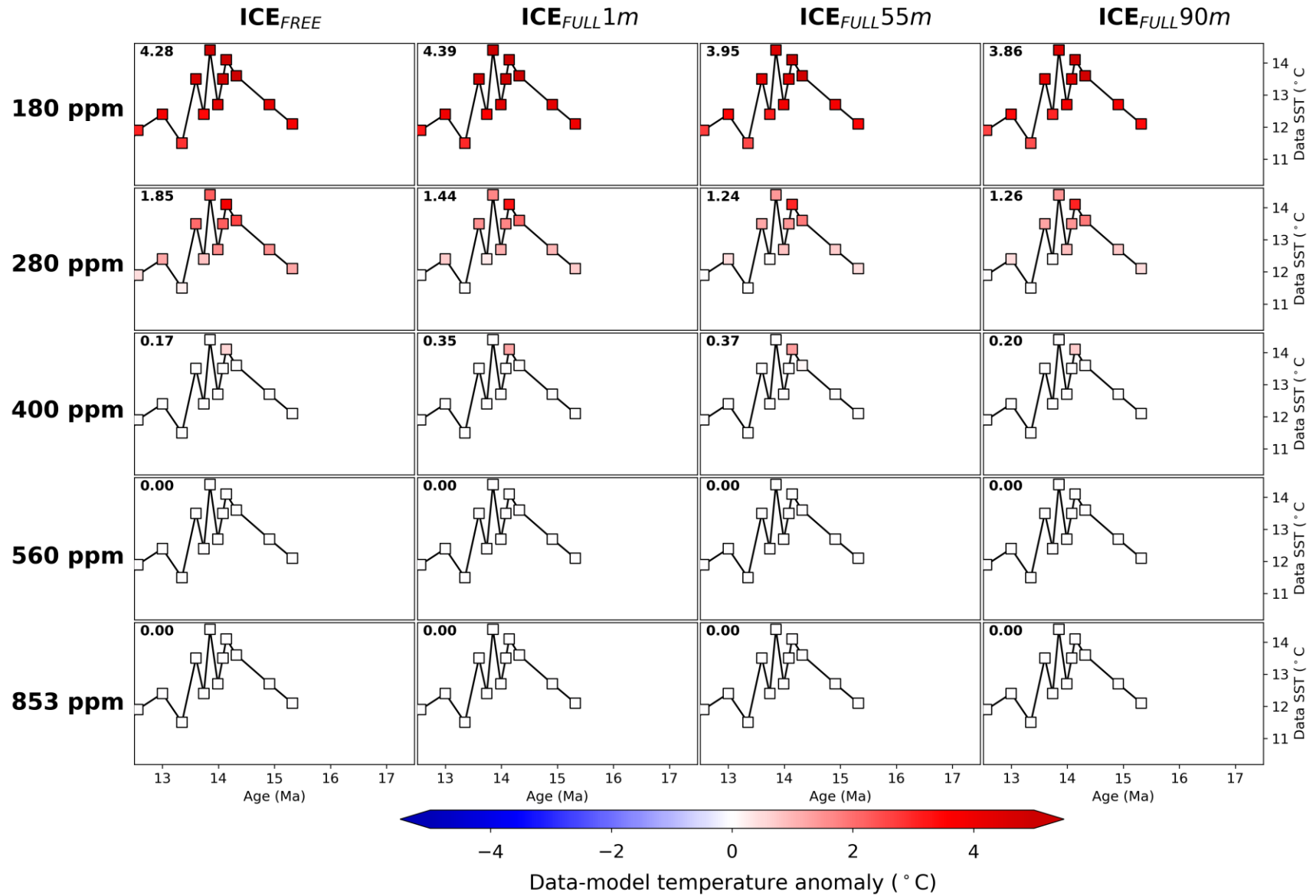
Supplementary Figure S30. Maximum sea surface temperature model-data comparison for Site 608 in the North Atlantic (TEX₈₆). Data from Super et al., 2018¹⁵ as given in Supplementary Table S10. Legend information as in Supplementary Figure S2.



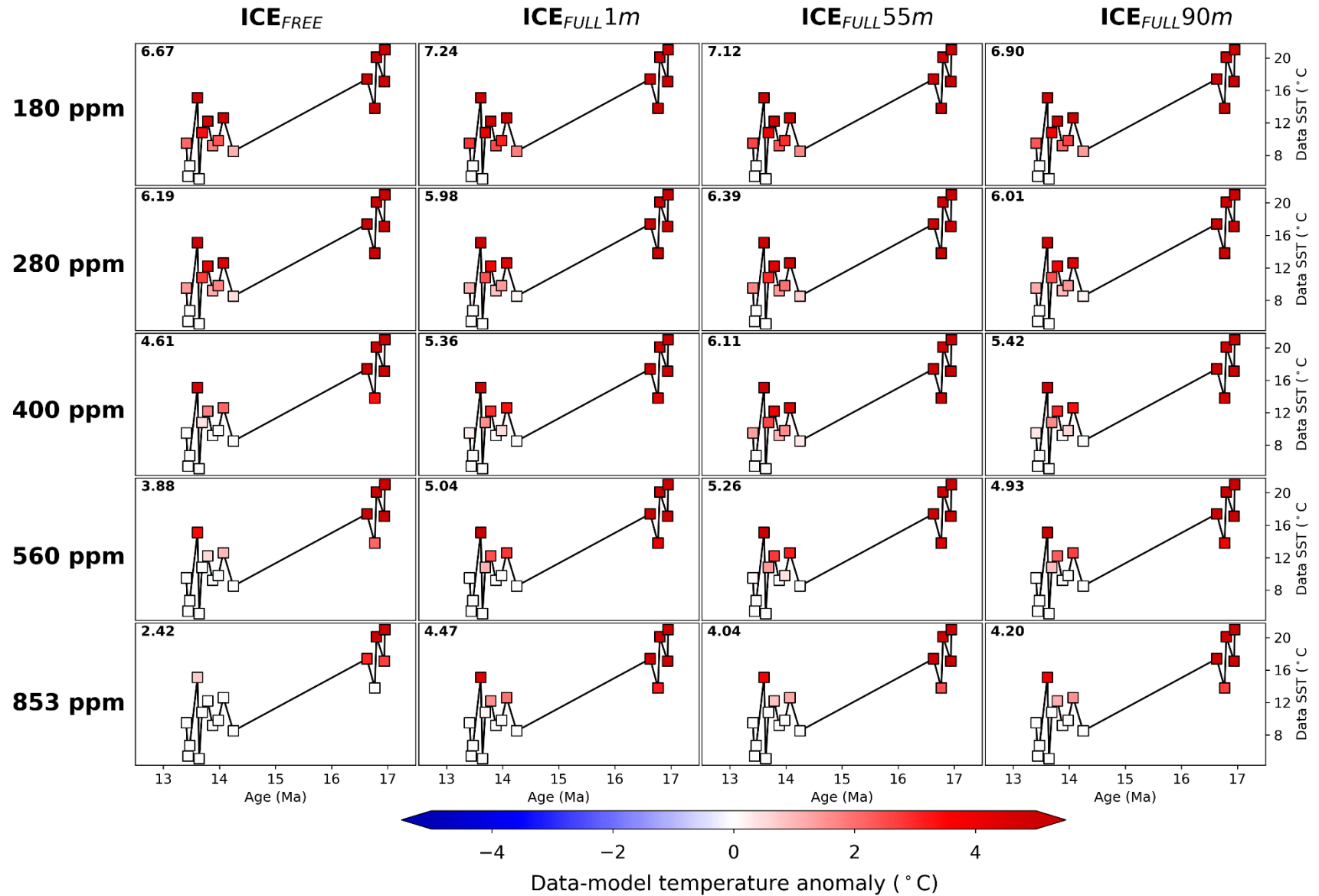
Supplementary Figure S31. Maximum sea surface temperature model-data comparison for Site 608 in the North Atlantic (UK^37). Data from Super et al., 2018¹⁵ as given in Supplementary Table S10. Legend information as in Supplementary Figure S2



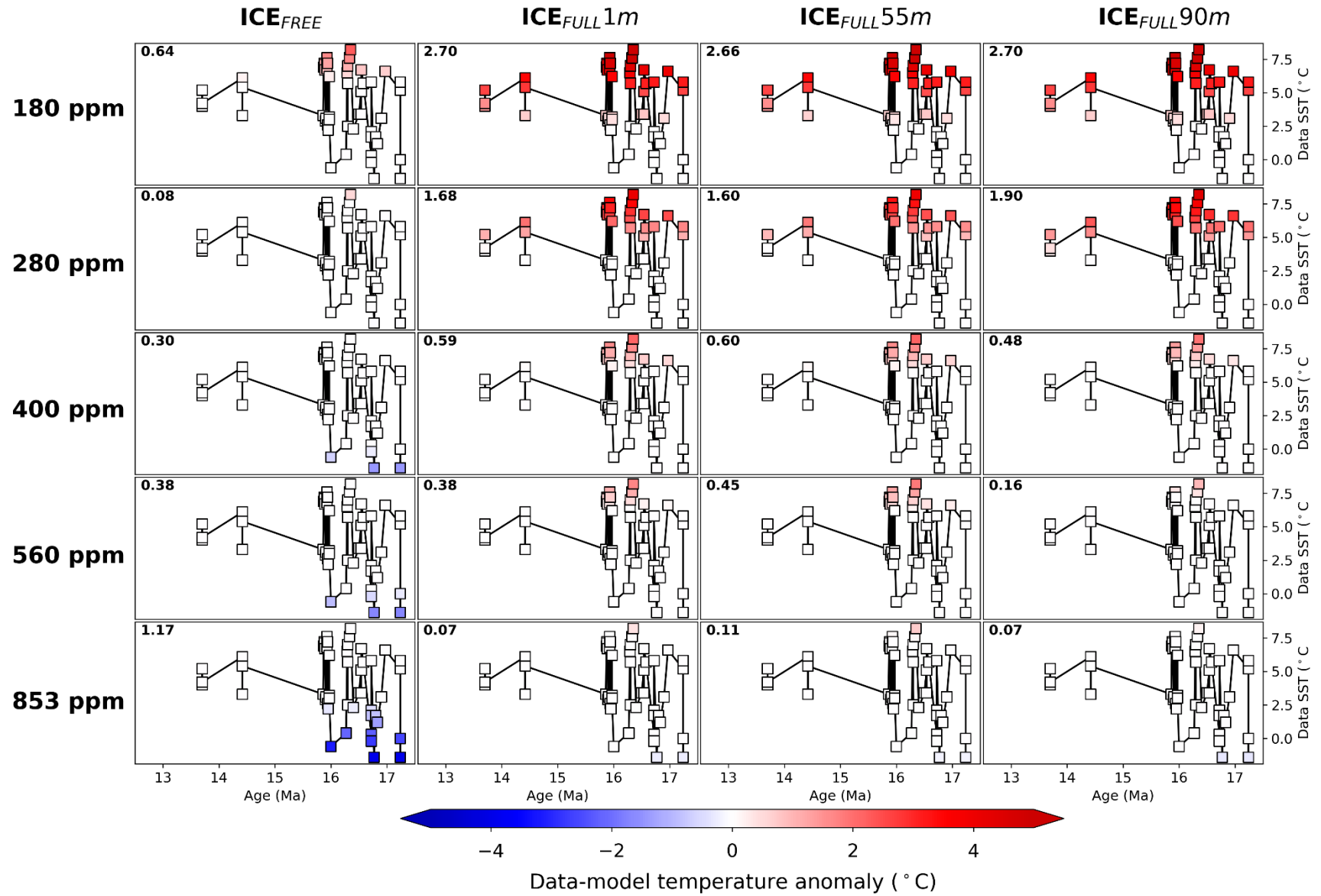
Supplementary Figure S32. Maximum sea surface temperature model-data comparison for Site 1171 in the Southern Ocean (Mg/Ca). Data from Shevenell et al., 2004¹⁹ as given in Supplementary Table S10. Legend information as in Supplementary Figure S2.



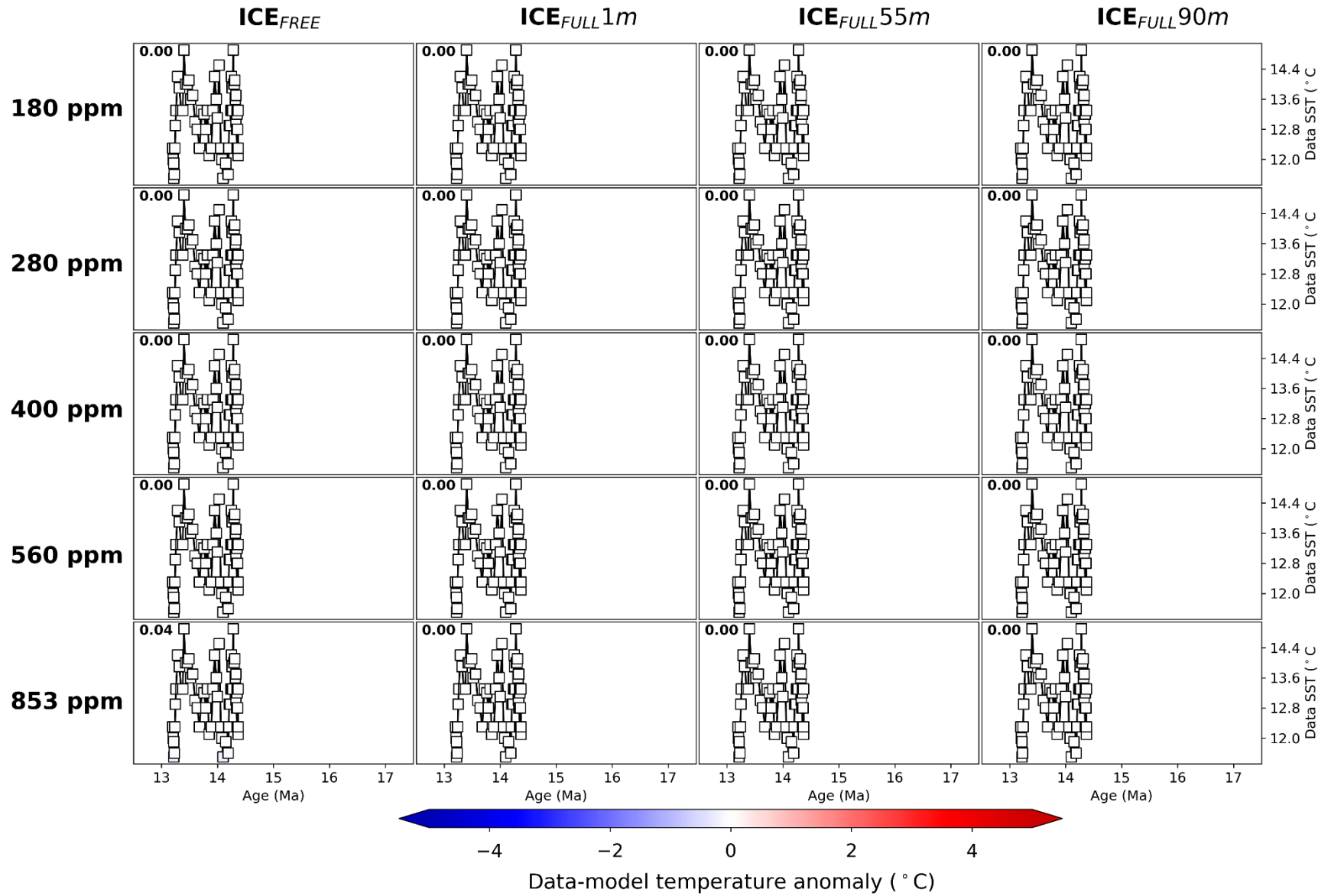
Supplementary Figure S33. Maximum sea surface temperature model-data comparison for Site 1171 in the Southern Ocean ($\Delta 47$). Data from Leutert et al., 2020²⁰ as given in Supplementary Table S10. Legend information as in Supplementary Figure S2.



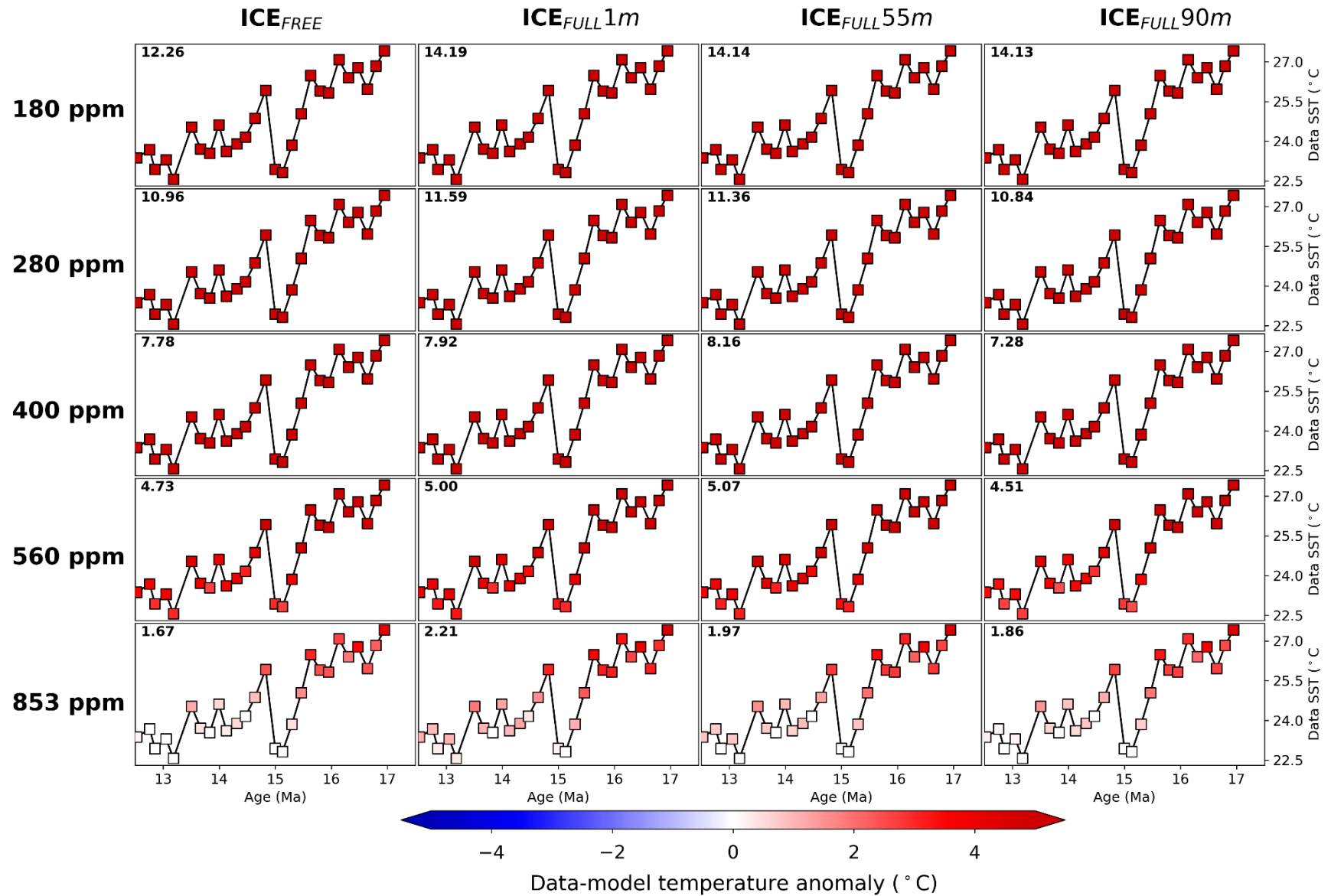
Supplementary Figure S34. Maximum sea surface temperature model-data comparison for Site U1356 in the Southern Ocean (TEX^L₈₆). Data from Sangiorgi et al., 2018¹³ as given in Supplementary Table S10. Legend information as in Supplementary Figure S2.



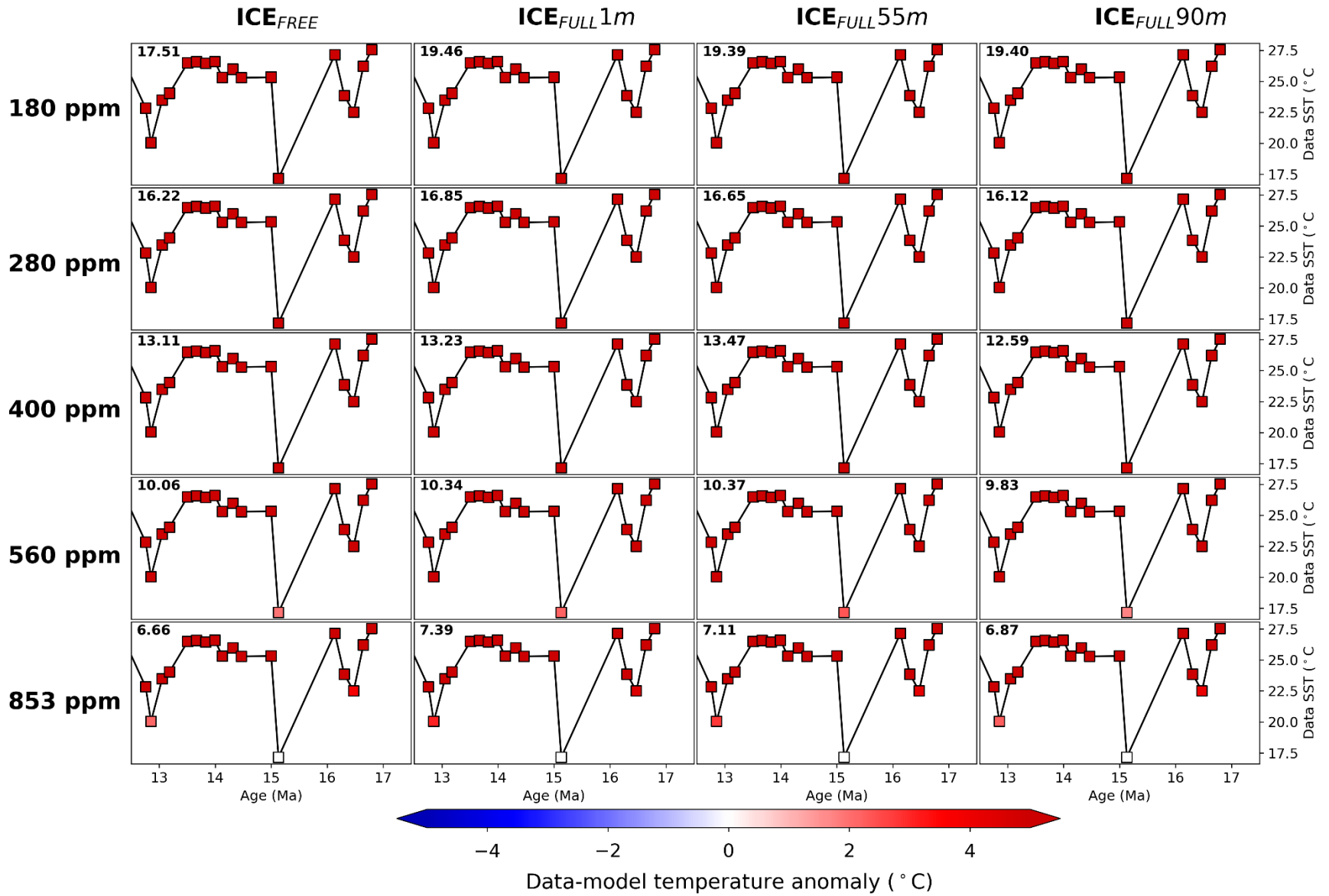
Supplementary Figure S35. Maximum sea surface temperature model-data comparison for Site AND-2A in the Southern Ocean (TEX_{L86}). Data from Levy et al., 2016²¹ as given in Supplementary Table S10. Legend information as in Supplementary Figure S2.



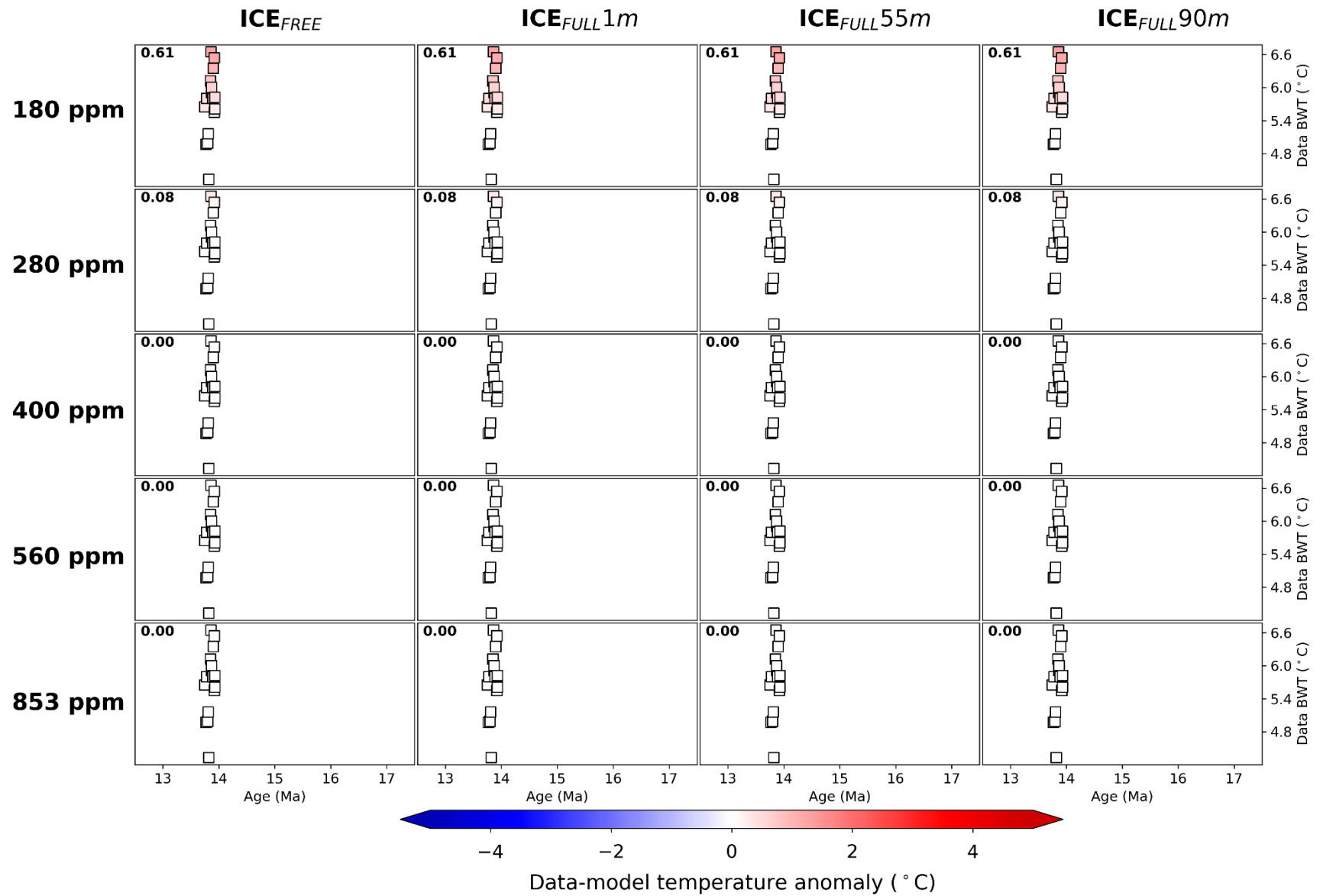
Supplementary Figure S36. Maximum sea surface temperature model-data comparison for Site 1092 in the Southern Ocean (Mg/Ca). Data from Kuhnert et al., 2009²⁴ as given in Supplementary Table S10. Legend information as in Supplementary Figure S2.



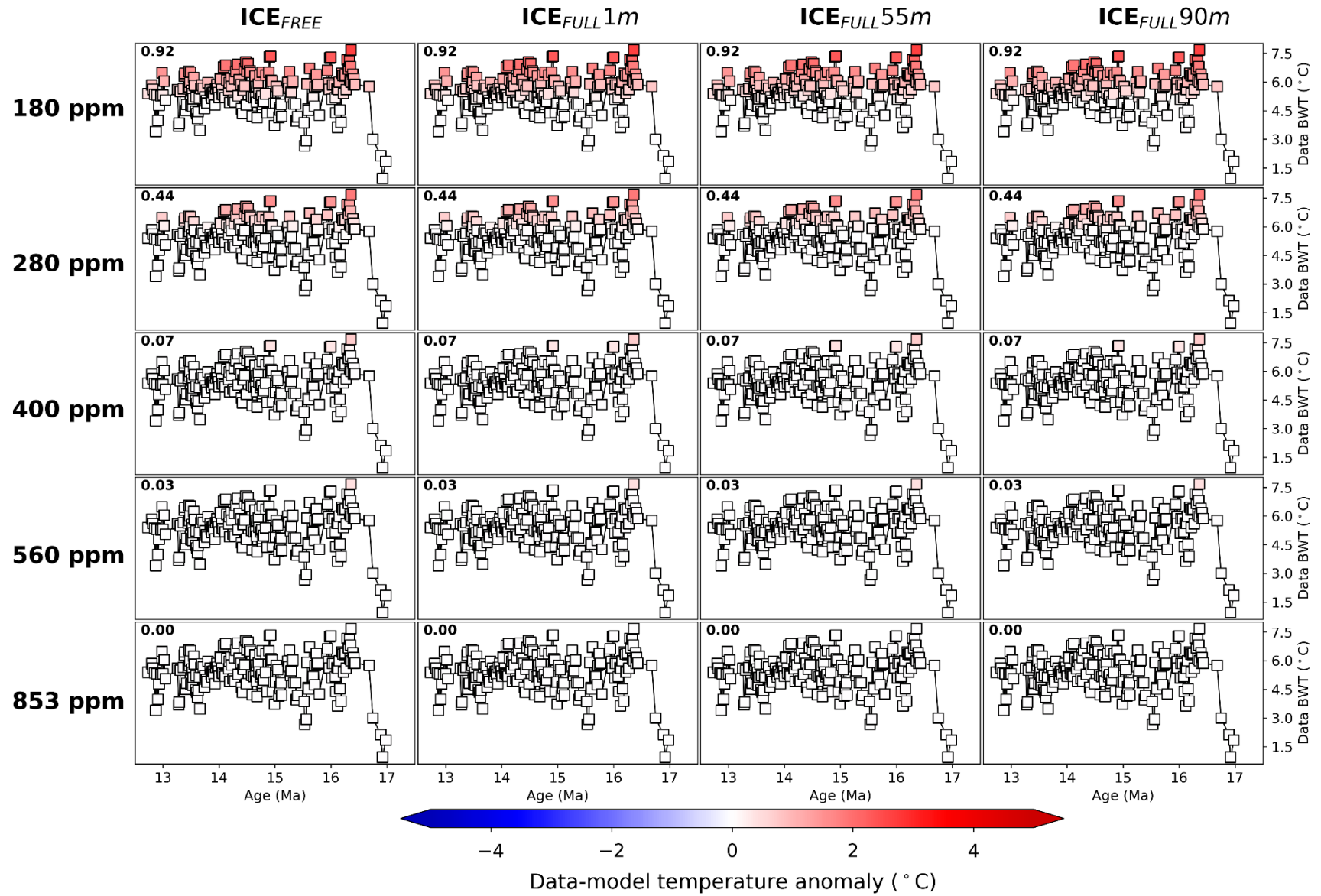
Supplementary Figure S37. Maximum sea surface temperature model-data comparison for Site 982 in the North Atlantic (TEX₈₆). Data from Super et al., 2020²⁵ as given in Supplementary Table S10. Legend information as in Supplementary Figure S2.



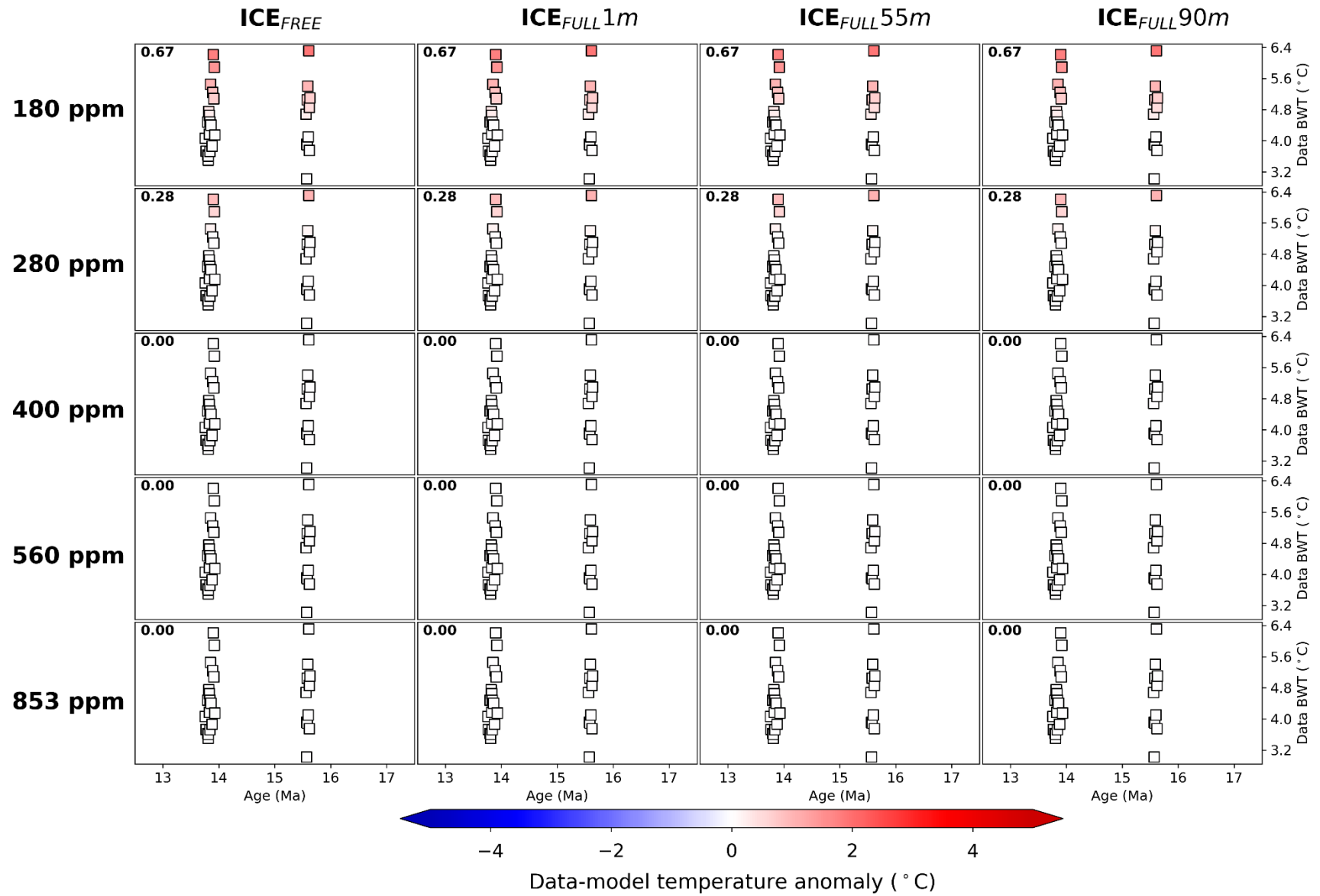
Supplementary Figure S38. Maximum sea surface temperature model-data comparison for Site 982 in the North Atlantic (U^K_{37}). Data from Super et al., 2020²⁵ as given in Supplementary Table S10. Legend information as in Supplementary Figure S2.



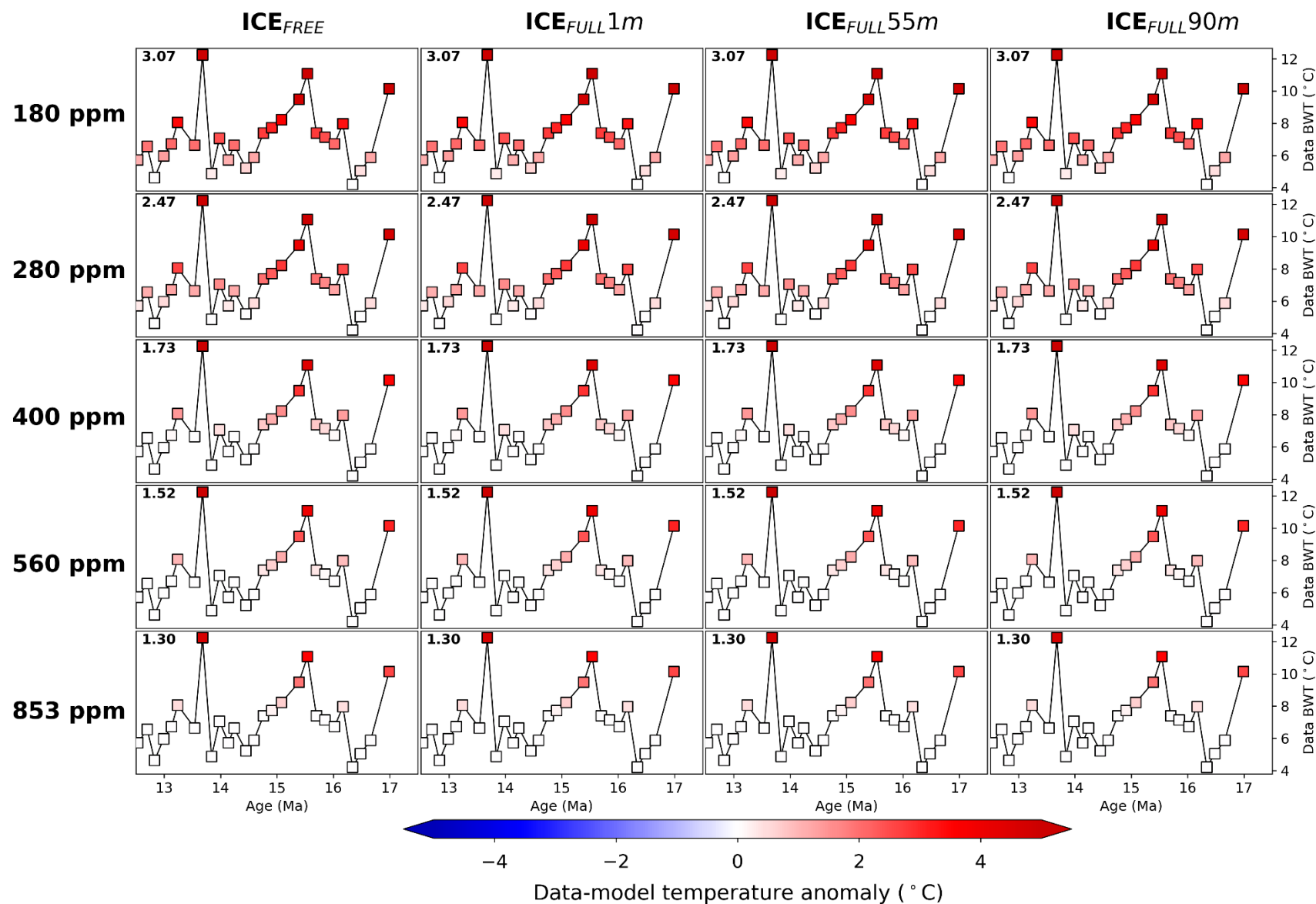
Supplementary Figure S39. Annual mean deep water temperature model-data comparison for Site 1146 in the South China Sea (Mg/Ca). Data from Kochhann et al., 2017²⁶ as given in Supplementary Table S11. Legend information as in Supplementary Figure S2.



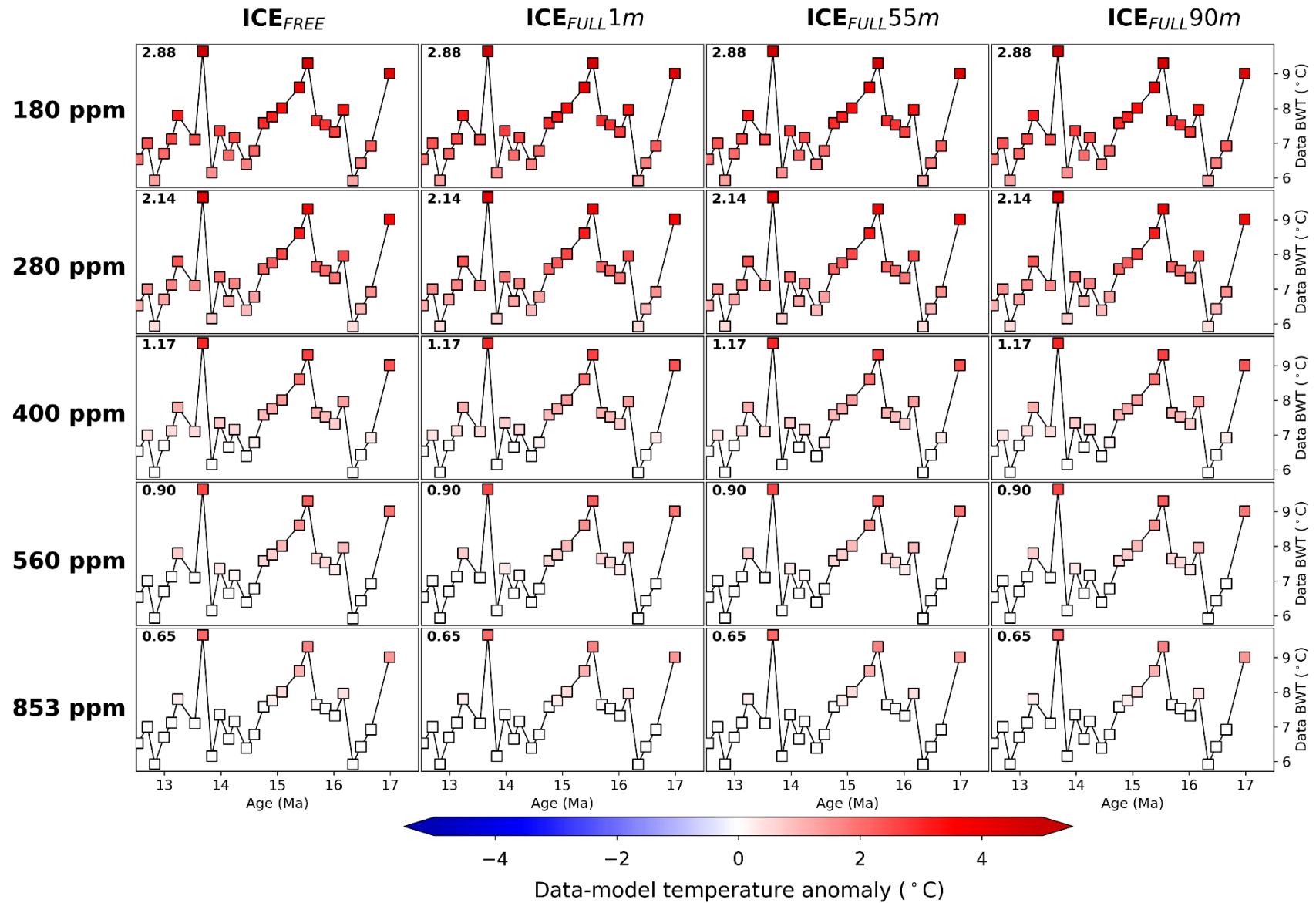
Supplementary Figure S40. Annual mean deep water temperature model-data comparison for Site 1171 in the Southern Ocean (Mg/Ca). Data from Shevenell et al., 2008⁵ as given in Supplementary Table S11. Legend information as in Supplementary Figure S2.



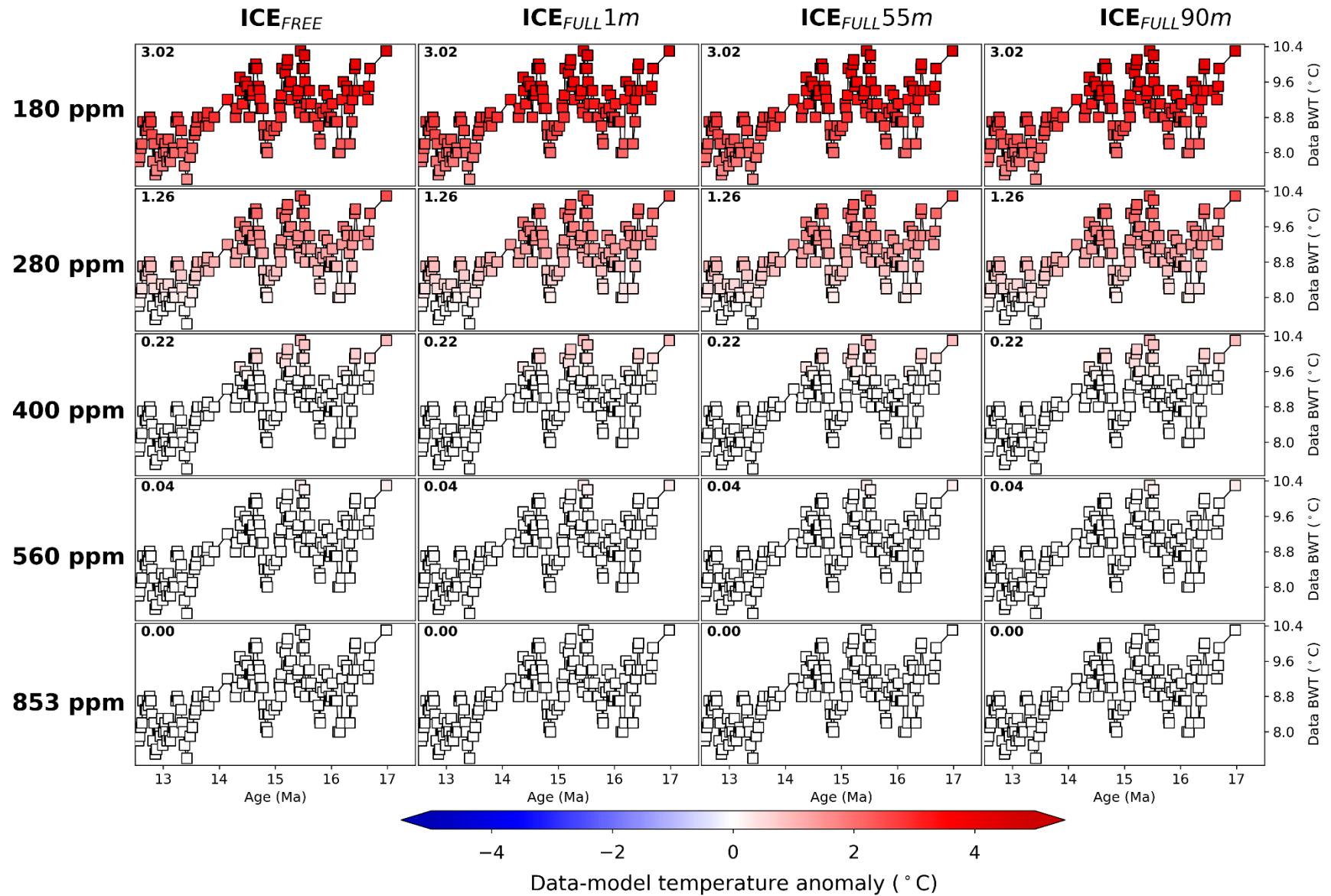
Supplementary Figure S41. Annual mean deep water temperature model-data comparison for Site U1338 in the Tropical Pacific (Mg/Ca). Data from Kochhann et al., 2017²⁶ as given in Supplementary Table S11. Legend information as in Supplementary Figure S2.



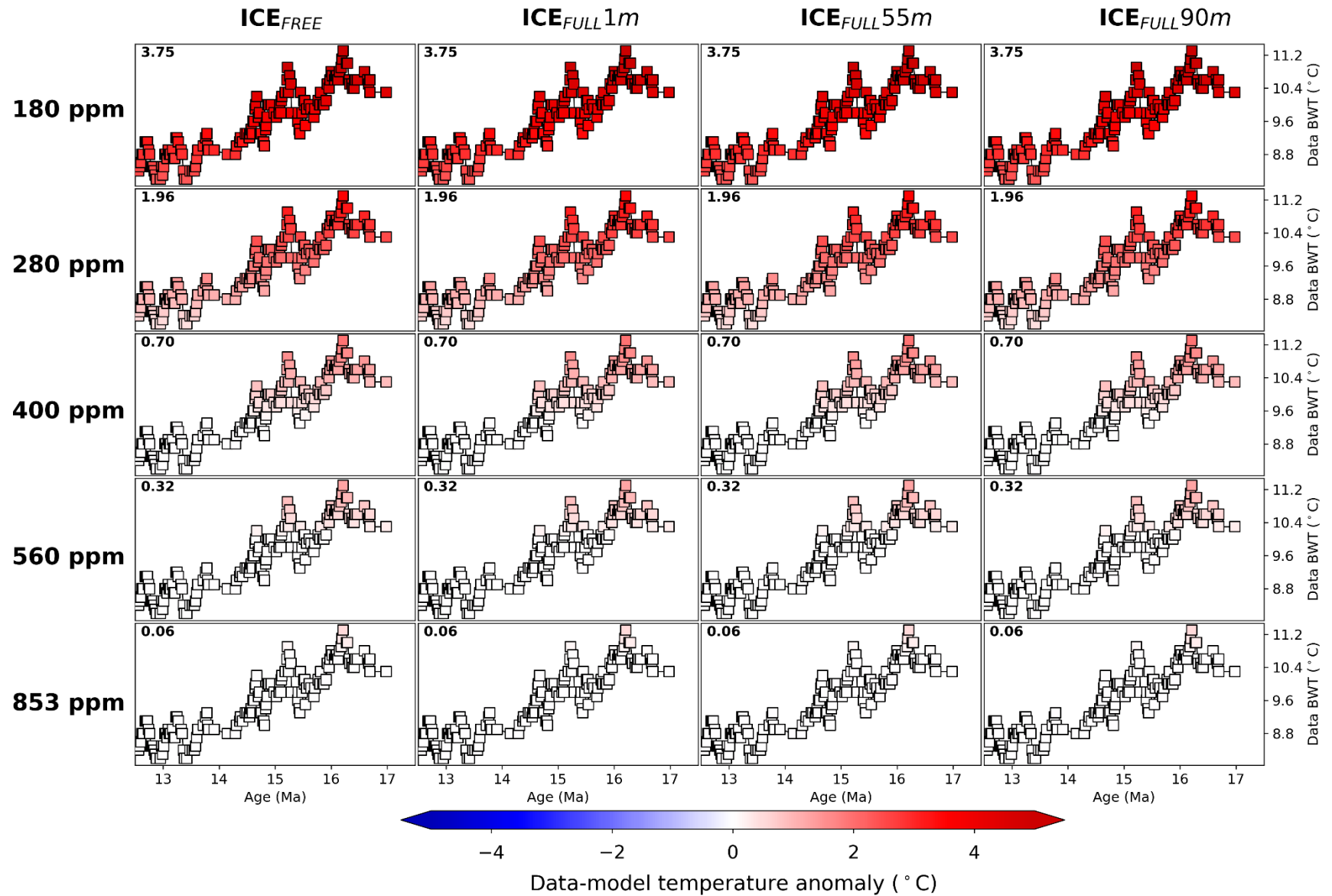
Supplementary Figure S42. Annual mean deep water temperature model-data comparison for Site 806 in the Tropical Pacific (Mg/Ca). Linear-fit data from Lear et al., 2015⁹ as given in Supplementary Table S11. Legend information as in Supplementary Figure S2.



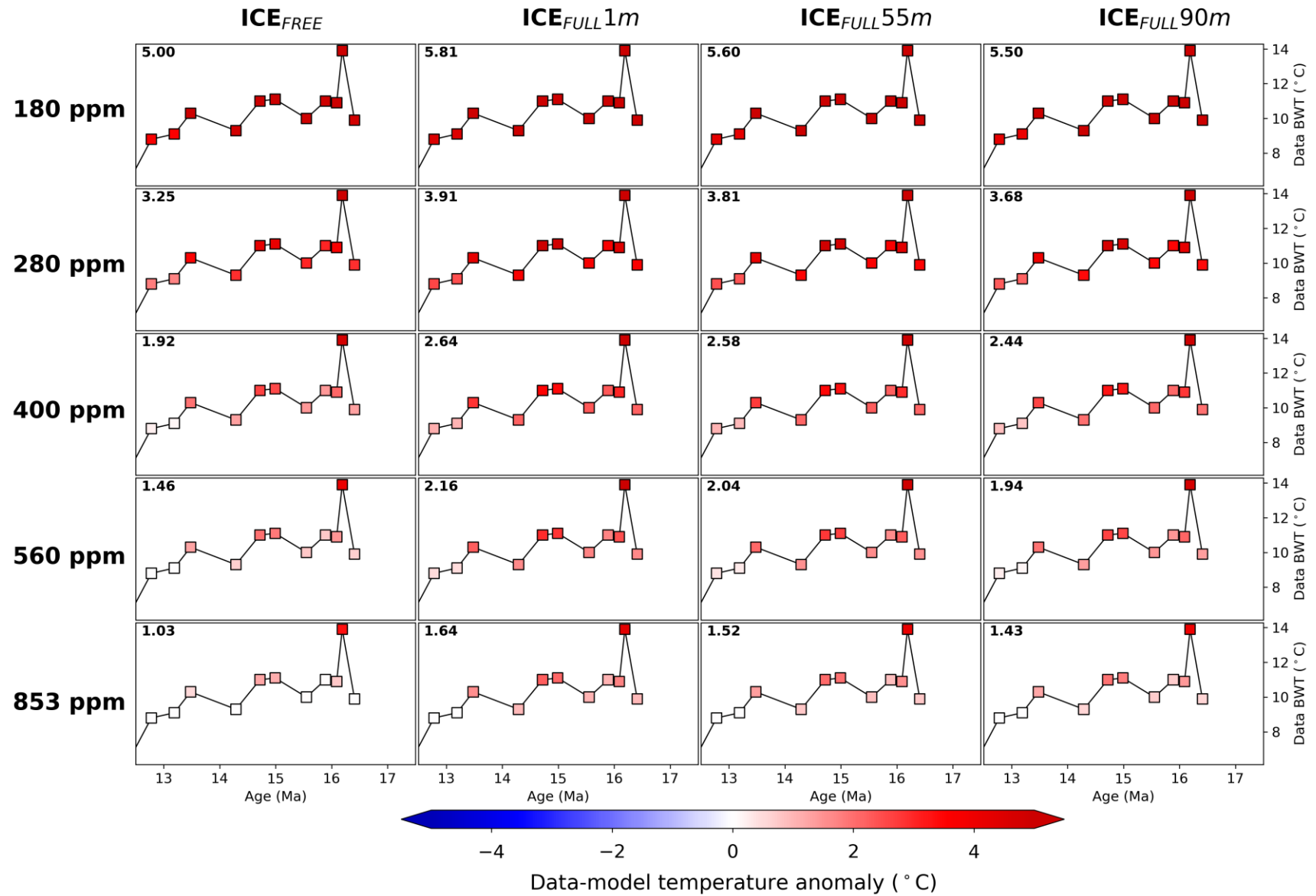
Supplementary Figure S43. Annual mean deep water temperature model-data comparison for Site 806 in the Tropical Pacific (Mg/Ca). Exponential-fit data from Lear et al., 2015⁹ as given in Supplementary Table S11. Legend information as in Supplementary Figure S2.



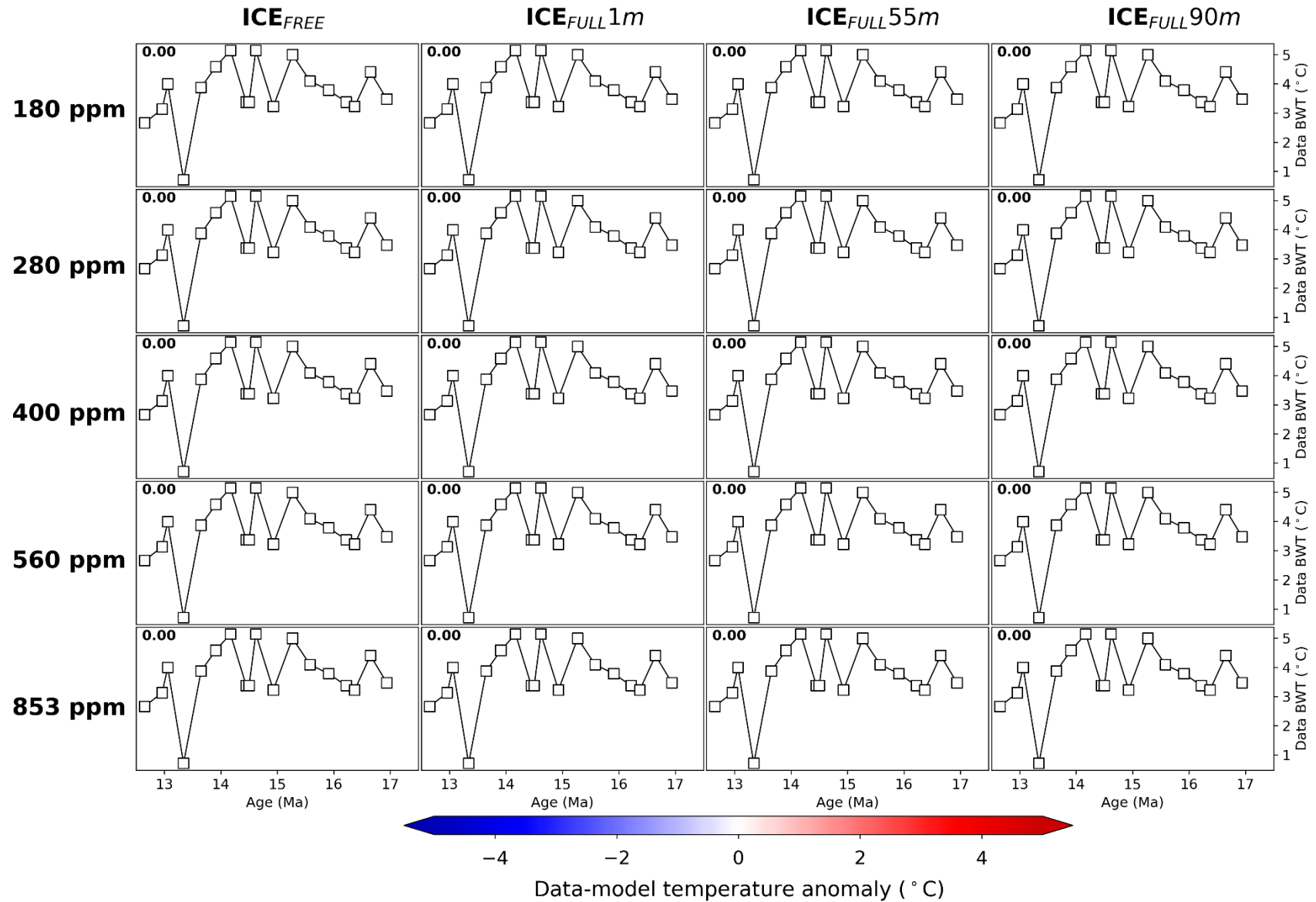
Supplementary Figure S44. Annual mean deep water temperature model-data comparison for Site 761 in the Indian Ocean (Mg/Ca). Unadjusted-data from Lear et al., 2010⁸ as given in Supplementary Table S11. Legend information as in Supplementary Figure S2.



Supplementary Figure S45. Annual mean deep water temperature model-data comparison for Site 761 in the Indian Ocean (Mg/Ca). Adjusted -data from Lear et al., 2010⁸ as given in Supplementary Table S11. Legend information as in Supplementary Figure S2.



Supplementary Figure S46. Annual mean deep water temperature model-data comparison for Site 761 in the Indian Ocean ($\Delta 47$). Data from Modestou et al., 2020³⁷ as given in Supplementary Table S11. Legend information as in Supplementary Figure S2.



Supplementary Figure S47. Annual mean deep water temperature model-data comparison for Site 747 in the Southern Ocean (Mg/Ca). Data from Billups and Schrag, 2002²⁷ as given in Supplementary Table S11. Legend information as in Supplementary Figure S2.

S2. Supplementary Discussion

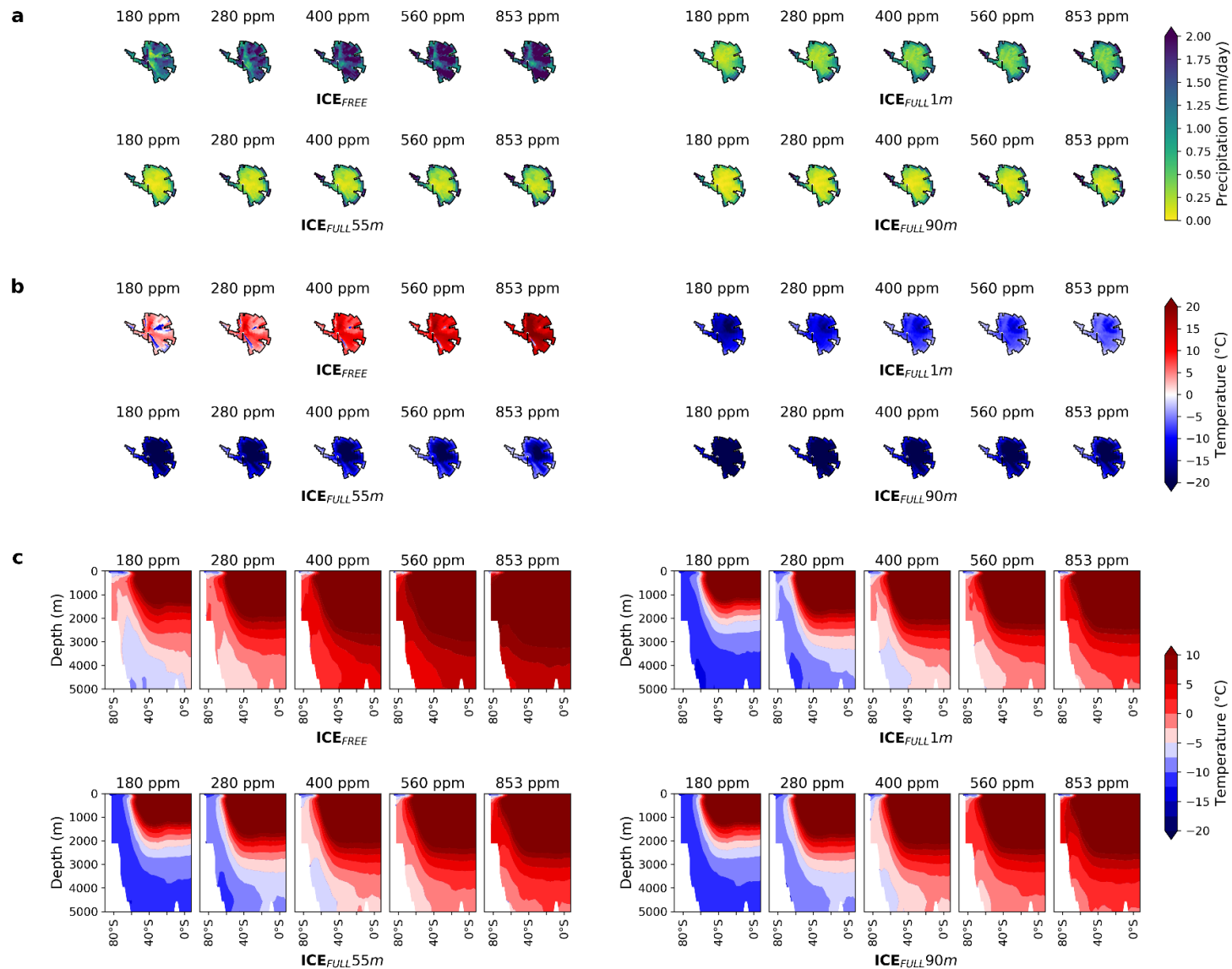
A. Ocean response to glaciation

Although the broad features of our mechanism appear insensitive to the CO₂ concentration (Supplementary Figure S48), we do find evidence that the Southern Ocean sea surface temperature response to glaciation is very sensitive to the underlying CO₂ concentration, and that the relationship is non-linear (Supplementary Figures S49 to S51). In our model, glaciation-driven topographic forcing (ICE_{FULL1m} to ICE_{FULL55m}) results generally in sea surface warming at the global scale, as also found with a similar scenario using the ECHAM5-MPIOM model²⁸, but we also find divergent trends as the CO₂ concentration either increases or decreases away from our mid-range concentration of 400 ppm (Supplementary Figure S49). This is because of the non-linearities of the winds and sea ice response to CO₂ forcing (Supplementary Figures S52 to S57). We find these non-linearities arise in both summer and winter when we consider just the albedo/surface roughness change (ICE_{FREE} to ICE_{FULL1m}; Supplementary Figures S54 and S56) but only during the summer for winds and winter for sea ice when we consider just the topographic change (ICE_{FULL1m} to ICE_{FULL55m}; Supplementary Figures S51 and S55). When both aspects are combined (ICE_{FREE} to ICE_{FULL55m}), the sea surface temperature responses to glaciation at different CO₂ concentrations become quite complex (Supplementary Figure S51).

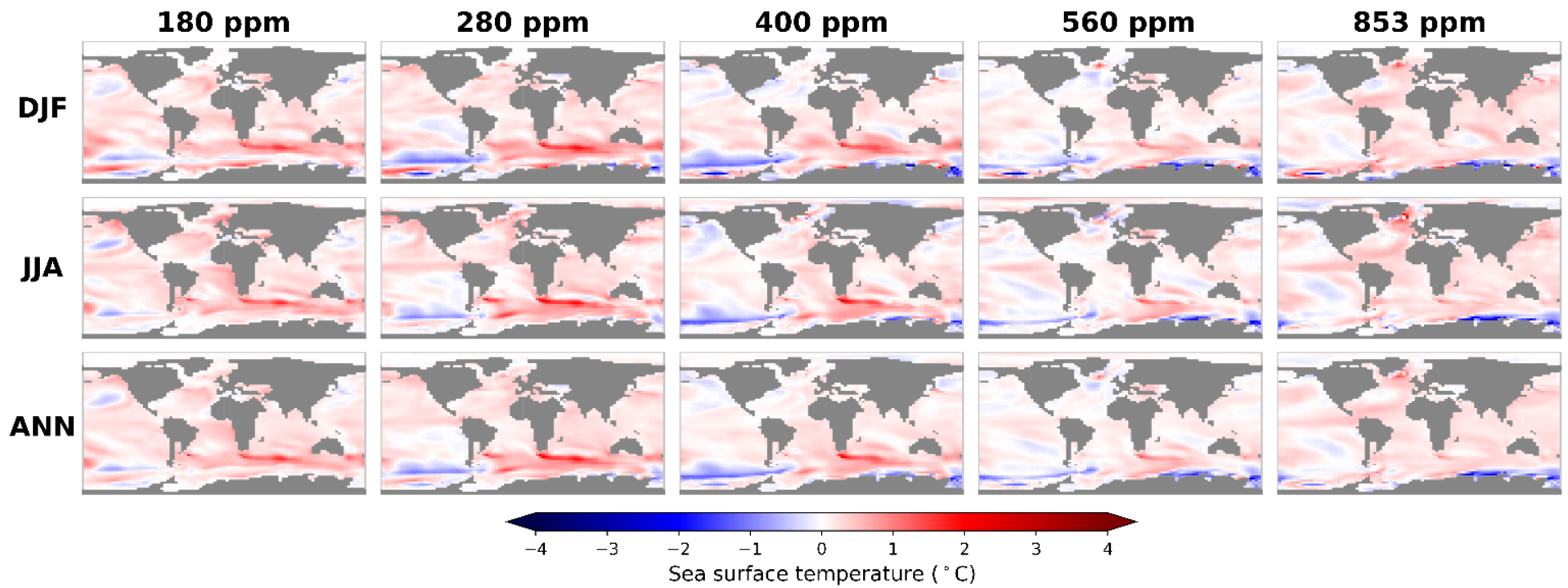
The result of these different surface responses to glaciation results in some differing responses in the deep ocean too. Firstly, although we see a slight cooling of deep waters close to Antarctica in the Ross Sea sector in response to topographic change, the Weddell Sea and most of the deep ocean actually warms slightly (ICE_{FULL1m} to ICE_{FULL55m}; Supplementary Figures S58 and S61a). This is the opposite result to that found for the similar scenario with the ECHAM5-MPIOM model²⁸. The topography-driven DWT changes, although small in magnitude, do show some non-linearities as well. The 400 ppm CO₂ scenario shows the most cooling in the Ross Sea sector and the 853 ppm CO₂ scenario showing a patch in this region ~120°W with the opposite sign of change. Although the albedo/surface roughness change (ICE_{FREE} to ICE_{FULL1m}, Supplementary Figures S59 and S61b) also shows some non-linear behaviour in the magnitude of the DWT response, the direction of the changes is consistent. Because the response to albedo/surface roughness changes dominates the combined DWT response to Antarctic glaciation

(topography, albedo and surface roughness together), this pattern looks very similar to the albedo/surface roughness response (Supplementary Figures S60 compared to S59, Supplementary Figure S61c compared to S61b). We suggest therefore, that the reason our mechanism operates in the same way between our 280 ppm and 853 ppm longitudinal ice growth scenarios is because the mechanism is largely independent of sea ice concentration.

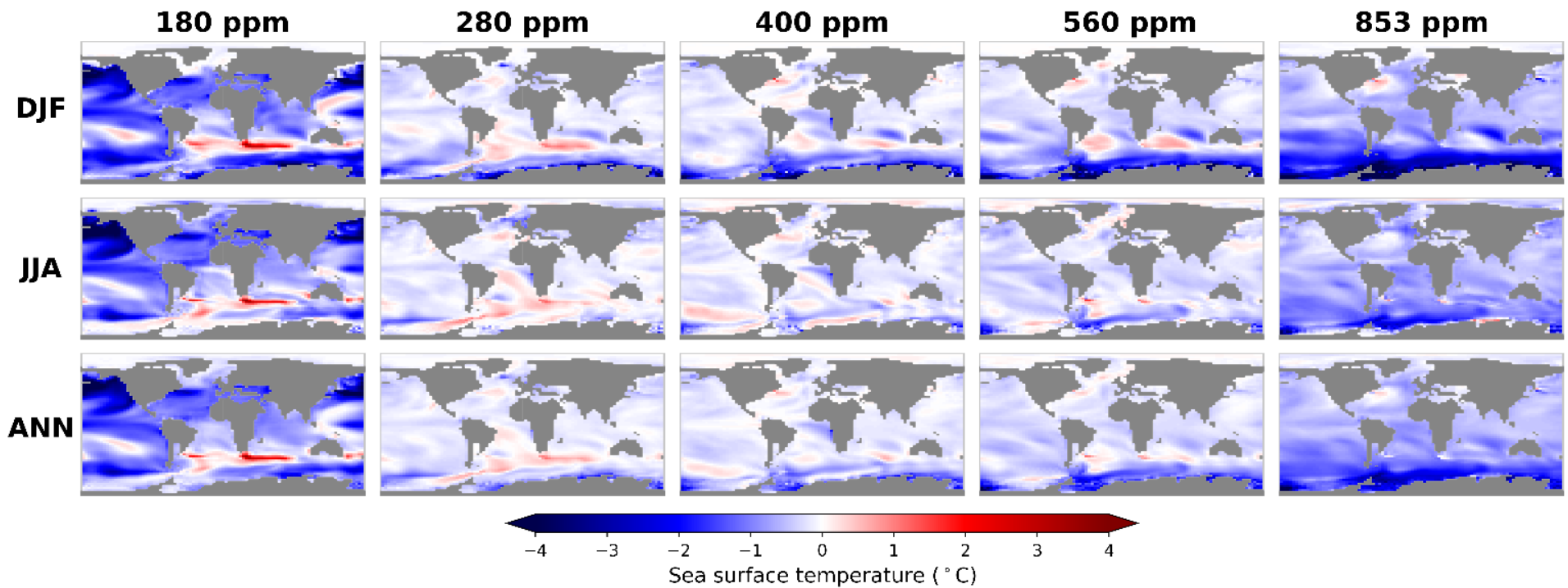
However, there are now two mechanisms capable of explaining the decoupling of ice volume and DWT at the MMCT glaciation; one involving winds and sea ice²⁸ and our new mechanism involving precipitation and runoff. The fact these two mechanisms result in the opposite sign of change for DWTs for a similar scenario, and of course the fact that both are likely important and interact, suggests there is a need for a Miocene model intercomparison project to establish the importance of the different boundary conditions versus the different models used. Scenarios to test alternative regional scale ice sheet configurations at higher CO₂ are recommended, and to consider ice shelf and meltwater processes not included in our model.



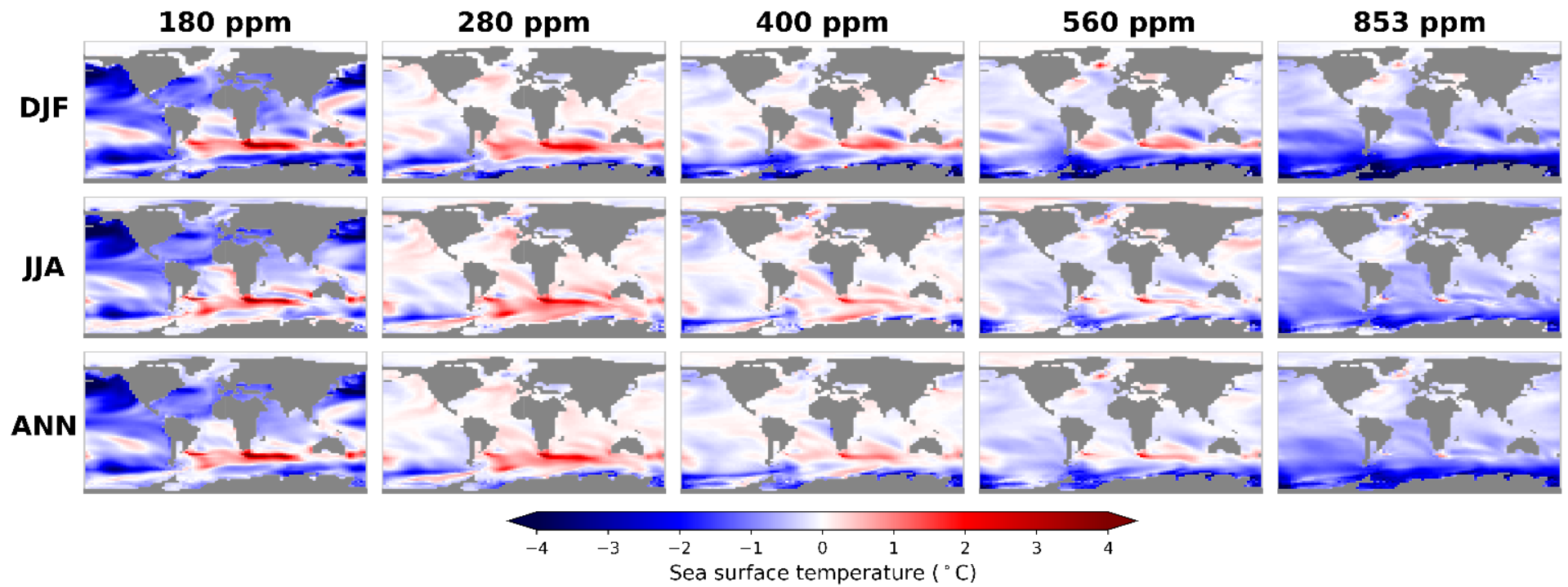
Supplementary Figure S48. Simulated atmospheric and oceanographic conditions in response to changes in CO₂ for different Antarctic ice sheet configurations. (a) Antarctic summer (DJF) precipitation, (b), Antarctic summer air temperature, (c), Annual mean Southern Hemisphere meridional mean ocean temperature. Refer to Fig. 2 for more details of the boundary conditions used.



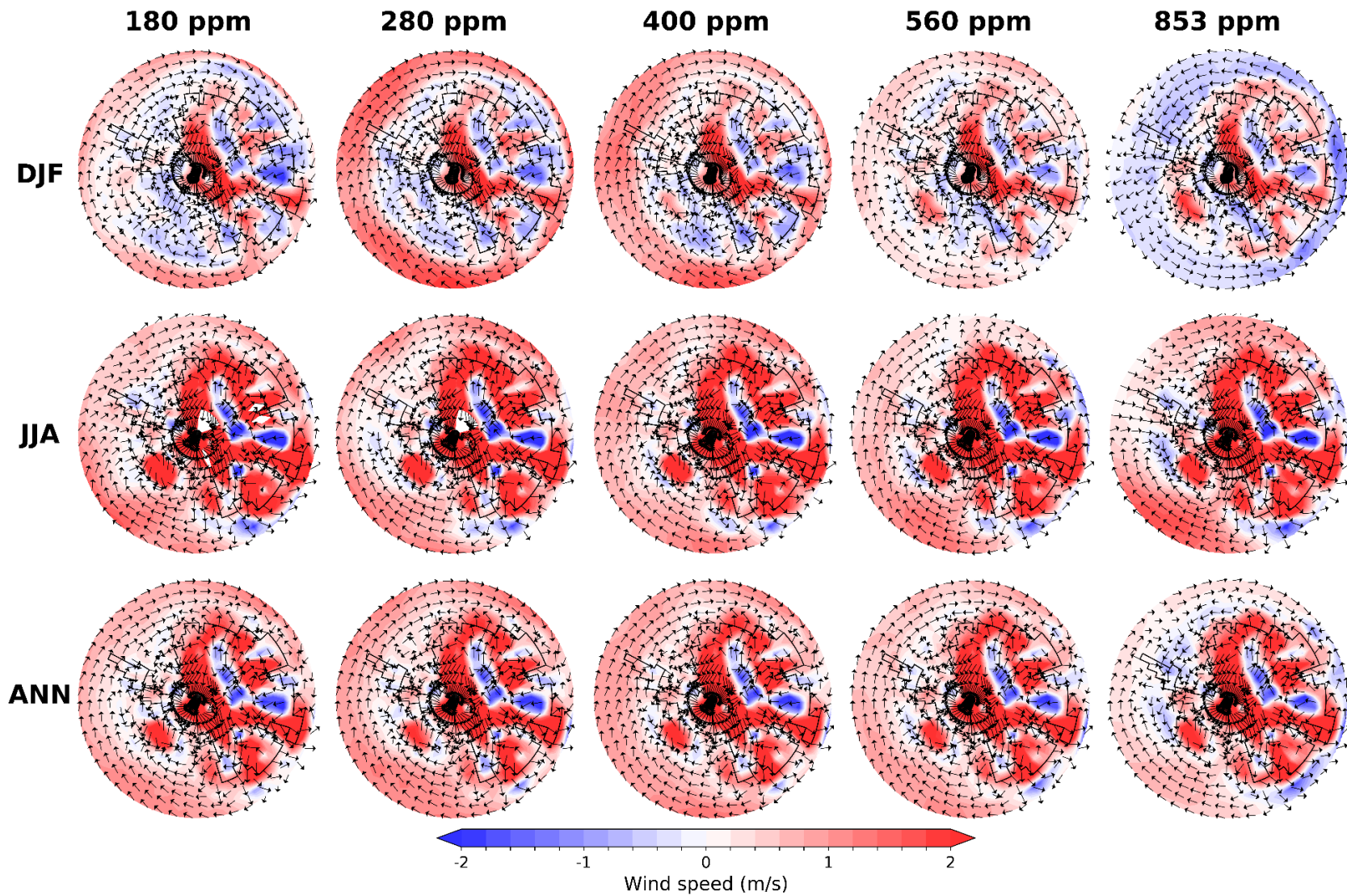
Supplementary Figure S49. Simulated sea surface temperatures in response to glaciation (topography changes only) for different CO₂ concentrations (ICE_{FULL55m}–ICE_{FULL1m}). Refer to Fig. 2 for more details of the boundary conditions used.



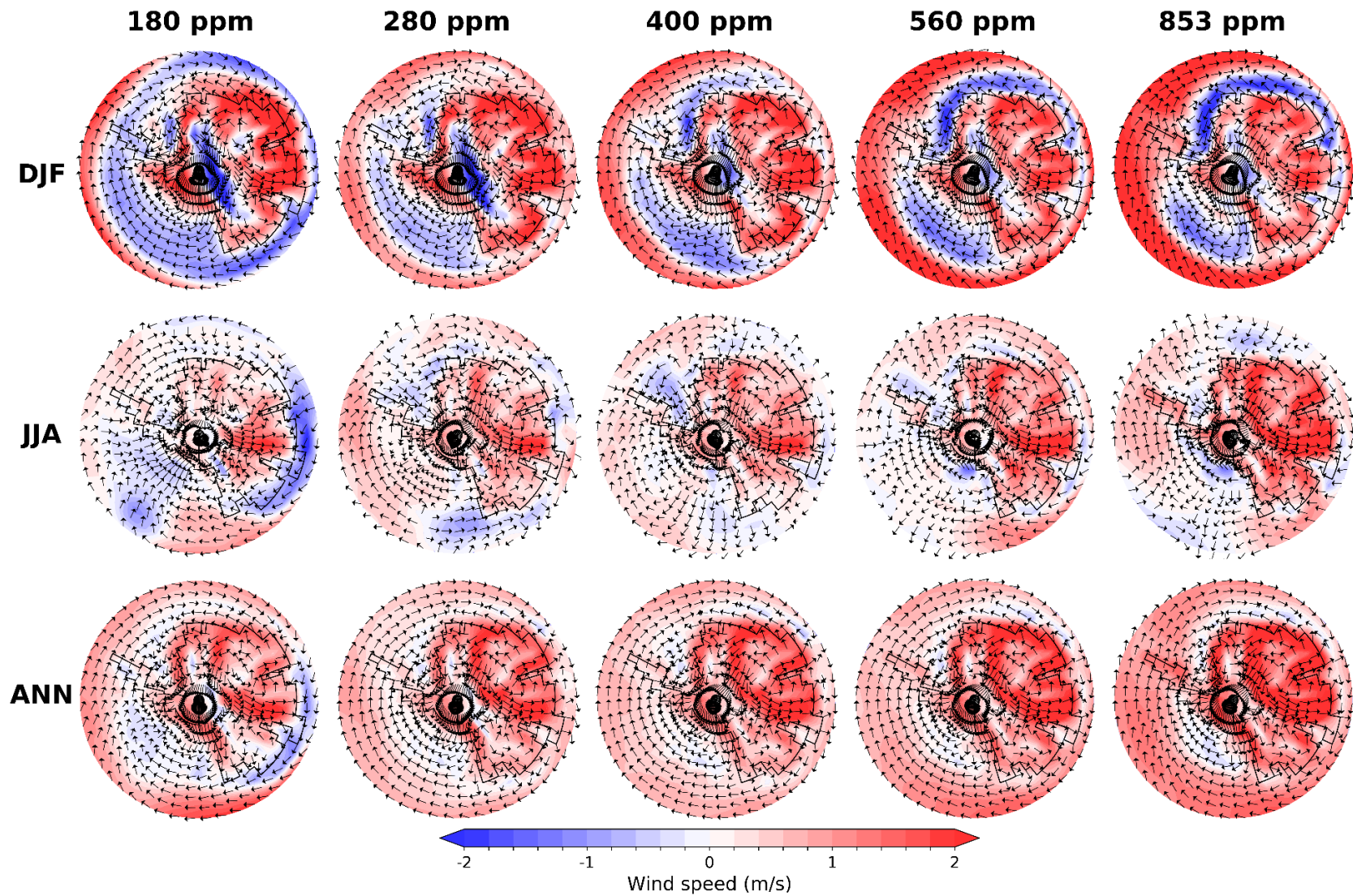
Supplementary Figure S50. Simulated sea surface temperatures in response to glaciation (albedo and surface roughness changes only) for different CO₂ concentrations (ICE_{FULL1m}–ICE_{FREE}). Refer to Fig. 2 for more details of the boundary conditions used.



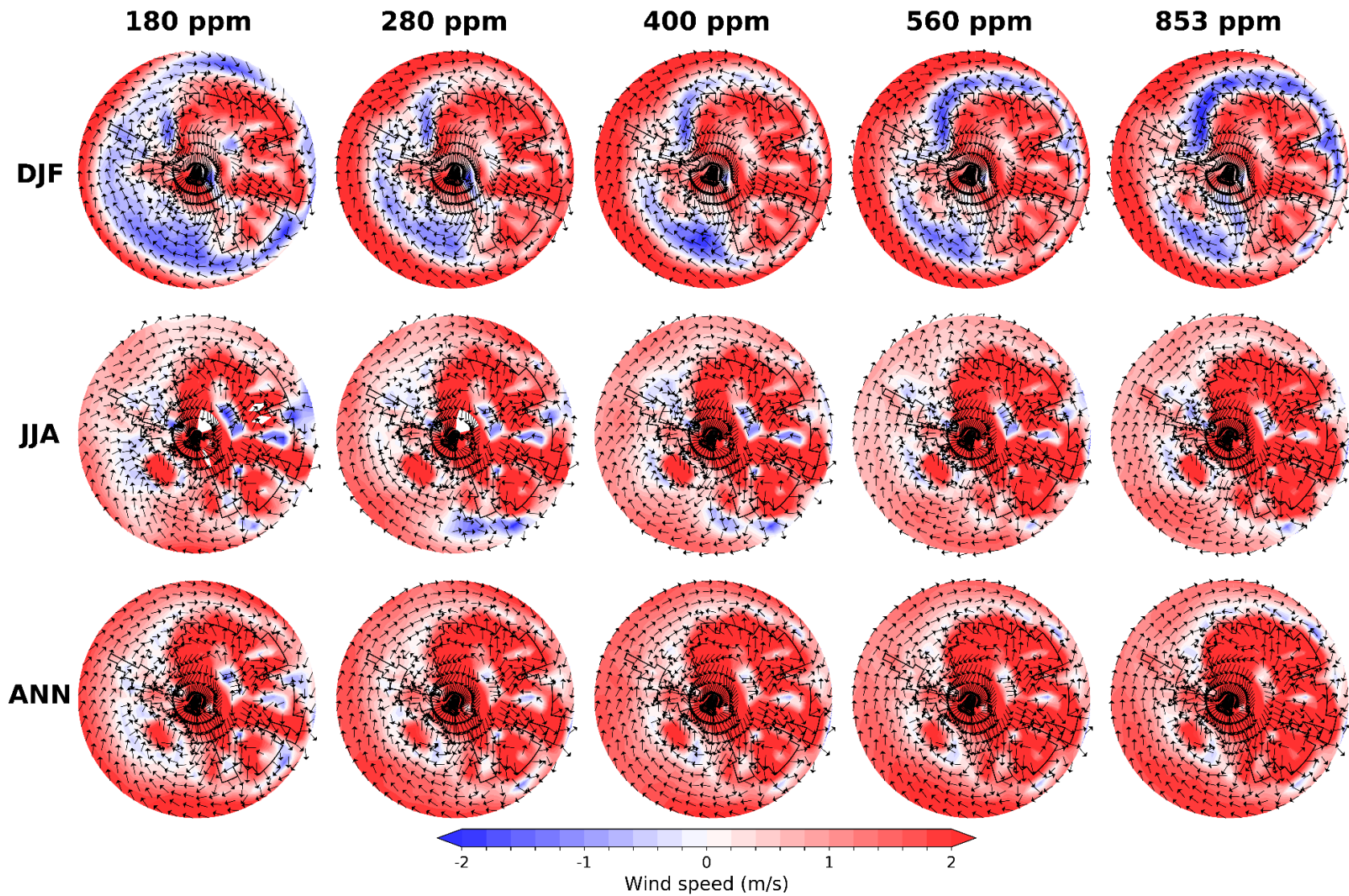
Supplementary Figure S51. Simulated sea surface temperatures in response to glaciation (albedo, surface roughness and topography changes) for different CO₂ concentrations (ICE_{FULL55m}–ICE_{FREE}). Refer to Fig. 2 for more details of the boundary conditions used.



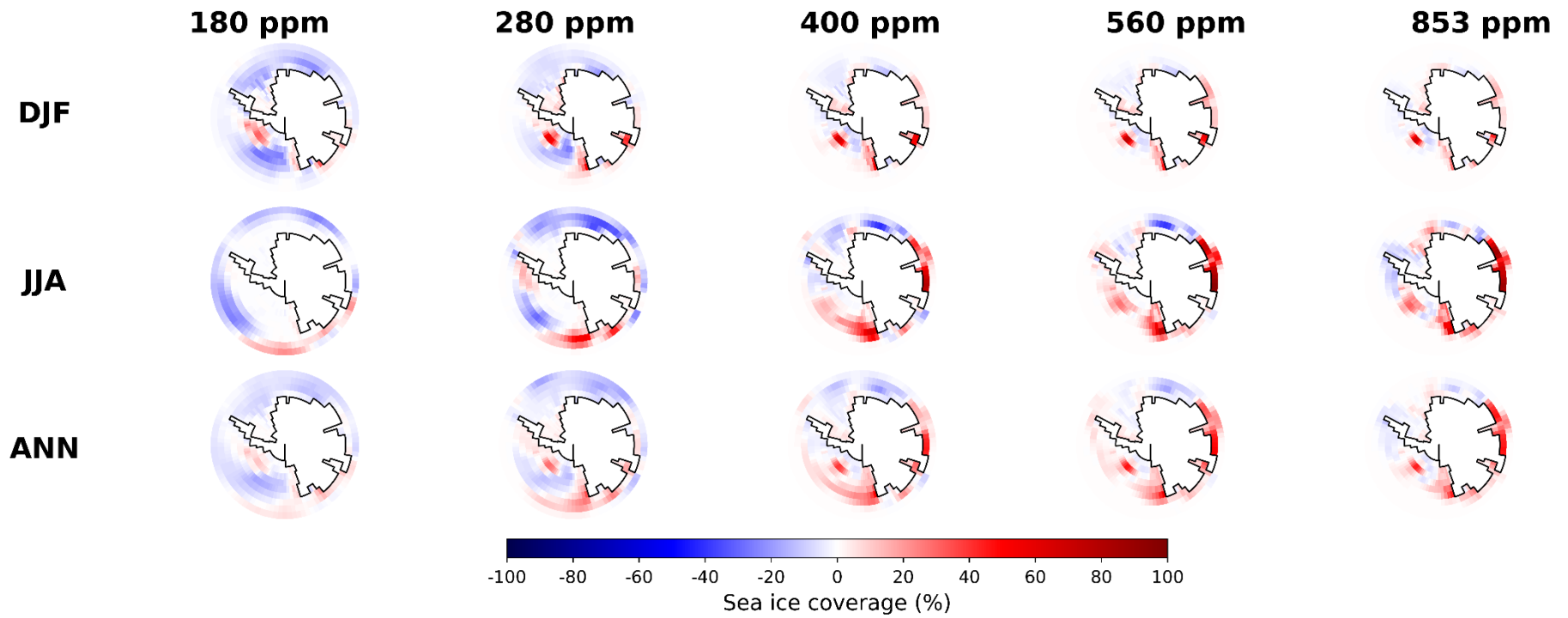
Supplementary Figure S52. Simulated 10m wind response to glaciation (topography changes only) for different CO₂ concentrations (ICE_{FULL55m}–ICE_{FULL1m}). Refer to Fig. 2 for more details of the boundary conditions used.



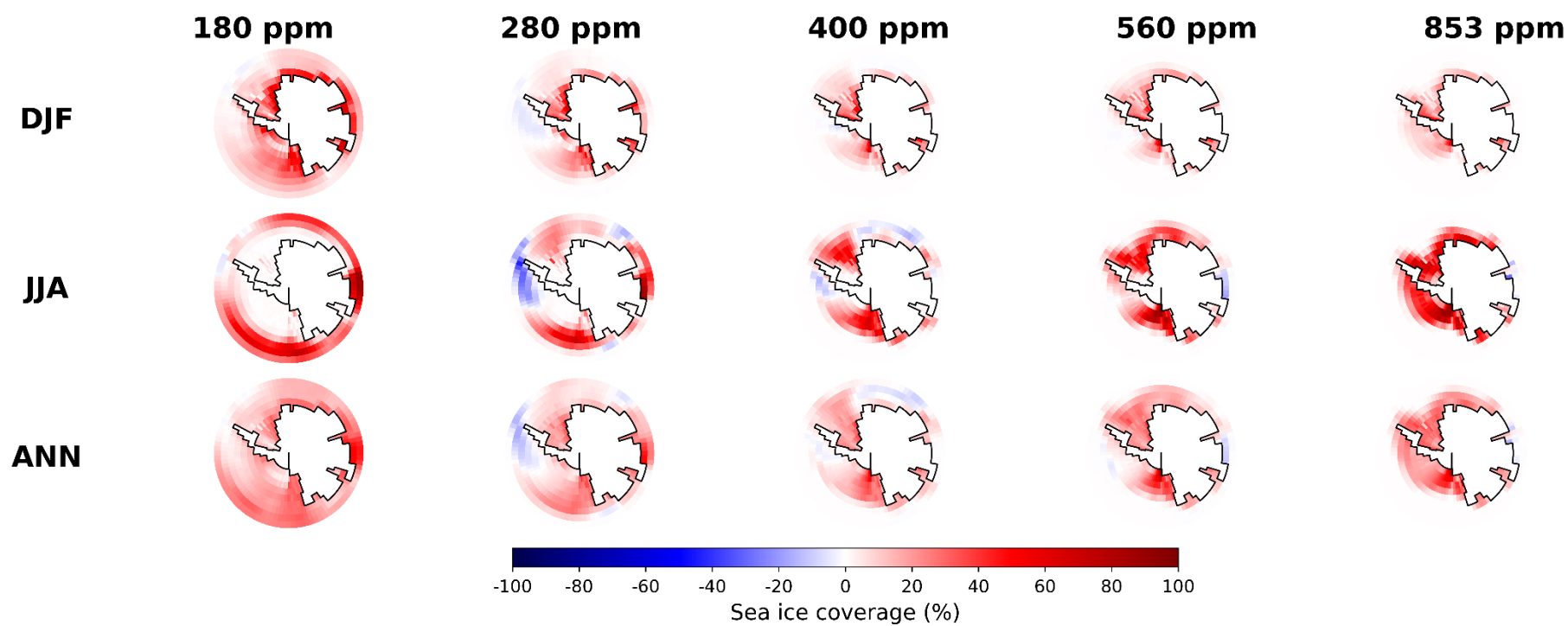
Supplementary Figure S53. Simulated 10m wind response to glaciation (albedo and surface roughness changes only) for different CO₂ concentrations (ICE_{FULL1m}–ICE_{FREE}). Refer to Fig. 2 for more details of the boundary conditions used.



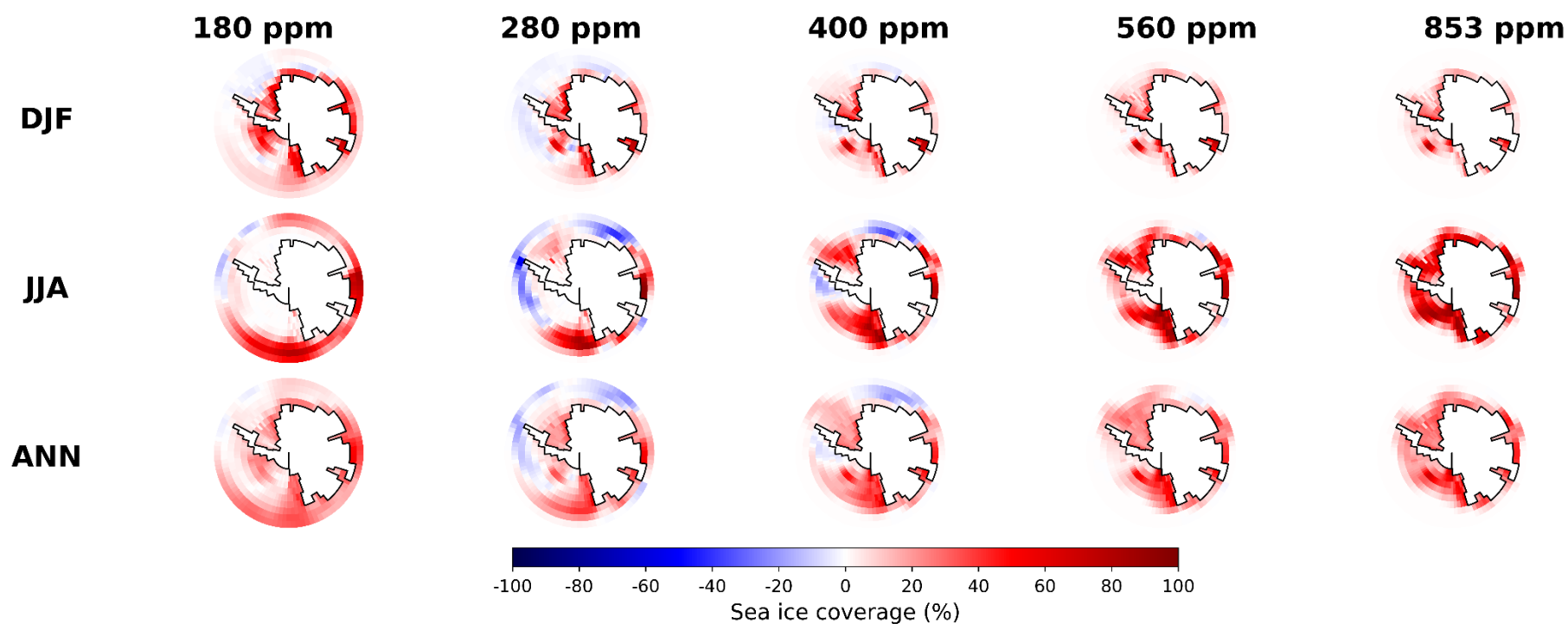
Supplementary Figure S54. Simulated 10m wind response to glaciation (albedo, surface roughness and topography changes) for different CO₂ concentrations (ICE_{FULL55m}–ICE_{FREE}). Refer to Fig. 2 for more details of the boundary conditions used.



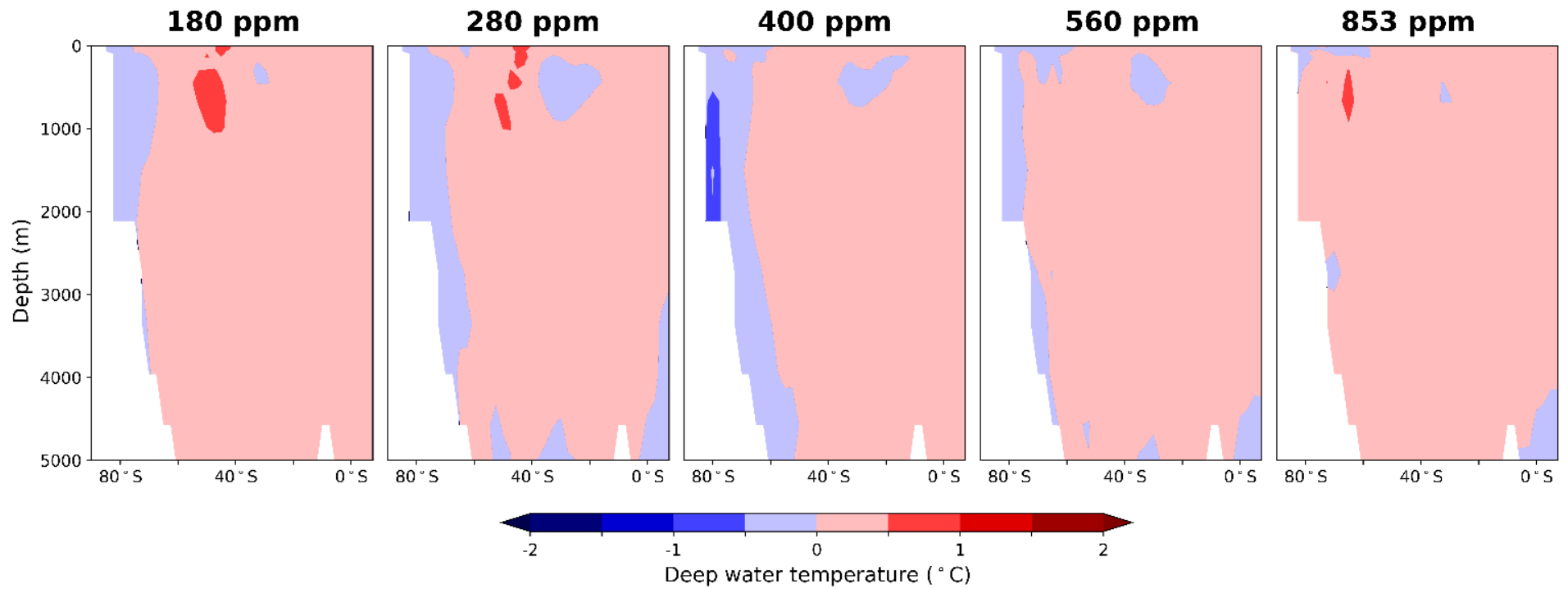
Supplementary Figure S55. Simulated sea ice concentration in response to glaciation (topography changes only) for different CO₂ concentrations (ICE_{FULL55m}–ICE_{FULL1m}). Refer to Fig. 2 for more details of the boundary conditions used.



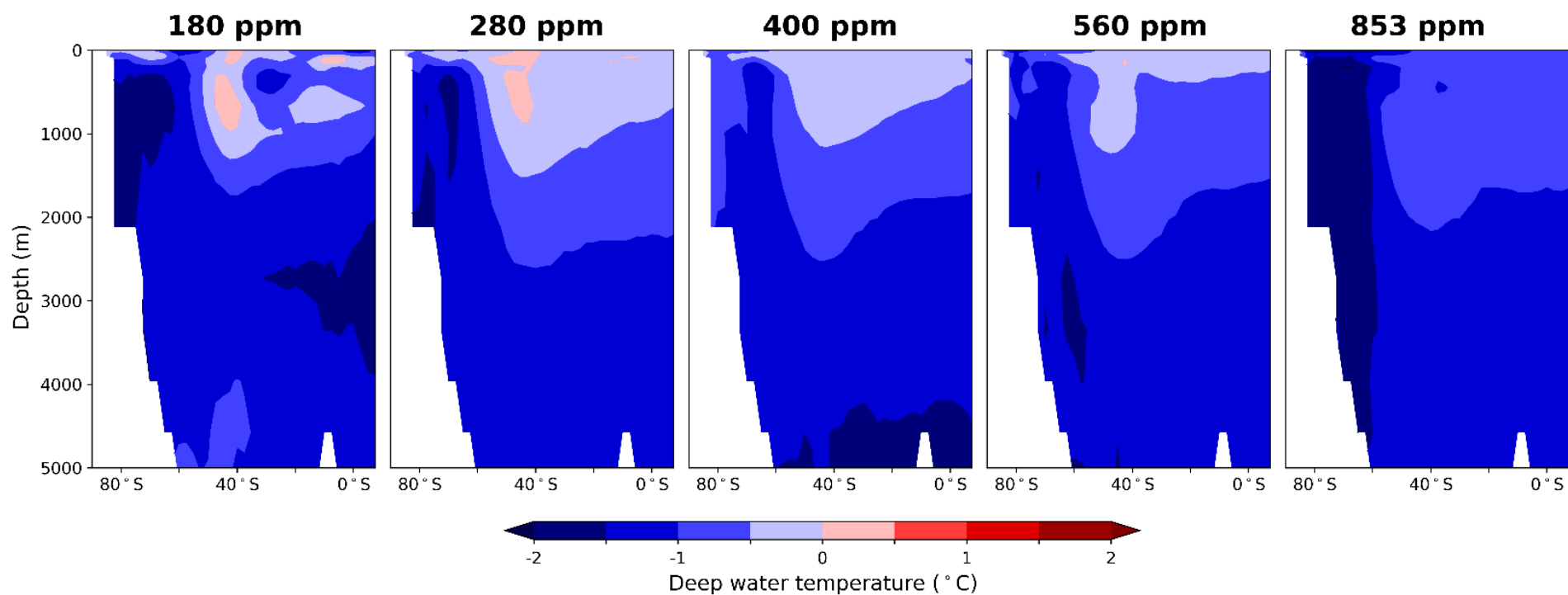
Supplementary Figure S56. Simulated sea ice concentration in response to glaciation (albedo and surface roughness changes only) for different CO₂ concentrations (ICE_{FULL1m}–ICE_{FREE}). Refer to Fig. 2 for more details of the boundary conditions used.



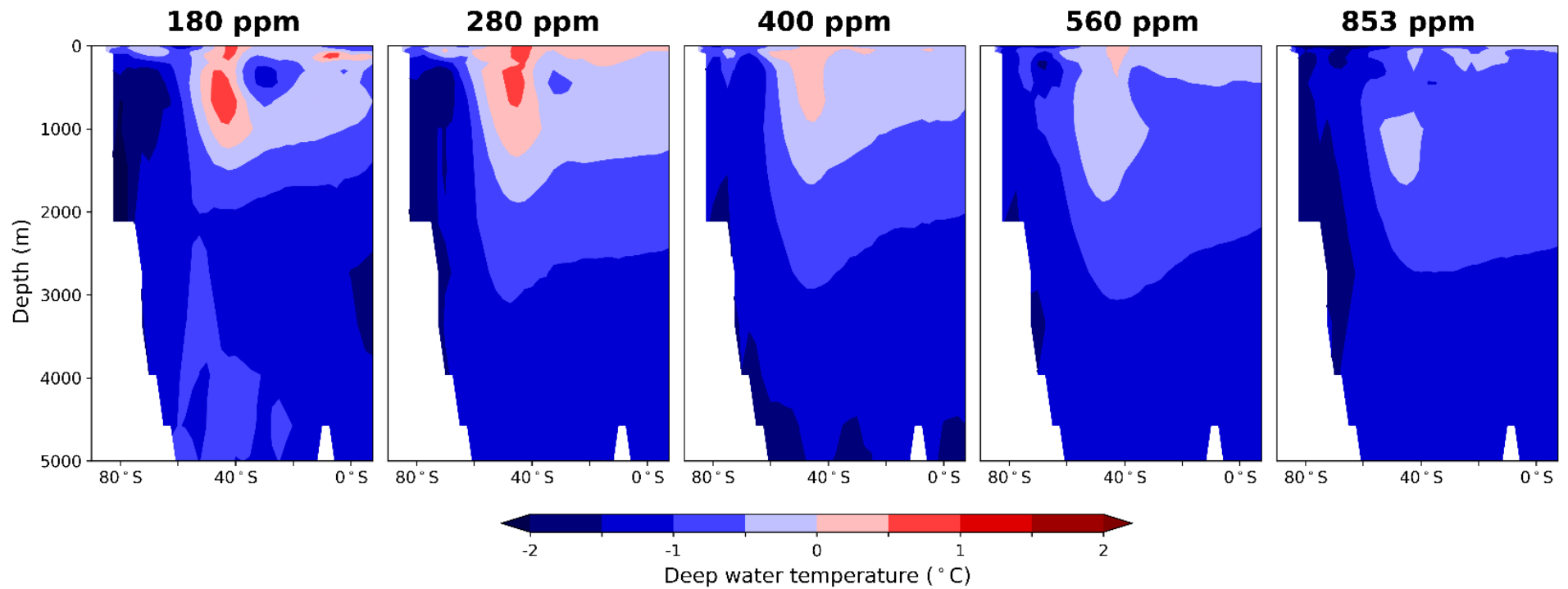
Supplementary Figure S57. Simulated sea ice concentration in response to glaciation (albedo, surface roughness and topography changes) for different CO₂ concentrations (ICE_{FULL55m}–ICE_{FREE}). Refer to Fig. 2 for more details of the boundary conditions used.



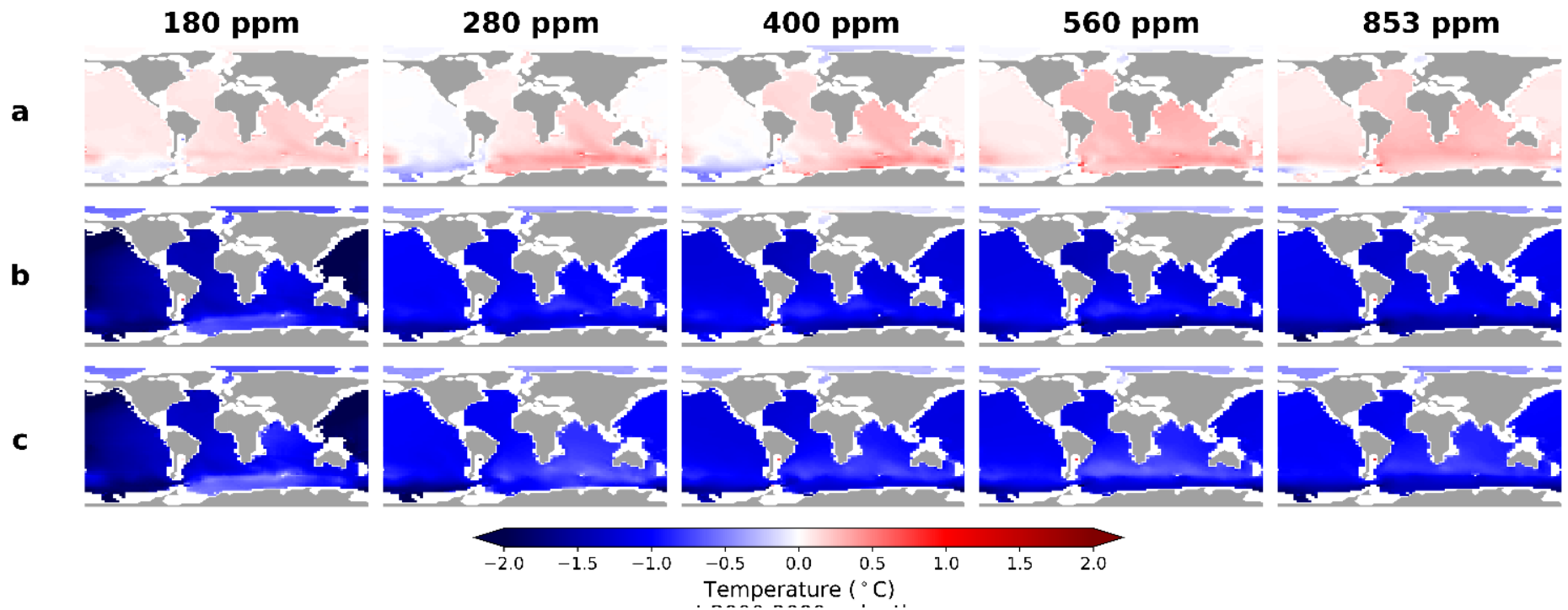
Supplementary Figure S58. Simulated deep water temperatures in response to glaciation (topography changes only) for different CO₂ concentrations (ICE_{FULL55m}–ICE_{FULL1m}). Refer to Fig. 2 for more details of the boundary conditions used.



Supplementary Figure S59. Simulated deep water temperatures in response to glaciation (albedo and surface roughness changes only) for different CO₂ concentrations (ICE_{FULL1m} – ICE_{FREE}). Refer to Fig. 2 for more details of the boundary conditions used.



Supplementary Figure S60. Simulated deep water temperature in response to glaciation (albedo, surface roughness and topography changes) for different CO₂ concentrations (ICE_{FULL55m} – ICE_{FREE}). Refer to Fig. 2 for more details of the boundary conditions used.



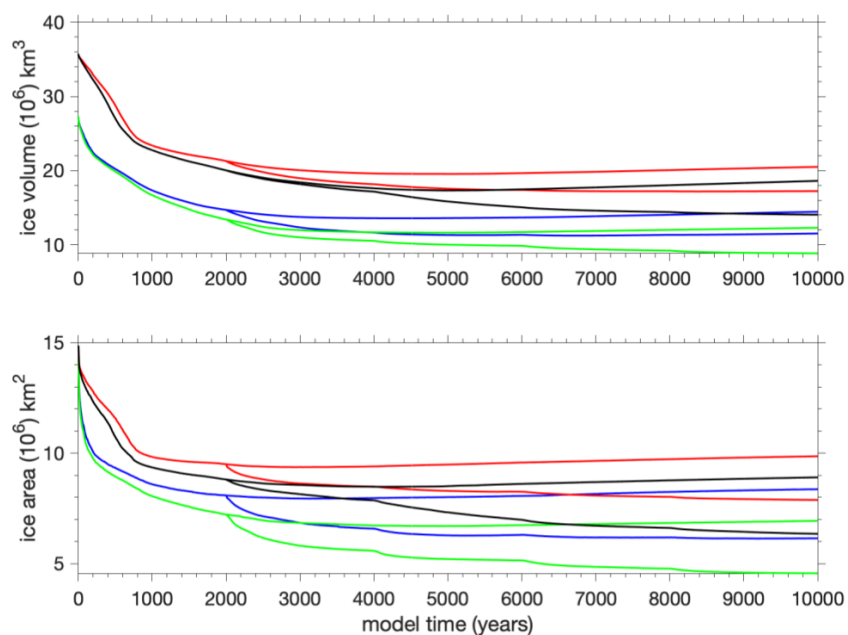
Supplementary Figure S61. Simulated deep water temperatures (2-3km depth) in response to glaciation for different CO₂ concentrations. (a). Topography changes only ($ICE_{FULL55m} - ICE_{FULL1m}$), **(b).** Albedo/surface roughness changes only ($ICE_{FULL1m} - ICE_{FREE}$) and **(c).** Albedo, surface roughness and topography changes ($ICE_{FULL55m} - ICE_{FREE}$). Refer to Fig. 2 for more details of the boundary conditions used.

B. Middle Miocene deep water production

In all of our middle Miocene simulations, deep water is in all cases primarily produced in the south; Atlantic Meridional Overturning Circulation in the Northern Hemisphere is weak (i.e. $<3\text{Sv}$, as compared to 18Sv for a pre-industrial simulation using the same model²) and there is no deep water production in the North Pacific (except for our ice-free 180 ppm CO_2 scenario, which is perhaps one of the most unrealistic). Modern North Atlantic Deep Water (NADW) is comprised of deep waters formed in both the Nordic seas and the Labrador Sea. Whilst there is evidence for the onset of deep convection in the Nordic Seas by the middle Miocene²⁹⁻³¹, the role of NADW (or its precursor, Northern Component Water, NCW) in the global ocean at this time is an open question. Benthic foraminifera carbon isotope compilations show similar values in all basins during the middle Miocene, interpreted to indicate that deep water formation came from a common southern source^{32,33}. However, recent work has shown that the geochemical signature of ancient NCW differed from modern values³¹, which implies that this interpretation may not be robust. Opal deposition, however, is a process indicating the presence of older less corrosive deep waters rather than NADW/NCW. Therefore, the fact that opal deposition at Site 642 in the Nordic Seas did not collapse until 14Ma ³⁴ provides support for a minor role for NCW in global ocean circulation during the MCO. Hence, we are confident that our model results are robust for the middle Miocene.

C. Relationship between ice sheet volume and ice sheet area

The relationship between ice volume and ice area for the ice sheet model used in Gasson et al., 2016³⁵ is approximately linear for ice sheet retreat (Supplementary Figure S62). Ice sheet growth simulations show a similar linear relationship (not shown).



Supplementary Figure S62. Timeseries of ice sheet volume and ice sheet area. Values are taken from the ice model simulations of Gasson et al., 2016³⁵ and the plot was provided by Edward Gasson. The simulations are blue (500ppm, bedmap2), green (840 ppm, bedmap2), red (500 ppm, ‘Miocene’ topography), black (840 ppm, ‘Miocene’ topography). The plots show the simulations both with and without asynchronous coupling of the ice sheet to the climate model.

D. Deep water temperature changes that can be accounted for from CO₂ forcing alone

In order to assess the contribution made from CO₂ forcing alone to the overall reported temperature changes at Site 1171 and Site 761 during the MCO and the MMCT glaciation, we perform linear interpolation of the results for the different CO₂ simulations conducted.

Average CO₂ variability during the MCO were of the order 630 - 470 ppm²². Supplementary Table S1 documents the DWT changes linearly interpolated for these CO₂ concentrations and suggest that CO₂ forcing accounts for between 0.5 and 0.6°C of temperature change.

	ICE _{FREE}	ICE _{FULL} 1m	ICE _{FULL} 55m	ICE _{FULL} 90m
Site 1171	0.6	0.6	0.5	0.5
Site 761	0.5	0.5	0.5	0.5

Supplementary Table S1. Simulated deep water temperatures (°C) for CO₂ changes estimated during the MCO (630-470 ppm²²) at Site 1171 in the Southern Ocean and at Site 761 in the Indian Ocean. Temperatures for the 630 ppm CO₂ scenarios are linearly interpolated between the 853 ppm and the 560 ppm CO₂ equivalent scenarios. Temperatures for the 470 ppm CO₂ scenarios are linearly interpolated between the 560 ppm and the 400 ppm CO₂ equivalent scenarios.

The magnitude of the CO₂ decline during the MMCT glaciation was at most 570-400 ppm²². Supplementary Table S2 documents the DWT changes linearly interpolated for these CO₂ concentrations and suggest that CO₂ forcing accounts for between 0.5 and 0.8°C of temperature change. These results therefore suggest a more important role for CO₂ changes in determining the DWT during the MMCT glaciation than the MCO (Supplementary Table S2 compared to S1), consistent with the results of a new study, which concluded that CO₂ has a direct role in driving the MMCT ice growth event²⁰.

	ICE _{FREE}	ICE _{FULL} 1m	ICE _{FULL} 55m	ICE _{FULL} 90m
Site 1171	0.6	0.8	0.6	0.5
Site 761	0.6	0.6	0.6	0.5

Supplementary Table S2. Simulated deep water temperatures (°C) for CO₂ changes estimated during the MMCT glaciation (570-400 ppm²²) at Site 1171 in the Southern Ocean and at Site 761 in the Indian Ocean. Temperatures for the 570 ppm CO₂ scenarios are linearly interpolated between the 853 ppm and the 560 ppm CO₂ equivalent scenarios.

E. Deep water temperature changes that can be accounted for from surface albedo and roughness forcing alone

In order to assess the contribution made to the overall reported temperature changes at Site 1171 and Site 761 from our mechanism during the MCO, we compare the deep water temperature changes between our ICE_{FREE} and our ICE_{FULL1m} scenarios for the different CO₂ concentrations simulated. Supplementary Table S3 shows that these surface albedo and roughness changes account for between 0.9 and 1.9°C of temperature change.

	CO ₂ concentration				
	180 ppm	280 ppm	400 ppm	560 ppm	853 ppm
Site 1171	1.5	1.0	1.2	1.1	1.4
Site 761	1.9	0.9	1.1	1.2	1.1

Supplementary Table S3. Simulated deep water temperature changes (°C) due to surface albedo and roughness changes estimated during the MCO (anomaly between ICE_{FULL1m} and ICE_{FREE}).

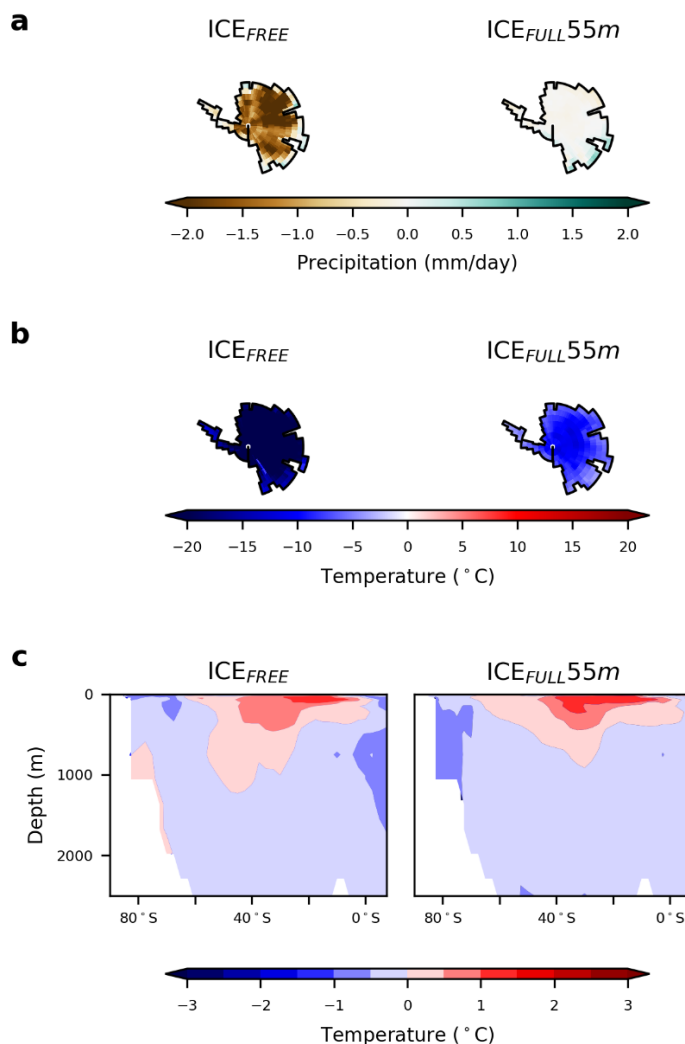
In order to assess the contribution made to the overall reported temperature changes at Site 1171 and Site 761 from our mechanism during the MMCT glaciation, we compare the deep water temperature changes between our ICE_{FULL1m} and our ICE_{FULL55m} scenarios for the different CO₂ concentrations simulated. Supplementary Table S4 shows that these topographic changes result in temperature changes spanning no change at all, up to 0.5°C of warming.

	CO ₂ concentration				
	180 ppm	280 ppm	400 ppm	560 ppm	853 ppm
Site 1171	-0.4	-0.5	-0.4	-0.2	-0.3
Site 761	0.0	-0.1	-0.2	-0.3	-0.2

Supplementary Table S4. Simulated deep water temperature changes (°C) due to topographic changes estimated during the MMCT glaciation (anomaly between ICE_{FULL55m} and ICE_{FULL1m}).

F. Sensitivity to orbital configuration

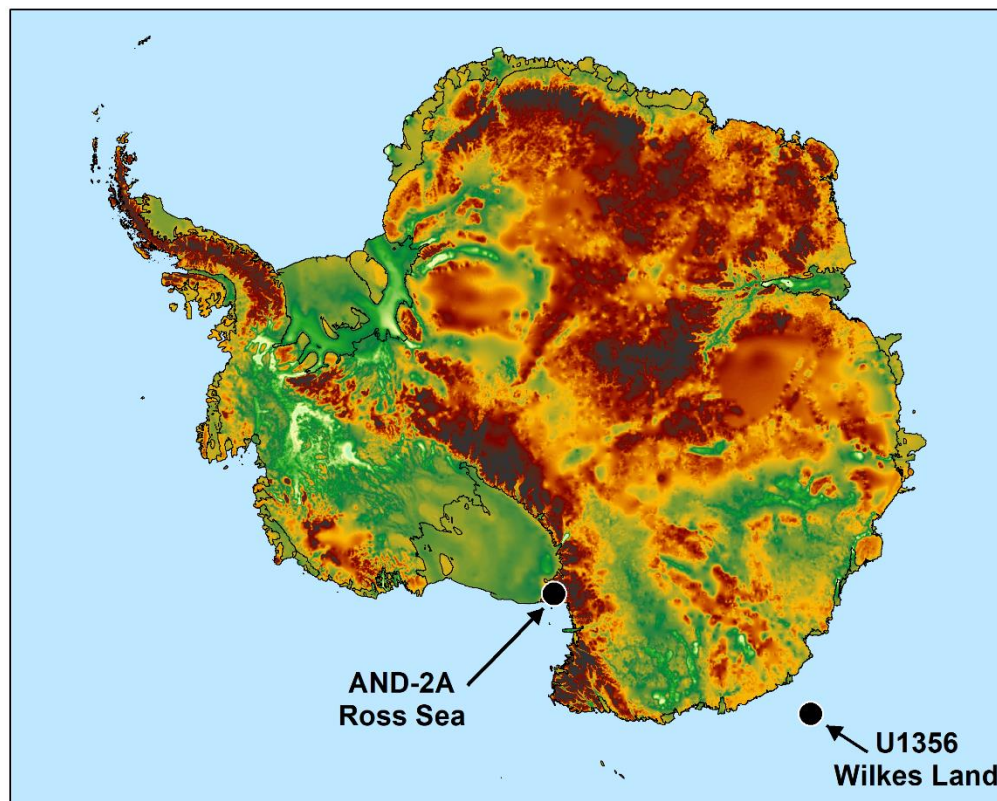
In further orbital forcing sensitivity tests (refer to Methods), we find a minimal effect on DWT: the anomaly between extreme Southern Hemisphere warm and cold orbit conditions is just 0.2-0.3°C (Supplementary Figure S63). In the ICE_{FREE} extreme cold orbit scenario, interior continental temperatures become cold enough to likely support an ice sheet. Coastal surface temperatures, however, remain above zero meaning that snowfall melts, runoff occurs and our mechanism reducing AABW production still operates. DWT changes in the extreme warm orbit ICE_{FULL55m} scenario relate to significant sea ice reductions (not shown).



Supplementary Figure S63. Simulated atmospheric and oceanographic conditions in response to changes in orbital configuration for different Antarctic ice sheet configurations. (a) Antarctic summer (DJF) precipitation, (b), Antarctic summer air temperature, (c), Annual mean Southern Hemisphere meridional mean ocean temperature. The left panels show the model results for the anomaly between the extreme cold orbit configuration and the extreme warm orbit configuration for an ice-free Antarctica. The right panels show the model results for the anomaly between the extreme cold orbit configuration and the extreme warm orbit configuration for 55m sea level equivalent scenario. Refer to Fig. 2 for more details of the boundary conditions used.

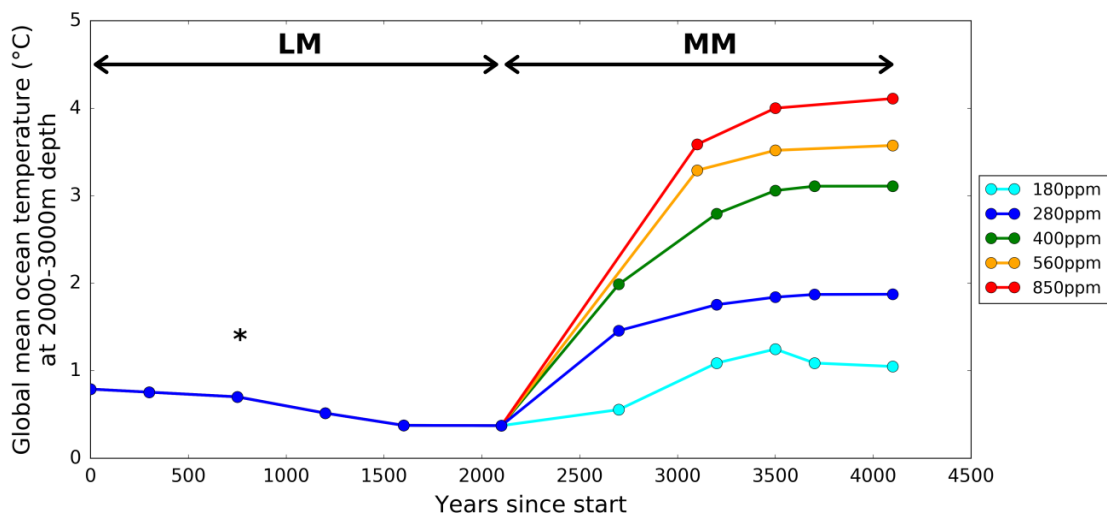
G. A potential mechanism for asynchronous advance of different ice sheet catchments

Major ice advance onto the continental shelf in the Ross Sea^{21,36} occurred at the same time as the presence of open water and woody vegetation in the Wilkes Land¹³ during the MCO (locations shown in Supplementary Figure S64). Although our climate model resolution is too coarse to examine these catchments in detail, our mechanism could provide an explanation for both of these records. On the basis of inference from our model results, and from discussions with a Chief Operational Meteorologist from the Met Office, we suggest that a) the warm vegetated Wilkes Land could have caused the grounded ice sheet in the Ross Sea and that b) a large ice sheet in the Ross Sea could have helped to maintain the vegetated Wilkes Land. We have shown in our model results how the presence of a warm vegetated Antarctic surface will draw moisture in from the Southern Ocean (Fig. 5c). If this warm moist air is drawn in over the Wilkes Land, when reaches the Transantarctic Mountains, it would likely lift and fall as snow into the Ross Sea catchments. Cold katabatic winds could then form from the top of the Transantarctic Mountains and flow over the growing Ross Sea sector ice sheet and complete the localized circulation of air. As ice in one catchment retreats, therefore, ice in another could advance, and vice versa. The resolution of the data from Site U1356 in the Wilkes Land¹³ is not sufficient to compare directly with the extreme shifts in environmental motif documented in the AND-2A core in the Ross Sea between ~16.4 and 15.9 Ma²¹. However, changes in the extent of ice cover in the Wilkes Land vicinity could have been the trigger. Although evidence from other coastal catchments during the MCO is limited, we further suggest that such inter-catchment relationships could have also existed elsewhere since ice sheet advance requires a moisture supply, which our mechanism can provide. The record from Site 1171 in the Southern Ocean shows periods of ice sheet advance coincident with the warmest deep ocean temperatures⁵, which we infer from our model results to indicate large ice-free vegetated areas, not just that of the Wilkes Land. Higher resolution modelling than performed in the present study would be needed to confirm or reject these ideas.

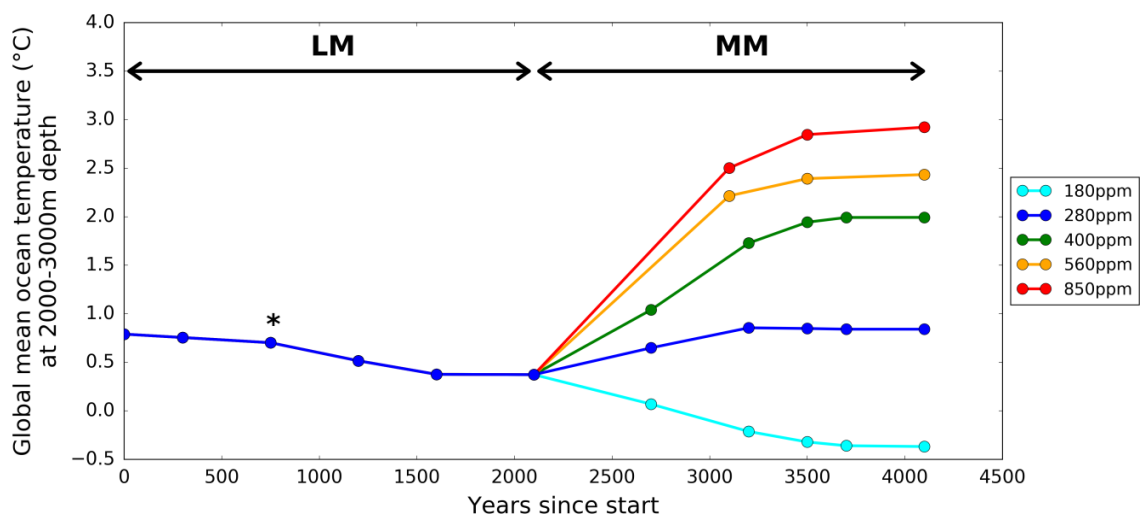


Supplementary Figure S64. Location of core sites. Basemap shown is the bed elevation from Bedmap2³⁸

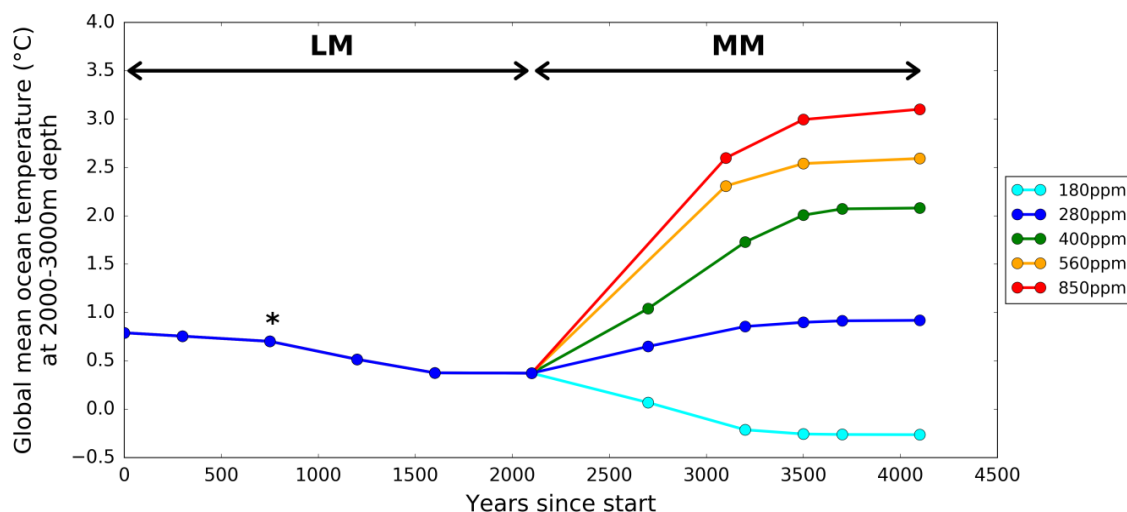
H. Model spinup



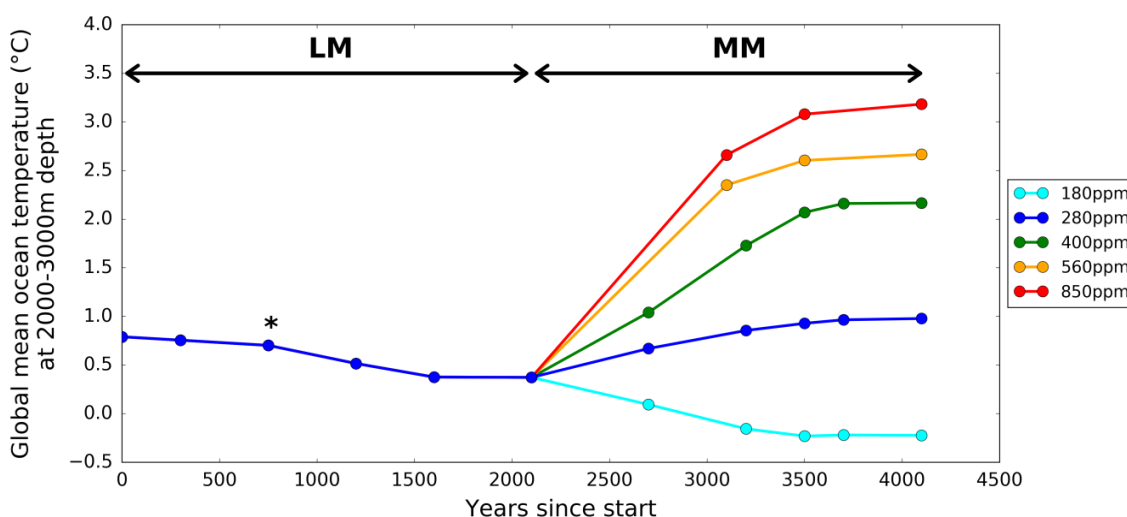
Supplementary Figure S65. Deep ocean temperature evolution through the simulations for the 0m sea level equivalent ice sheet Antarctic boundary condition. LM =late Miocene boundary conditions⁴, MM=middle Miocene boundary conditions (refer to Fig. 2). *The change in the deep ocean temperatures under the late Miocene boundary conditions at this step in the simulations is as a result of a significant change in the overall model setup onto a different computer.



Supplementary Figure S66. Deep ocean temperature evolution through the simulations for the 1m sea level equivalent ice sheet Antarctic boundary condition. LM =late Miocene boundary conditions⁴, MM=middle Miocene boundary conditions (refer to Fig. 2). *The change in the deep ocean temperatures under the late Miocene boundary conditions at this step in the simulations is as a result of a significant change in the overall model setup onto a different computer.



Supplementary Figure S67. Deep ocean temperature evolution through the simulations for the 55m sea level equivalent ice sheet Antarctic boundary condition. LM =late Miocene boundary conditions⁴, MM=middle Miocene boundary conditions (refer to Fig. 2). *The change in the deep ocean temperatures under the late Miocene boundary conditions at this step in the simulations is as a result of a significant change in the overall model setup onto a different computer.



Supplementary Figure S68. Deep ocean temperature evolution through the simulations for the 90m sea level equivalent ice sheet Antarctic boundary condition. LM =late Miocene boundary conditions⁴, MM=middle Miocene boundary conditions (refer to Fig. 2). *The change in the deep ocean temperatures under the late Miocene boundary conditions at this step in the simulations is as a result of a significant change in the overall model setup onto a different computer.

S3. Supplementary Information References

1. Bradshaw, C. D., Lunt, D. J., Flecker, R. & Davies-Barnard, T. Disentangling the roles of late Miocene palaeogeography and vegetation--Implications for climate sensitivity. *Palaeogeogr. Palaeoclimatol. Palaeoecol.* **417**, 17–34 (2015).
2. Bradshaw, C. D. *et al.* The relative roles of CO₂ and palaeogeography in determining late Miocene climate: results from a terrestrial model-data comparison. *Clim. Past* **8**, 715–786 (2012).
3. Goldner, A., Herold, N. & Huber, M. The Challenge of Simulating the Warmth of the Mid-Miocene Climatic Optimum in CESM1. *Clim. Past* (2014).
4. Markwick, P. J. The palaeogeographic and palaeoclimatic significance of climate proxies for data-model comparisons. in *Deep-Time Perspectives on Climate Change: Marrying the Signal from Computer Models and Biological Proxies* 251–312 (The Geological Society, 2007).
5. Shevenell, A. E., Kennett, J. P. & Lea, D. W. Middle Miocene ice sheet dynamics, deep-sea temperatures, and carbon cycling: A Southern Ocean perspective. *Geochemistry, Geophys. Geosystems* **9**, (2008).
6. Elderfield, H., Yu, J., Anand, P., Kiefer, T. & Nyland, B. Calibrations for benthic foraminiferal Mg/Ca paleothermometry and the carbonate ion hypothesis. *Earth Planet. Sci. Lett.* **250**, 633–649 (2006).
7. Gray, W. R. & Evans, D. Nonthermal influences on Mg/Ca in planktonic foraminifera: a review of culture studies and application to the Last Glacial Maximum. *Paleoceanogr. Paleoclimatology* **34**, 306–315 (2019).
8. Lear, C. H., Mawbey, E. M. & Rosenthal, Y. Cenozoic benthic foraminiferal Mg/Ca and Li/Ca records: Toward unlocking temperatures and saturation states. *Paleoceanography* **25**, (2010).
9. Lear, C. H. *et al.* Neogene ice volume and ocean temperatures: Insights from infaunal

- foraminiferal Mg/Ca paleothermometry. *Paleoceanography* **30**, 1437–1454 (2015).
10. You, Y., Huber, M., Müller, R. D., Poulsen, C. J. & Ribbe, J. Simulation of the middle Miocene climate optimum. *Geophys. Res. Lett.* **36**, (2009).
 11. Herold, N., Huber, M., Müller, R. D. & Seton, M. Modeling the Miocene climatic optimum: Ocean circulation. *Paleoceanography* **27**, (2012).
 12. Passchier, S. *et al.* Early Eocene to middle Miocene cooling and aridification of East Antarctica. *Geochemistry, Geophys. Geosystems* **14**, 1399–1410 (2013).
 13. Sangiorgi, F. *et al.* Southern Ocean warming and Wilkes Land ice sheet retreat during the mid-Miocene. *Nat. Commun.* **9**, 317 (2018).
 14. Feakins, S. J., Warny, S. & Lee, J.-E. Hydrologic cycling over Antarctica during the middle Miocene warming. *Nat. Geosci.* **5**, 557 (2012).
 15. Super, J. R. *et al.* North Atlantic temperature and pCO₂ coupling in the early-middle Miocene. *Geology* **46**, 519–522 (2018).
 16. Zhang, Y. G., Pagani, M., Liu, Z., Bohaty, S. M. & DeConto, R. A 40-million-year history of atmospheric CO₂. *Philos. Trans. R. Soc. A Math. Phys. Eng. Sci.* **371**, 20130096 (2013).
 17. Scheiner, F., Holcová, K., Milovský, R. & Kuhnert, H. Temperature and isotopic composition of seawater in the epicontinental sea (Central Paratethys) during the Middle Miocene Climate Transition based on Mg/Ca, $\delta^{18}\text{O}$ and $\delta^{13}\text{C}$ from foraminiferal tests. *Palaeogeogr. Palaeoclimatol. Palaeoecol.* **495**, 60–71 (2018).
 18. Rousselle, G., Beltran, C., Sicre, M.-A., Raffi, I. & De Raféllis, M. Changes in sea-surface conditions in the Equatorial Pacific during the middle Miocene--Pliocene as inferred from coccolith geochemistry. *Earth Planet. Sci. Lett.* **361**, 412–421 (2013).
 19. Shevenell, A. E., Kennett, J. P. & Lea, D. W. Middle Miocene southern ocean cooling and Antarctic cryosphere expansion. *Science (80-.)*. **305**, 1766–1770 (2004).
 20. Leutert, T. J., Auderset, A., Martínez-García, A., Modestou, S. & Meckler, A. N. Coupled Southern Ocean cooling and Antarctic ice sheet expansion during the middle Miocene.

- Nat. Geosci.* (2020). doi:10.1038/s41561-020-0623-0
21. Levy, R. *et al.* Antarctic ice sheet sensitivity to atmospheric CO₂ variations in the early to mid-Miocene. *Proc. Natl. Acad. Sci.* **113**, 3453–3458 (2016).
 22. Sosdian, S. M. *et al.* Constraining the evolution of Neogene ocean carbonate chemistry using the boron isotope pH proxy. *Earth Planet. Sci. Lett.* **498**, 362–376 (2018).
 23. Foster, G. L., Lear, C. H. & Rae, J. W. B. The evolution of pCO₂, ice volume and climate during the middle Miocene. *Earth Planet. Sci. Lett.* **341**, 243–254 (2012).
 24. Kuhnert, H., Bickert, T. & Paulsen, H. Southern Ocean frontal system changes precede Antarctic ice sheet growth during the middle Miocene. *Earth Planet. Sci. Lett.* **284**, 630–638 (2009).
 25. Super, J. R., Thomas, E., Pagani, M. & Huber, M. Miocene Evolution of North Atlantic Sea Surface Temperature. *Paleoceanogr. Paleoclimatology* **Accepted**, (2020).
 26. Kochhann, K. G. D., Holbourn, A., Kuhnt, W. & Xu, J. Eastern equatorial Pacific benthic foraminiferal distribution and deep water temperature changes during the early to middle Miocene. *Mar. Micropaleontol.* **133**, 28–39 (2017).
 27. Billups, K. & Schrag, D. P. Paleotemperatures and ice volume of the past 27 Myr revisited with paired Mg/Ca and ¹⁸O/¹⁶O measurements on benthic foraminifera. *Paleoceanography* **17**, 1–3 (2002).
 28. Knorr, G. & Lohmann, G. Climate warming during Antarctic ice sheet expansion at the Middle Miocene transition. *Nat. Geosci.* **7**, 376 (2014).
 29. Via, R. K. & Thomas, D. J. Evolution of Atlantic thermohaline circulation: Early Oligocene onset of deep-water production in the North Atlantic. *Geology* **34**, 441–444 (2006).
 30. Davies, R., Cartwright, J., Pike, J. & Line, C. Early Oligocene initiation of North Atlantic deep water formation. *Nature* **410**, 917 (2001).
 31. Coxall, H. K. *et al.* Export of nutrient rich Northern Component Water preceded early

- Oligocene Antarctic glaciation. *Nat. Geosci.* **11**, 190 (2018).
32. Poore, H. R., Samworth, R., White, N. J., Jones, S. M. & McCave, I. N. Neogene overflow of northern component water at the Greenland-Scotland Ridge. *Geochemistry, Geophys. Geosystems* **7**, (2006).
 33. Cramer, B. S., Toggweiler, J. R., Wright, J. D., Katz, M. E. & Miller, K. G. Ocean overturning since the Late Cretaceous: Inferences from a new benthic foraminiferal isotope compilation. *Paleoceanography* **24**, (2009).
 34. Cortese, G., Gersonde, R., Hillenbrand, C.-D. & Kuhn, G. Opal sedimentation shifts in the World Ocean over the last 15 Myr. *Earth Planet. Sci. Lett.* **224**, 509–527 (2004).
 35. Gasson, E., DeConto, R. M., Pollard, D. & Levy, R. H. Dynamic Antarctic ice sheet during the early to mid-Miocene. *Proc. Natl. Acad. Sci.* **113**, 3459–3464 (2016).
 36. Colleoni, F. *et al.* Spatio-temporal variability of processes across Antarctic ice-bed--ocean interfaces. *Nat. Commun.* **9**, 2289 (2018).
 37. Modestou, S., Leutert, T. J., Fernandez, A., Lear, C.H., Neckler, A.N. Warm middle Miocene Indian Ocean bottom water temperatures: comparison of clumped isotope and Mg/Ca records. *Paleoceanography and Paleoclimatology* **35(11)** e2020PA003927 (2020)
 38. Fretwell, P., Pritchard, H.D., Vaughan, D.G., Bamber, J.L., Barrand, N.E., Bell, R., Bianchi, C., Bingham, R.G., Blankenship, D.D., Casassa, G. and Catania, G., Bedmap2: improved ice bed, surface and thickness datasets for Antarctica. *The Cryosphere*, **7(1)**, pp.375-393. (2013)